Utrecht University

UU - Institute for Theoretical Physics (utrecht)

ICFO - Institute of Photonic Sciences (barcelona)

Master Thesis

Generating Gauge Fields in Optical Kagome and Dice Lattices

Author:
Tessa Verboven, BSc.

Supervisors:
Dr. Alessio Celi (ICFO)
Dr. Lars Fritz (UU)

July 11, 2016

Abstract

Flat energy bands are suitable for observing the Fractional Quantum Hall Effect. We propose an optical setup that can be used for probing flat bands of the Kagome and dice lattice structures dressed by a gauge field. For the Kagome lattice we show that these bands are indeed topologically nontrivial. We suggest using an optical potential that generates the Kagome and dice structures simultaneously. We propose a lattice shaking-scheme to induce a gauge field that is equivalent to a magnetic field, resulting in the desired energy spectrum. Combining the shaking with resonant driving and a site-dependent phase shift, we present a construction for the Kagome lattice that generates flat bands that can be probed experimentally. Implementing interactions in this setup immediately corresponds to being in the strongly correlated regime.

Acknowledgements

First of all, I would like to thank my supervisor Alessio Celi for giving me the opportunity to come to Barcelona and write my master thesis at ICFO in the group of Maciej Lewenstein. During our collaboration he always took the time to answer my questions, combining physical and mathematical intuition in a way that I very much admire.
During my time at ICFO I have met many people of various research fields and nationalities. A special thanks to Nils Günther, for the tough but fair criticism and all the moral support. Thanks Gorka Muñoz, for taking the time to read my work while working on his own thesis. Thank you Ameer Ghouse, for improving my English vocabulary and attending my final presentation. Good luck with your careers at ICFO!
Many thanks to the people in the ICFO Visitor's Room generation february 2016 for all the lunches, dinners, beach hangouts and poolparties. I hope to see you all once again!

I want to thank Lars Fritz for his supervision, on this thesis as well as during the courses I have taken from him in the past three years. Thanks to him I became interested in the field of topological insulators. Moreover, he has taught me how to give proper clear-cut presentations which I will benefit from the rest of my life.

A little shoutout to my sister Anouk Verboven, who is now in Los Angeles finishing her Master's degree, and inspired me to go abroad as well. And finally I would like to thank my parents for supporting me in 7 years of studying. Thanks to you I can soon call myself Bachelor of Arts and Master of Science.

¡Muchas gracías a todos!

Introduction

The conducting or insulating properties of a solid are largely determined by the lattice the atoms are structured in. The Kagome and dice lattices considered in this thesis are specifically interesting because of their *topological* properties, a concept that has existed in mathematics since mid 19^{th} century. Topological properties of a manifold (smoothly curved space or set) are those that are preserved under continuous deformations. They depend on the global structure of the system and not on the form they have locally. A famous example is the comparison of a mug and a donut, which are topologically equivalent as one can smoothly be deformed into the other. But both of them can not be transformed to a disk, because removing the hole is not a smooth deformation. The number of holes in the donut, mug and disk can be viewed as a topological invariants of these manifolds.

The introduction of topological quantities in physics was marked by the discovery of the Quantum Hall Effect, the quantummechanical variant of the classical Hall effect. The classical Hall Effect can be observed in the setup shown in Figure 1a. In the approximately two-dimensional slab charged particles move around in the perpendicular magnetic. Due to the Lorentz force $\boldsymbol{F}_L = q(\boldsymbol{E} + \boldsymbol{v} \times \boldsymbol{B})$ these particles will be deflected. The direction of this deflection will be opposite for negatively and positively charged particles, such that a potential difference arises in the transverse direction. This transverse conductivity is proportional to the strength of the magnetic field: $\sigma_{\text{tr}} \propto |\boldsymbol{B}|$.

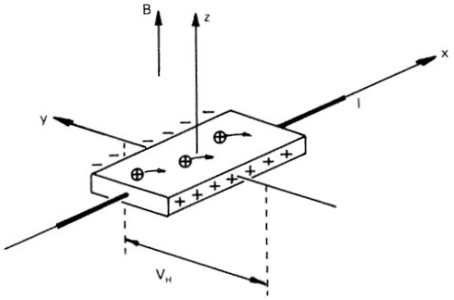

(a) The setup used to measure the Hall Effect. B is the perpendicular magnetic field and I a current that is sent through the material. (Kosmos, 1986)

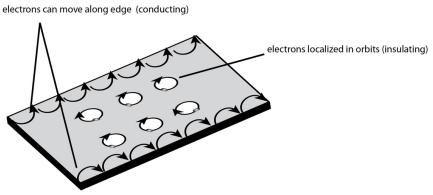

(b) For a stronger perpendicular magnetic field $\boldsymbol{B}$ the trajectories of the electrons become circles.

Figure 1

For stronger magnetic fields $\boldsymbol{B}$ the trajectory of the electrons is deflected so heavily that they start moving in small circular trajectories as shown in Figure 1b. The radii of these trajectories are quantized at these high fields strengths. For electrons in the bulk this means that they cannot transport charge through the system anymore, and the bulk becomes insulating. But at the edges the electrons cannot make full circles; instead they start bouncing off the edges in semi-circles, either clockwise or anti-clockwise. Due to their left- or right-handedness these states have a certain *chirality*. The chiral edge states *are* capable of carrying current, and causes the transverse conductivity to still be present in the system.
The phenomenon above was foreseen to be a quantum effect by Ando et al. [1], who theoretically predicted that the transverse conductivity equals $\sigma_{\text{tr}} = (e^2/h)N,\ N \in \mathbb{N}$.

In 1980 this relation was probed in an experiment conducted by von Klitzing et al. [2], producing the result shown in Figure 2.

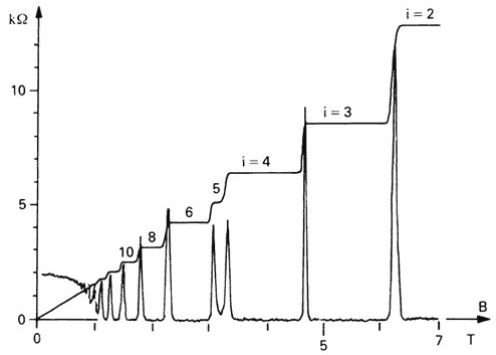

Figure 2: The integer Quantum Hall Effect. For stronger magnetic fields, the linear proportionality of the transverse conductivity to the strength of the magnetic field (horizontal axis) changes to plateaus proportional to integer multiples of e^2/h. Also the longitudinal conductivity is plotted, exhibiting spikes whenever the transverse conductivity changes plateau showing that inbetween the bulk becomes conducting. (Kosmos, 1986)

According to the measurements the plateaus were equal to integer multiples of $R_K = 25812.807557(18)\ \Omega$, agreeing almost exactly with the value of $(e^2/h)^{-1}$. This was very surprising: it was certain that the experimental setup contained disorder (e.g. impurities in the material) which had not been taken into account in the theoretical prediction. The transverse conductivity turned out to depend only on the number of edge states in the system, whose existence was apparently robust against contamination in the system. It turned out that the edge states are *topologically protected*, and the material was termed a *topological insulator*: an insulating bulk with topologically protected currents on the boundaries.

In the early 90's measurements of the transverse conductivity for even stronger magnetic fields were conducted by Störmer et al. [3]. The result - awarded with the Nobel Prize in 1998 - is shown in Figure 3.

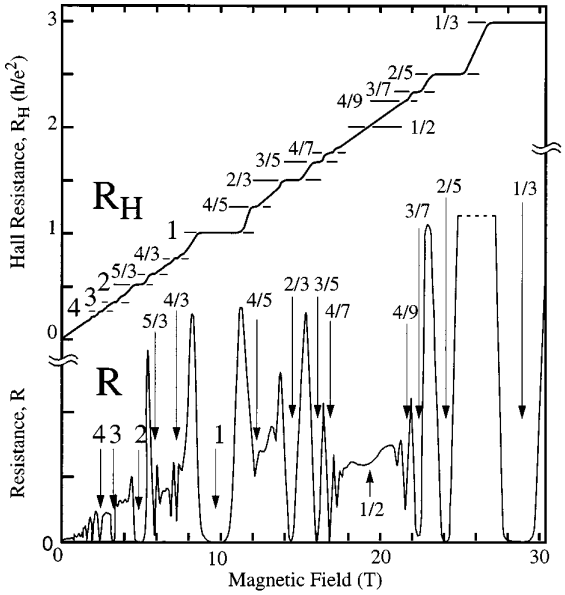

Figure 3: For strengths of the magnetic field above 7 T the transverse conductivity becomes proportional to fractional values of e^2/h. [3]

The transverse conductivity is now proportional to fractional multiples of e^2/h: $\sigma_{\text{tr}} = (e^2/h)Q$, $Q \in \mathbb{Q}$. Although this behaviour is partly explained by the effect of electron-electron interactions becoming significant, it is still not completely understood.
Just as for the integer Quantum Hall Effect these fractional values are topologically protected, which makes them suitable for applications. The Fractional Quantum Hall Effect is observed more easily in systems with a *flat energy band*, because the addition of interactions immediately result in strongly correlated effects [4]. We will see in this thesis that the Kagome and dice lattice have these flat bands; therefore they are interesting systems to simulate and examine.
Using optical lattices to simulate these systems has several advantages. First of all, it is difficult to find solids in nature whose atoms are perfectly structured in a lattice configuration. In optical lattices one can create a periodic structure using standing wave patterns in a clean and regular way, by creating standing wave patterns with pairs of counterpropagating lasers (see Figure 4).

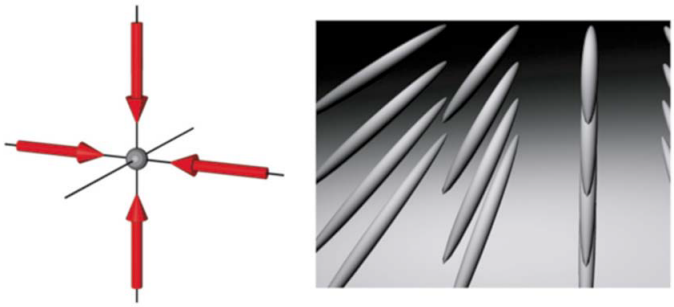

Figure 4: Two orthogonal pairs of counterpropagating lasers result creating a square optical lattice in two dimensions (figure taken from [5]).

The simulation using optical lattices enables control of parameters in the system: the distance between lattice sites depends on wavelength of the laser, the strength of confinement of the atoms on the intensity of the laser. One can show that for lattice distances considered in these optical lattices the magnitude of the magnetic fields needed is of the order of 10^9 T - many orders of magnitude higher than what is now experimentally feasible. But by periodically shaking the lattice in the plane we can generate gauge fields that are equivalent to applying a perpendicular magnetic field, with which we are able to reach the desired magnitudes.

In this thesis we aim to propose a setup generating the Kagome and dice lattice with flat bands in the energy spectrum. This setup can then be used to probe the flat bands for strongly correlated effects. We start by defining a topological invariant in Chapter 1. In Chapter 2 we consider several lattice structures (including the Kagome and dice lattic) and show how applying a magnetic field affects the energy spectrum. In Chapter 3 we introduce the concept of a time-dependent Hamiltonian and the Floquet formalism, and subsequently we use this to show that shaking the lattice results in the generation of a gauge field. Finally, in Chapter 4 we combine the concepts developed before with the construction of optical lattices to propose a setup that generates flat bands.

Contents

1 Topological properties of two-dimensional sytems

The topological properties of a system are determined by its Hamiltonian. One way to determine if a system possesses topologically invariant quantities is by considering the energy spectrum. These properties of the system that can not be destroyed by local perturbations such as impurities or disorder, which indicates why they are potentially interesting to use for applications.

In this section we present the physical and mathematical framework for working with topological properties of system. First we review how to compute the energy spectrum for a lattice using the example of the square lattice. We then move on to the formal definition of a topological invariant called the *Chern number* using the Berry phase. After this we present a numerical method to compute the Chern number for separated energy bands (without degeneracy) developed by Fukui et al. [6]. A background on how the topological properties of a system are related to symmetries of the Hamiltonian can be found in Appendix A.

1.1 Topology in energy bands

We can model the kinetics of electrons in a two-dimensional solid by particles hopping between sites structured in a periodic lattice. Consider for example the square lattice shown in Figure 5. In the x- and y-direction each site is separated by a distance the *lattice constant* in units of length, which we put equal to 1 here for simplicity. We can describe coordinates on this lattice using $\boldsymbol{x} = (x_i, y_j)$. Assuming that the particles only hop to nearest neighbour lattice sites, we can use the tight-binding approximation. In second quantization this Hamiltonian for two-dimensional systems equals:

$$H = -J \sum_{\boldsymbol{x}} \sum_{\ell} \left(a^\dagger_{\boldsymbol{x}+\boldsymbol{\delta}_\ell} a_{\boldsymbol{x}} + \text{H.c.} \right). \tag{1}$$

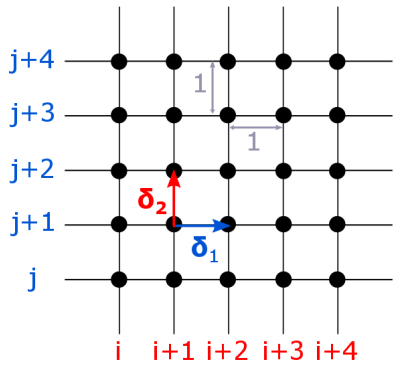

Figure 5: The square lattice.

The sum runs over all lattice sites $\boldsymbol{x} = (x_i, y_j)$ and the number of lattice unit vectors $\ell = 1, \ldots, \ell_{\max}$. The parameter $J \in \mathbb{R}$ indicates the hopping strength, which can be determined from the overlap of the wavefunctions of the particles (see Section 4.2). The system minimizes its energy when particles hop around, as for each hop an amount $-J$ is added to the energy. The ladder operators $a^{(\dagger)}_{\boldsymbol{x}}$ annihilate (create) a particle at site $\boldsymbol{x}$. They commute as $\left[a_{\boldsymbol{x}}, a^\dagger_{\boldsymbol{x}'}\right] = \delta_{\boldsymbol{x},\boldsymbol{x}'}$ for bosons and anticommute as $\left\{a_{\boldsymbol{x}}, a^\dagger_{\boldsymbol{x}'}\right\} = \delta_{\boldsymbol{x},\boldsymbol{x}'}$ for fermions. The vectors $\boldsymbol{\delta}_l$ indicate the lattice unit vectors, connecting nearest-neighbour sites. The lattice unit vectors $\boldsymbol{\delta}_\ell$ are distinct in the sense that $\boldsymbol{\delta}_\ell \neq -\boldsymbol{\delta}_{\ell'}$. For the square lattice they are given by

$$\boldsymbol{\delta}_1 = (1, 0) \qquad \text{and} \qquad \boldsymbol{\delta}_2 = (0, 1). \tag{2}$$

For every site $\boldsymbol{x}$ we can jump in all directions $\pm\boldsymbol{\delta}_1, \pm\boldsymbol{\delta}_2$. An infinite amount of lattice sites then immediately implies periodicity (Bravais). We can define a discrete Fourier transform to get an expression for the Hamiltonian in $\boldsymbol{k}$-space. The discrete Fourier transforms of the ladder operators are defined as:

$$a^\dagger_{\boldsymbol{x}} = \frac{1}{V} \sum_{\boldsymbol{k}} e^{-i\boldsymbol{k}\cdot\boldsymbol{x}} a^\dagger_{\boldsymbol{k}} \qquad \text{and} \qquad a_{\boldsymbol{x}} = \frac{1}{V} \sum_{\boldsymbol{k}} e^{i\boldsymbol{k}\cdot\boldsymbol{x}} a_{\boldsymbol{k}}. \tag{3}$$

Using the definition of the Kronecker delta-function this allows us to rewrite our Hamiltonian as

$$H = \sum_{\boldsymbol{k}} a_{\boldsymbol{k}}^{\dagger} \mathcal{H}_{\boldsymbol{k}} a_{\boldsymbol{k}}, \tag{4}$$

where the energy spectrum is given by the Bloch Hamiltonian

$$\begin{aligned} \mathcal{H}_{\boldsymbol{k}} = \varepsilon_{\boldsymbol{k}} &= -J \sum_{\ell} 2 \cos \boldsymbol{k} \cdot \boldsymbol{\delta}_{\ell}. && (5) \\ &= -2J \left(\cos \boldsymbol{k} \cdot \boldsymbol{\delta}_1 + \cos \boldsymbol{k} \cdot \boldsymbol{\delta}_2 \right) \\ &= -2J \left(\cos k_x + \cos k_y \right). && (6) \end{aligned}$$

We observe that the energy is determined completely by the hopping parameter J and the lattice unit vectors $\boldsymbol{\delta}_{\ell}$. Note that due to the definition of the discrete Fourier transform the values of the energy are uniquely defined for $\boldsymbol{k}$ in the first Brillouin Zone $[-\pi, \pi] \times [-\pi, \pi]$. The energy spectrum in the first Brillouin zone is plotted below in Figure 6.

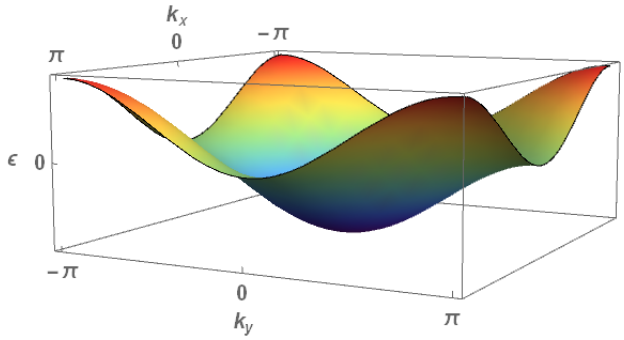

Figure 6: The single energy band for the square lattice with $J > 0$.

For lattice structures that are not Bravais the Bloch Hamiltonian is not a scalar, but a matrix. This is related to the number of sites in the unit cell. The possible hopping directions $(\boldsymbol{\delta}_{\ell})_{\boldsymbol{x}}$ on the lattice site $\boldsymbol{x}$ depend strongly on the structure of the lattice. For lattices with one site in their unit cell, the surroundings of every site look exactly the same. This indicates that the lattice possesses a Bravais structure. When this is not the case we can enlarge the unit cell to multiple sites, corresponding to the introduction of sublattices. By displacing the unit cell one is able to reconstruct the whole lattice. This changes the structure of the Hamiltonian to a matrix equation. The number of energy bands (eigenvalues) is determined by the dimension of the Bloch Hamiltonian.

For each point in the Brillouin Zone we can determine the eigenstates defined by the time-independent Schrödinger equation:

$$\mathcal{H}_{\boldsymbol{k}} |\psi_{\boldsymbol{k}}\rangle = \varepsilon_{\boldsymbol{k}} |\psi_{\boldsymbol{k}}\rangle. \tag{7}$$

When there are multiple bands in the energy spectrum, the value of the energy depends on the band m and on the point in momentum space $\boldsymbol{k}$: $\varepsilon \to \varepsilon_{\boldsymbol{k}}^{(m)}$. Correspondingly, the eigenvector will do so as well: $|\psi\rangle \to \left|\psi_{\boldsymbol{k}}^{(m)}\right\rangle$. For a specific band m, we can continuously change the vector $\boldsymbol{k}$ to $\boldsymbol{k} + d\boldsymbol{k}$. The transformation of the eigenvector $\left|\psi_{\boldsymbol{k}}^{(m)}\right\rangle$ to $\left|\psi_{\boldsymbol{k}+d\boldsymbol{k}}^{(m)}\right\rangle$ is $U(1)$, corresponding to a rotation.

Consider the reciprocal lattice vectors that span the Brillouin Zone: $\boldsymbol{k}_1 = 2\pi(1,0)$ and $\boldsymbol{k}_2 = 2\pi(0,1)$. When we move through the whole Brillouin Zone by translating with these vectors $\boldsymbol{k} + \boldsymbol{k}_{1,2}$ by definition the eigenvectors must come back to itself: $\left|\psi_{\boldsymbol{k}+\boldsymbol{k}_{1,2}}\right\rangle = |\psi_{\boldsymbol{k}}\rangle$. Therefore, the unitary transformation must equal the identity and the angle corresponding to the rotation must equal an integer multiple n of 2π. The integer n, also called the Chern number, is a topological invariant. When the system is topologically nontrivial, this integer will be nonzero [7].

We have now qualitatively argued how the curvature of the energy bands relates to the value of the transverse conductivity. In Section 1.2 we will derive the mathematical definition of the topological invariant (called the Chern number) for two-dimensional systems.

1.2 Berry phase & Chern number

For the formal definition of the Chern number in terms of the Berry phase, we will broadly follow the derivation as given by Asbóth et al. in *A Short Course on Topological Insulators* [8].

We move back to the eigenvector from Section 1.1 defined by:

$$\mathcal{H}_{\boldsymbol{k}} \left|\psi_{\boldsymbol{k}}^{(m)}\right\rangle = \varepsilon_{\boldsymbol{k}}^{(m)} \left|\psi_{\boldsymbol{k}}^{(m)}\right\rangle. \tag{8}$$

Recall that m determines the number of the energy band (we choose $m = 1$ to be the lowest band) and $\boldsymbol{k} = (k_x, k_y)$ is a point in the Brillouin zone. When we move an infinitesimal amount through the Brillouin zone, from $\boldsymbol{k}$ to $\boldsymbol{k} + d\boldsymbol{k}$, the initial and final eigenvector will differ by a U(1) transformation (a rotation). Using the time-dependent Schrödinger equation [9] it can be derived that the difference in phase equals (up to 1st order)

$$d\gamma = \underbrace{i \left\langle \psi_{\boldsymbol{k}}^{(m)} \right| \nabla_{\boldsymbol{k}} \left|\psi_{\boldsymbol{k}}^{(m)}\right\rangle}_{=\boldsymbol{\mathcal{A}}_{\boldsymbol{k}}} \cdot d\boldsymbol{k}. \tag{9}$$

The emphasized quantity $\boldsymbol{\mathcal{A}}_{\boldsymbol{k}}$ is known as the *Berry connection*, relating the eigenvectors at $\boldsymbol{k}$ and $\boldsymbol{k} + d\boldsymbol{k}$. Observe that this quantity is only well-defined for energy bands that are *non-degenerate*. The $U(1)$ transformation is then defined as

$$e^{-id\gamma} = \frac{\left\langle \psi_{\boldsymbol{k}}^{(m)} \middle| \psi_{\boldsymbol{k}+d\boldsymbol{k}}^{(m)} \right\rangle}{\left| \left\langle \psi_{\boldsymbol{k}}^{(m)} \middle| \psi_{\boldsymbol{k}+d\boldsymbol{k}}^{(m)} \right\rangle \right|}. \tag{10}$$

Indeed the quantity on the right side is of length 1. The *Berry phase* is now defined as the phase picked up when moving along a closed loop $\mathcal{C}$:

$$\gamma(\mathcal{C}) = -\arg\left(\exp\left[-i \oint_{\mathcal{C}} \boldsymbol{\mathcal{A}}_{\boldsymbol{k}} \cdot d\boldsymbol{k}\right]\right). \tag{11}$$

While the Berry connection $\boldsymbol{\mathcal{A}}_{\boldsymbol{k}}$ is not gauge invariant, the Berry phase is. Therefore it is an observable variable.

If we now consider the closed loop $\mathcal{C} = \partial\mathcal{S}$ to be the boundary of a surface $\mathcal{S}$ which is part of the Brillouin zone, applying the Stokes' theorem results in

$$\oint_{\partial\mathcal{S}} \boldsymbol{\mathcal{A}}_{\boldsymbol{k}} \cdot d\boldsymbol{k} = \int_{\mathcal{S}} (\boldsymbol{\nabla} \times \boldsymbol{\mathcal{A}}_{\boldsymbol{k}}) \cdot d\boldsymbol{S}. \tag{12}$$

The vector $d\boldsymbol{S}$ is the vector normal to the surface $\mathcal{S}$. This quantity is still gauge invariant.

The equations derived above are analogous toh those for magnetic fields. If we consider $\boldsymbol{\mathcal{A}}_{\boldsymbol{k}}$ as a vector potential defining a gauge field $\boldsymbol{\mathcal{B}}_{\boldsymbol{k}} = \boldsymbol{\nabla} \times \boldsymbol{\mathcal{A}}_{\boldsymbol{k}}$ (the *Berry curvature*), then the Berry phase the flux through $\mathcal{S}$ produced by this gauge field:

$$\gamma(\partial\mathcal{S}) = -\arg\left(\exp\left[-i\int_{\mathcal{S}} \boldsymbol{\mathcal{B}}_{\boldsymbol{k}} \cdot d\boldsymbol{S}\right]\right) = -\int_{\mathcal{S}} \boldsymbol{\mathcal{B}}_{\boldsymbol{k}} \cdot d\boldsymbol{S}. \tag{13}$$

From this definition one can also see that the Berry phase is robust against continuous deformations of the energy band $\mathcal{S}$. The smoothness of the Berry curvature is the only property affecting its value: taking the curl of the Berry connection means we measure vortices in the gauge potential. These vortices are the quantity contributing to the Berry phase.

Using the periodicity of the Brillouin zone $\boldsymbol{k} + \boldsymbol{K} = \boldsymbol{k}$, the following equality holds:

$$\left|\psi^{(m)}_{\boldsymbol{k}+\boldsymbol{K}}\right\rangle = \left|\psi^{(m)}_{\boldsymbol{k}}\right\rangle. \tag{14}$$

Therefore, when $\mathcal{S} = \mathrm{BZ}$ the Berry phase must be a multiple of 2π. The exact multiple defines the *Chern number*:

$$\begin{aligned} c_m &= -\frac{1}{2\pi}\int_{\mathrm{BZ}} \boldsymbol{\mathcal{B}}_{\boldsymbol{k}} \cdot d\boldsymbol{S} \\ &= -\frac{1}{2\pi}\int_{\mathrm{BZ}} \left(\boldsymbol{\nabla} \times \left\langle \psi^{(m)}_{\boldsymbol{k}} \right| \nabla_{\boldsymbol{k}} \left| \psi^{(m)}_{\boldsymbol{k}} \right\rangle\right) \cdot d\boldsymbol{S}. \end{aligned} \tag{15}$$

By construction the Chern number will always be an integer, counting the number of vortices in energy band m. The energy bands need to be nondegenerate such that the displacement from $\boldsymbol{k}$ to $\boldsymbol{k} + d\boldsymbol{k}$ is always well-defined. Just like the Berry phase the Chern number is a gauge-invariant quantity.

Finally the transverse conductivity can be computed from the Chern number by summing over all bands that are filled (which are below the Fermi energy ε_F):

$$\sigma_{\mathrm{tr}} = \frac{e^2}{h}\sum_{m<m_{\mathrm{F}}} c_m. \tag{16}$$

When all bands are completely filled, the sum over the Chern numbers must be zero. Conducting edge states are not allowed, because their energy cannot cross the Fermi level. The system therefore has to be topologically trivial.

1.3 Numerical computation of the winding number

We now introduce a numerical method to compute the Chern number by discretizing the Brillouin Zone, developed by Fukui et al. [6]. They show that this method is manifestly gauge-invariant and therefore we can use this to compute Chern number without specifying a gauge. As in the previous section it only works for non-degenerate energy bands.

First we discretize the Brillouin Zone by implementing the following grid:

$$\begin{aligned} &\boldsymbol{k}_\alpha = (k_{j_x}, k_{j_y}), && k_{j_\mu} = (\delta k)_\mu j_\mu && (\delta k)_\mu = \frac{2\pi}{q_\mu N_\mu} \\ &\alpha = 1, \ldots, N_x N_y && j_\mu = 0, \ldots, N_\mu - 1 && \mu \in \{x, y\}. \end{aligned} \tag{17}$$

The number of sites in direction $\hat{\boldsymbol{\mu}}$ is given by N_μ. The integer q_μ allows us to differ between the step sizes in $\hat{\boldsymbol{x}}$- and $\hat{\boldsymbol{y}}$-direction. We can move between gridpoints using the unit vectors $(\delta k)_\mu \hat{\mu} = 2\pi/(q_\mu N_\mu)\hat{\boldsymbol{\mu}}$. An example of a grid is shown in Figure 7a.

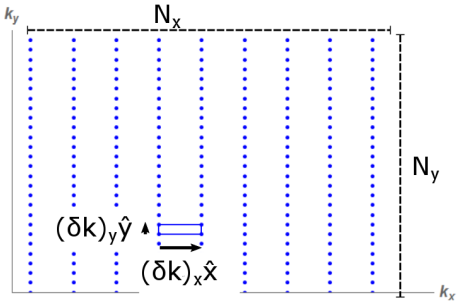

(a) A grid in $\boldsymbol{k}$-space with N_x in the x-direction and N_y sites in the y-direction.

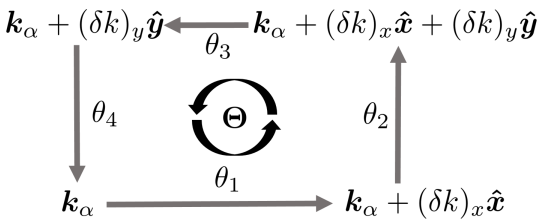

(b) When moving around a unit plaquette on the $\boldsymbol{k}_\alpha$-grid, the $U(1)$ transformations can be linked to a total enclosed flux Θ.

Figure 7

We implement periodic boundary conditions by demanding $\boldsymbol{k}_\alpha + N_u(\delta k)_\mu \hat{\boldsymbol{\mu}} = \boldsymbol{k}_\alpha$.

For each point on the grid we can compute the eigenvectors:

$$\mathcal{H}_{\boldsymbol{k}_\alpha} \left|\psi^{(m)}_{\boldsymbol{k}_\alpha}\right\rangle = \varepsilon^{(m)}_{\boldsymbol{k}_\alpha} \left|\psi^{(m)}_{\boldsymbol{k}_\alpha}\right\rangle . \tag{18}$$

The angle corresponding to the difference between two eigenvectors can be computed using the unitary transformation defined in Equation (10). A general plaquette is shown in Figure 7b. For the angle θ_1 indicated there we use the following definition:

$$e^{i\theta_1} = \frac{\left\langle \psi^{(m)}_{\boldsymbol{k}_\alpha} \middle| \psi^{(m)}_{\boldsymbol{k}_\alpha + (\delta k)_x \hat{\boldsymbol{x}}} \right\rangle}{\left| \left\langle \psi^{(m)}_{\boldsymbol{k}_\alpha} \middle| \psi^{(m)}_{\boldsymbol{k}_\alpha + (\delta k)_x \hat{\boldsymbol{x}}} \right\rangle \right|}, \tag{19}$$

and likewise for $\theta_{2,3,4}$. We can define the gauge field through a unit plaquette as

$$F(\boldsymbol{k}_\alpha) = \ln\left(e^{i\theta_1} e^{i\theta_2} e^{i\theta_3} e^{i\theta_4}\right) = i\Theta. \tag{20}$$

Note that this implicitly depends on the energy band m. Finally the Chern number is proportional to the sum of this over all lattice points:

$$c_m = \frac{1}{2\pi i} \sum_{\alpha=1}^{N_x N_y} F(\boldsymbol{k}_\alpha). \tag{21}$$

Because this computation will always give an integer result, increasing the resolution of the grid causes the Chern number to converge to the correct value quite fast (as is argued in [6]). So even for a coarsely discretized Brillouin zone this method is expected to reproduce the correct result. We will use this method to compute the Chern number for the energy spectra in Chapter 2.

2 Kagome and dice lattices with a magnetic field

In the previous chapter we have shown that the topological properties of a system can be derived from its energy spectrum. In turn, the structure of the energy spectrum depends on the structure of the lattice. Furthermore, we can alter the structure of the energy spectrum by applying a magnetic perturbation that splits the bands in the spectrum.

In this chapter we derive how the bandstructure changes when applying a perpendicular magnetic field to several two-dimensional lattices. To do so we first consider some more complex lattice structures that have more than one site in the unit cell. Also we introduce the structure of the Kagome and dice lattice. Then we introduce a method to incorporate the presence of a magnetic field in the language of second quantization, and derive the consequences on the energy spectra. Finally we compute the energy eigenvalues for varying strengths of the magnetic field, creating a symmetric fractal structure known as the Hofstadter butterfly.

2.1 Band structures

In this section we apply the lattice formalism introduced in Section 1.1 to the Kagome and dice structures. For this we first introduce the concept of having multiple sites in the unit cell using the brick lattice. After this we treat the triangular lattice. Finally we present the Kagome and dice lattices.

2.1.1 The brick lattice

Constructing periodicity using a unit cell in the square lattice was trivial. The brick lattice (also called the brick-wall lattice) will be the first lattice we treat where we have to extend the unit cell to regain periodicity.

The brick lattice is shown in Figure 8. A way to construct this lattice from the square lattice is to remove every other vertical bond. Each site can be labeled using the same coordinate system as for the square lattice, but not all sites are equivalent. In essence, we have two species: sites where along the y-axis a particle can only hop upwards (labeled **A**), or sites where it can only do so downwards (labeled **B**) The result is a lattice of alternating **A** and **B** sites, whose bonds establish the brick lattice structure.
The lattice unit vectors are the same as for the square lattice. To be able to construct the Bloch Hamiltonian we need translational invariance. This time, the directions we can hop differ from sublattice species **A** to **B**: on **A** we can hop along $\pm\boldsymbol{\delta}_1$ and $+\boldsymbol{\delta}_2$, on **B** along $\pm\boldsymbol{\delta}_1$ and $-\boldsymbol{\delta}_2$. To be able to describe both species with a Hamiltonian, we use the operators $a^{(\dagger)}_{\boldsymbol{x}_A}$ and $b^{(\dagger)}_{\boldsymbol{x}_B}$ where the first operator annihilates/creates a particle on sublattice **A** and the second operator on sublattice **B**.

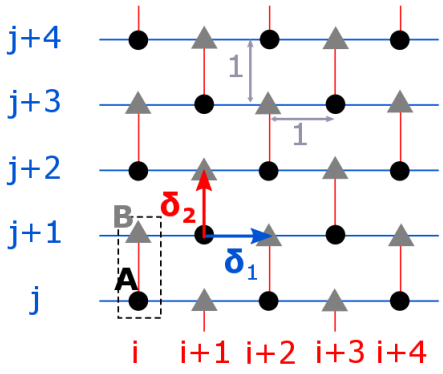

Figure 8: The brick lattice. The circle **A** and the triangle **B** make up the unit cell from which the lattice can be constructed.

We now start from the Hamiltonian in real space, as in Equation (1), where we take into account that a particle can only hop between different sublattices:

$$
\begin{aligned}
H &= \frac{1}{2}\left(H_A + H_B\right); \\
H_A &= -J \sum_{\boldsymbol{x}_A} \left[\left(a^\dagger_{\boldsymbol{x}_A} b_{\boldsymbol{x}_A + \boldsymbol{\delta}_1} + \text{H.c.} \right) + a^\dagger_{\boldsymbol{x}_A} b_{\boldsymbol{x}_A + \boldsymbol{\delta}_2} \right], \\
H_B &= -J \sum_{\boldsymbol{x}_B} \left[\left(b^\dagger_{\boldsymbol{x}_B} a_{\boldsymbol{x}_B + \boldsymbol{\delta}_1} + \text{H.c.} \right) + b^\dagger_{\boldsymbol{x}_B} a_{\boldsymbol{x}_B - \boldsymbol{\delta}_2} \right].
\end{aligned}
\tag{22}
$$

The factor $\frac{1}{2}$ is to correct for double-counting. Each site of sublattice **A** has equal surroundings, as does sublattice **B**. So this structure is Bravais, and we can transform to momentum space. The discrete Fourier transform of $b^{(\dagger)}_{\boldsymbol{x}}$ is defined the same as in Equation (3). The Hamiltonian in $\boldsymbol{k}$-space becomes:

$$
\begin{aligned}
H &= -\frac{J}{2} \sum_{\boldsymbol{k}} \left[\left(e^{i\boldsymbol{k}\cdot\boldsymbol{\delta}_1} + e^{-i\boldsymbol{k}\cdot\boldsymbol{\delta}_1} + e^{i\boldsymbol{k}\cdot\boldsymbol{\delta}_2} \right) a^\dagger_{\boldsymbol{k}} b_{\boldsymbol{k}} + \left(e^{i\boldsymbol{k}\cdot\boldsymbol{\delta}_1} + e^{-i\boldsymbol{k}\cdot\boldsymbol{\delta}_1} + e^{-i\boldsymbol{k}\cdot\boldsymbol{\delta}_2} \right) b^\dagger_{\boldsymbol{k}} a_{\boldsymbol{k}} \right] \\
&= -\frac{J}{2} \sum_{\boldsymbol{k}} \left[\left(2\cos k_x + e^{ik_y} \right) a^\dagger_{\boldsymbol{k}} b_{\boldsymbol{k}} + \left(2\cos k_x + e^{-ik_y} \right) b^\dagger_{\boldsymbol{k}} a_{\boldsymbol{k}} \right].
\end{aligned}
$$

We now rewrite this in matrix notation as

$$
H = \sum_{\boldsymbol{k}} \begin{pmatrix} a^\dagger_{\boldsymbol{k}} & b^\dagger_{\boldsymbol{k}} \end{pmatrix} \mathcal{H}_{\boldsymbol{k}} \begin{pmatrix} a_{\boldsymbol{k}} \\ b_{\boldsymbol{k}} \end{pmatrix},
\tag{23}
$$

where

$$
\mathcal{H}_{\boldsymbol{k}} = -\frac{J}{2} \begin{pmatrix} 0 & 2\cos k_x + e^{-ik_y} \\ 2\cos k_x + e^{ik_y} & 0 \end{pmatrix}.
\tag{24}
$$

Note that the matrix elements on the diagonal are zero, corresponding to the fact that the particles cannot hop from **A** (**B**) to itself.
In this way one can construct the Bloch Hamiltonian from which the energy bands and eigenstates can be computed in a quick and intuitive way. We will use this below for the Kagome and Dice lattice.

As before, the Bloch Hamiltonian gives the energy spectrum by computing the eigenvalues:

$$
\varepsilon_\pm = \pm \frac{J}{2} \sqrt{3 + 2\cos(2k_x) + 4\cos k_x \cos k_y}.
\tag{25}
$$

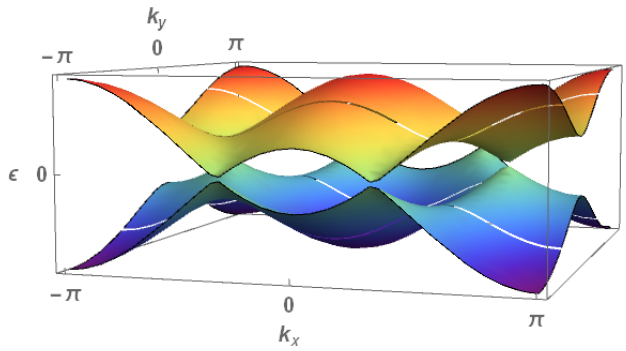

Figure 9: The two energy bands for the brick lattice for $J \neq 0$; it is symmetric for $J < 0$ and $J > 0$.

Because the Bloch Hamiltonian has a 2×2-matrix structure, there are two solutions for the eigenvalues. This corresponds to the presence of two energy bands, as shown in Figure 9. In general, when a unit cell contains n sites the energy spectrum will consist of n energy bands.
Another interesting property of this spectrum is that the bands touch at $\varepsilon_\pm = 0$ for $k_x = \pm\frac{2\pi}{3}$, $k_y \in \{0, \pm\pi\}$. At these points the dispersion relation is linear and the eigenvalues are degenerate: they are called *Dirac points*. The brick lattice has four of these Dirac points on the edges of its first Brillouin zone, which are normally known from the spectrum of graphene. Indeed one can see that the brick lattice is just a deformation of the hexagonal lattice and therefore has a similar energy spectrum.

2.1.2 The triangular lattice

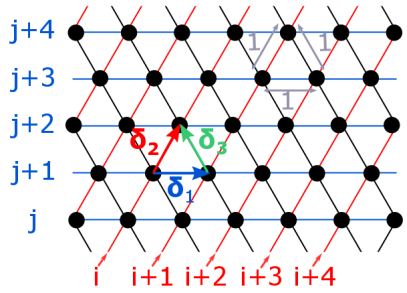

Figure 10: The triangular lattice.

On the left in Figure 10 we show the triangular lattice, built from equilateral triangles with sides of length 1. This lattice can be viewed as a tilted version of the square lattice with an extra diagonal bond.
Due to the extra diagonal bond, there are now three distinct lattice unit vectors:

$$\boldsymbol{\delta}_1 = (1, 0), \ \boldsymbol{\delta}_2 = \left(\frac{1}{2}, \frac{\sqrt{3}}{2}\right) \text{ and } \boldsymbol{\delta}_3 = \left(-\frac{1}{2}, \frac{\sqrt{3}}{2}\right). \tag{26}$$

Again we use these vectors to compute the Bloch Hamiltonian. At every site we can now hop in all six directions $\pm\boldsymbol{\delta}_1$, $\pm\boldsymbol{\delta}_2$, $\pm\boldsymbol{\delta}_3$. Because translational invariance is immediate for an infinite number of lattice sites, we see that

$$\begin{aligned} \mathcal{H}_{\boldsymbol{k}} = \varepsilon &= -2J \left(\cos \boldsymbol{k} \cdot \boldsymbol{\delta}_1 + \cos \boldsymbol{k} \cdot \boldsymbol{\delta}_2 + \cos \boldsymbol{k} \cdot \boldsymbol{\delta}_3\right) \\ &= -2J \left(\cos k_x + 2 \cos \frac{k_x}{2} \cos \frac{\sqrt{3} k_y}{2}\right). \end{aligned} \tag{27}$$

In Figure 11 we plot the energy spectrum.

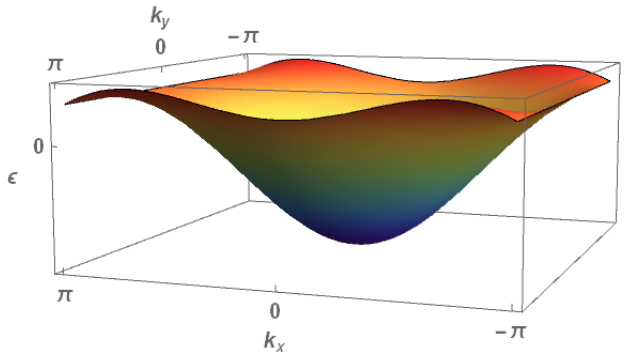

Figure 11: The single energy band for the triangular lattice for $J > 0$.

2.1.3 The Kagome lattice

A variation on the triangular lattice with a multiple-site unit cell is the Kagome lattice (shown in Figure 12). The unit cell is a triangle of three sites, and this unit cell is placed on a triangular lattice structure. Therefore the lattice unit vectors are the same as for the triangular lattice. Connecting only nearest neighbour sites results in the Kagome structure. Now we can distinguish three different sublattice species characterized as indicated below.

A $\Rightarrow$ $\pm\boldsymbol{\delta}_1, \pm\boldsymbol{\delta}_2$
B $\Rightarrow$ $\pm\boldsymbol{\delta}_1, \pm\boldsymbol{\delta}_3$
C $\Rightarrow$ $\pm\boldsymbol{\delta}_2, \pm\boldsymbol{\delta}_3$

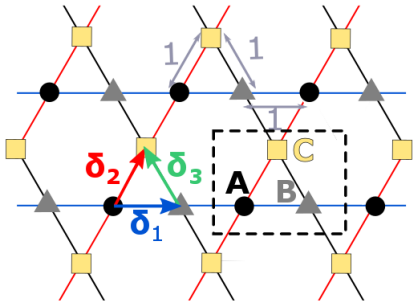

Figure 12: The Kagome lattice. The unit cell consists of three sublattice species on the corners of a triangle: the circle **A**, the triangle **B** and the square **C**.

We will not attempt to put a coordinate system on this lattice, because we can immediately construct the Hamiltonian in momentum space. As for the brick lattice - where the Hamiltonian became a 2×2 matrix - this implies that our Hamiltonian is now a 3×3 matrix in $\boldsymbol{k}$-space:

$$H = \sum_{\boldsymbol{k}} \begin{pmatrix} a_{\boldsymbol{k}}^\dagger & b_{\boldsymbol{k}}^\dagger & c_{\boldsymbol{k}}^\dagger \end{pmatrix} \mathcal{H}_{\boldsymbol{k}} \begin{pmatrix} a_{\boldsymbol{k}} \\ b_{\boldsymbol{k}} \\ c_{\boldsymbol{k}} \end{pmatrix}, \tag{28}$$

with

$$\mathcal{H}_{\boldsymbol{k}} = -J \begin{pmatrix} 0 & \cos \boldsymbol{k} \cdot \boldsymbol{\delta}_1 & \cos \boldsymbol{k} \cdot \boldsymbol{\delta}_2 \\ \cos \boldsymbol{k} \cdot \boldsymbol{\delta}_1 & 0 & \cos \boldsymbol{k} \cdot \boldsymbol{\delta}_3 \\ \cos \boldsymbol{k} \cdot \boldsymbol{\delta}_2 & \cos \boldsymbol{k} \cdot \boldsymbol{\delta}_3 & 0 \end{pmatrix}. \tag{29}$$

This matrix has three eigenvalues, corresponding to three energy bands:

$$\begin{aligned} \epsilon_1 &= J, \\ \epsilon_{2,3} &= -\frac{J}{2} \left(1 \pm \sqrt{3 + 2\cos(2k_x) + 4 \cos k_x \cos(\sqrt{3} k_y)} \right). \end{aligned} \tag{30}$$

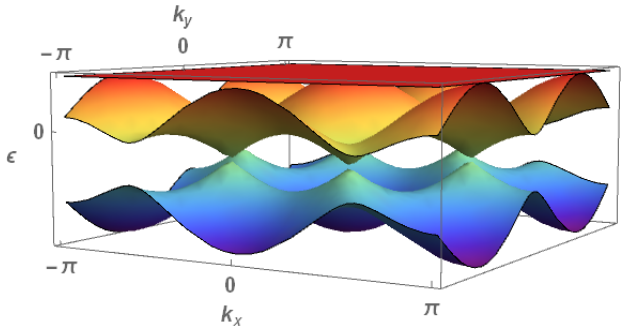

Figure 13: Energy bands of the Kagome lattice for $J > 0$, consisting of two brick-like bands with an additional flat band.

Note that ϵ_1 is independent of k_x, k_y and therefore constant in $\boldsymbol{k}$-space.

As can be seen from Figure 13 the highest energy band is a *flat band*. As for the brick lattice, the two lower bands are touching in Dirac-like points. In addition to that the flat band touches with the middle bands at several points. Further on in this chapter we will see that by applying a magnetic perturbation, we can put the flat band on the bottom of the energy spectrum as well as lift the degeneracy. This is beneficial because for the tight-binding approimation to be valid in optical lattices, we need to be in or close to the groundstate level of the system.

Flat bands A flat band is a highly degenerate energy level. The energy is constant and equal for every value of $\boldsymbol{k}$, so states in this energy band are *non-dispersive* as the group velocity equals zero: $v_g = \partial\varepsilon_1/\partial\boldsymbol{k} = 0$.
The Kagome spectrum acquires a flat band naturally by the way the lattice is structured. It can be shown that wavepackets located on the hexagonal ring cannot propagate out of this ring.

We give an qualitative explanation by looking at the structure in Figure 14. Consider a wavepacket on the hexagonal ring that has positive and negative amplitude for every other site. Any site just outside the hexagonal loop is coupled to two sites in the hexagon (e.g. in the unit cell: **A** outside the hexagon couples to two sites **B** and **C** in the hexagonal loop), where both bonds have equal strength. When time evolves, the wavepacket will propagate to this site using the bonds. But on the site their contributions cancel out. This is true for every particle outside the hexagonal ring, and so the wavepacket will always interfere destructively with itself. Therefore this particle is locked in and cannot propagate through the lattice [10]. This self-localization is responsible for the flat band in the energy spectrum.

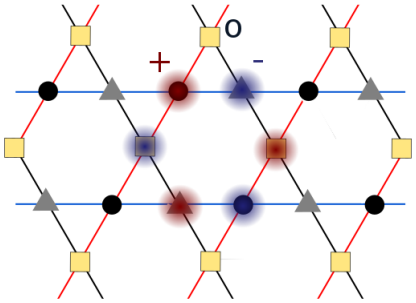

Figure 14: A self-localized wavepacket on the hexagonal ring of the Kagome lattice.

2.1.4 The dice lattice

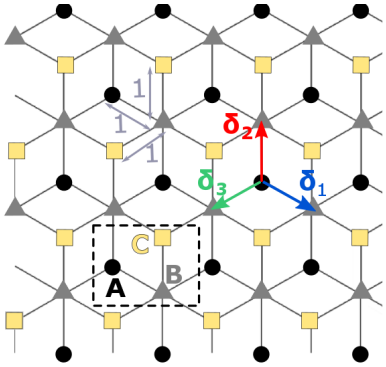

Figure 15: The dice lattice, which owes its name to the fact that it looks like threedimensional dice projected into the plane. The unit cell consists of three sublattice species: the circle **A**, the triangle **B** and the square **C**.

The final lattice to be considered in this thesis is the dice lattice. One can construct it by overlapping two hexagonal lattices, or by dividing up the plane into parallellograms with angles of 60° and 90°. The lattice unit vectors are:

$$\begin{aligned} \boldsymbol{\delta}_1 &= \left(\frac{\sqrt{3}}{2}, -\frac{1}{2}\right), \\ \boldsymbol{\delta}_2 &= (0, 1), \\ \boldsymbol{\delta}_3 &= \left(-\frac{\sqrt{3}}{2}, -\frac{1}{2}\right). \end{aligned} \tag{31}$$

The Dice lattice has three different sublattice species **A**, **B** and **C**, as shown in Figure 15:

$$\begin{array}{lcl} \mathbf{A} & \Rightarrow & +\boldsymbol{\delta}_1, +\boldsymbol{\delta}_2, +\boldsymbol{\delta}_3 \\ \mathbf{B} & \Rightarrow & \pm\boldsymbol{\delta}_1, \pm\boldsymbol{\delta}_2, \pm\boldsymbol{\delta}_3 \\ \mathbf{C} & \Rightarrow & -\boldsymbol{\delta}_1, -\boldsymbol{\delta}_2, -\boldsymbol{\delta}_3. \end{array}$$

Note that sublattices **A** and **C** are 3-fold coordinated, while **B** is 6-fold coordinated. For this reason **B** is called the *hub*-sublattice and **A**,**C** are called the *rim*-sublattices, like the rims of a wheel.
As for the Kagome lattice in Equation 28, the Bloch Hamiltonian for the Dice lattice is a 3×3-matrix. One can derive it has the following form:

$$\mathcal{H}_{\boldsymbol{k}} = -\frac{J}{2}\begin{pmatrix} 0 & e^{-i\boldsymbol{k}\cdot\boldsymbol{\delta}_1} + e^{-i\boldsymbol{k}\cdot\boldsymbol{\delta}_2} + e^{-i\boldsymbol{k}\cdot\boldsymbol{\delta}_3} & 0 \\ e^{i\boldsymbol{k}\cdot\boldsymbol{\delta}_1} + e^{i\boldsymbol{k}\cdot\boldsymbol{\delta}_2} + e^{i\boldsymbol{k}\cdot\boldsymbol{\delta}_3} & 0 & e^{-i\boldsymbol{k}\cdot\boldsymbol{\delta}_1} + e^{-i\boldsymbol{k}\cdot\boldsymbol{\delta}_2} + e^{-i\boldsymbol{k}\cdot\boldsymbol{\delta}_3} \\ 0 & e^{i\boldsymbol{k}\cdot\boldsymbol{\delta}_1} + e^{i\boldsymbol{k}\cdot\boldsymbol{\delta}_2} + e^{i\boldsymbol{k}\cdot\boldsymbol{\delta}_3} & 0 \end{pmatrix}. \tag{32}$$

From the fact that the diagonal as well as the anti-diagonal are zero, we can see that there is no hopping between the same sublattice species, and no hopping between **A** and **C** possible.

Diagonalization of the Bloch Hamiltonian gives the eigenvalues:

$$\begin{aligned} \epsilon_1 &= 0, \\ \epsilon_{2,3} &= \pm\frac{t}{\sqrt{2}}\left[3 + 2\cos\left(\sqrt{3}k_x\right) + 4\cos\left(\frac{\sqrt{3}}{2}k_x\right)\cos\left(\frac{3}{2}k_x\right)\right]^{\frac{1}{2}}. \end{aligned} \tag{33}$$

Once again we obtain a flat band as can be seen in Figure 16a, this time at zero energy.

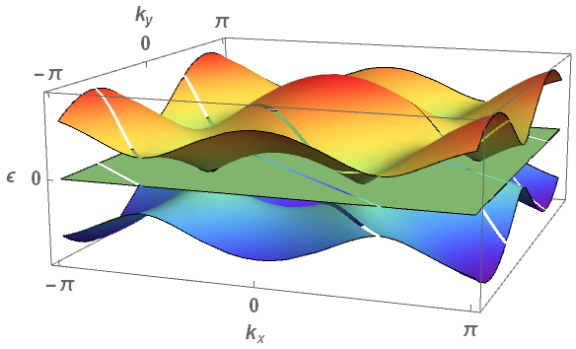

(a) The energy spectrum of the dice lattice for $J > 0$, with a flat band at zero energy.

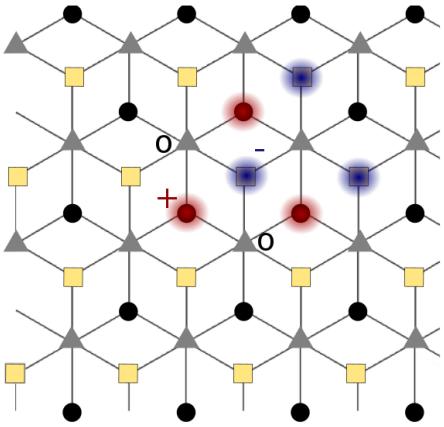

(b) The wavepacket present on sublattices **A** and **C** that interferes destructively with itself on sublattice **B**, creating a non-dispersive energy band.

Figure 16

Again this is self-localization due to destructive interference, for wavefunctions residing on sublattice **A** and **C** with equal weight but opposite phase for the two species. Their contributions will once more cancel out on the **B** sublattice [11].

2.2 Magnetic flux: hopping with a phase factor

In this section we extend the tight-binding model for a lattice in a magnetic field. We will see that we can account for the Aharonov-Bohm effect in second quantization by changing the hopping parameter from real-valued to complex-valued: $J \to Je^{i\phi} \in \mathbb{C}$.

Let us first introduce the formalism for charged particles moving in a magnetic field. For a two-dimensional lattice in a plane, we apply a magnetic field $\boldsymbol{B} = B\hat{\boldsymbol{z}}$ perpendicular to this plane. A magnetic field is linked to a vector potential $\boldsymbol{A}$ by $\boldsymbol{B} = \boldsymbol{\nabla} \times \boldsymbol{A}$. As usual we have the freedom of a gauge choice for $\boldsymbol{A}$, because the magnetic field $\boldsymbol{B}$ is not affected by transformations $\boldsymbol{A} \to \boldsymbol{A} + \boldsymbol{\nabla}\xi$ where ξ is a scalar. By definition the flux through a certain surface S is $\Phi = \int_S \boldsymbol{B} \cdot d\boldsymbol{S}$, and using Stokes' theorem this becomes $\Phi = \int_S (\boldsymbol{\nabla} \times \boldsymbol{A}) \cdot d\boldsymbol{S} = \oint_{\partial S} \boldsymbol{A} \cdot d\boldsymbol{\ell}$. Here ∂S is the edge of the surface S, and we define $\boldsymbol{\ell} = \partial \boldsymbol{S}$.
The effect of the magnetic field on the solution of the Schrödinger equation is taken into account by inserting minimal coupling $\boldsymbol{p} \to \boldsymbol{p} - \boldsymbol{A}$ into the Hamiltonian (we put $e = \hbar = 1$). It can be shown that the solution to the Schrödinger equation is then given by $\Psi' = e^{i\int_\ell \boldsymbol{A} \cdot d\boldsymbol{\ell}}\Psi = e^{i\Phi}\Psi$. The presence of a magnetic field expresses itself through the so-called Aharonov-Bohm phase factor in the wavefunction, with the phase equal to the enclosed flux [12]. Note that this is equivalent to the tranformation $H \to e^{i\Phi}H$.

To incorporate this Aharonov-Bohm phase into the language we have developed in Section 2.1, we use *Peierls substitution* [13]. Particles can move around the lattice by hopping from site to site using the present bonds, and in this way enclose a certain flux. To take this into account we substitute $J \to Je^{i\phi}$, where ϕ is strongly dependent on the gauge choice for $\boldsymbol{A}$ and on the direction of hopping. When moving around a plaquette, the hopping parameters are multiplied and the different Peierls phases are added. They need to be constructed in such a way that their sum equals the enclosed flux through the surface according to the Aharonov-Bohm theory:

$$\left(Je^{i\phi_1}\right)\left(Je^{i\phi_2}\right)\ldots\left(Je^{i\phi_m}\right) = J^m e^{i(\phi_1+\phi_2+\ldots+\phi_m)} = J^m e^{i\Phi}. \tag{34}$$

Determining the value for all ϕ_i is equivalent to choosing a gauge for $\boldsymbol{A}$.
We now compute the simplest case of magnetic flux for the square lattice, and then apply this technique to the lattice structures discussed in Section 2.1 and for different strengths of the magnetic flux.

2.2.1 The square lattice

We characterize the strength of the magnetic field by considering the flux through a unit plaquette of the lattice. In the case of the square lattice that means a square with a surface area of 1^2. We focus on enclosed fluxes per plaquette $\Phi \in [0, 2\pi\rangle$. To start we consider the case where $\Phi = \pi$.

For the direction of the magnetic field we have a gauge freedom. Recall that the square lattice has unit vectors $\boldsymbol{\delta}_1 = (1, 0)$ and $\boldsymbol{\delta}_2 = (0, 1)$. Due to the structure of the square lattice it is beneficial to choose a Landau gauge:

$$\boldsymbol{A}(x) = -Bx \begin{pmatrix} 0 \\ 1 \\ 0 \end{pmatrix}. \tag{35}$$

This adds a Peierls phase only when hopping along the y-axis but breaks translational invariance along the x-axis. We will see below that we can retrieve periodicity in the lattice by enlarging the unit cell.

Flux $\Phi = \pi$ First we consider the case in which the enclosed flux around a plaquette equals π. Using the gauge given above, the hopping strength in the x-direction is always J. In the y-direction, the hopping strength obtains a phase factor that depends on the x-coordinate of the lattice site $\boldsymbol{x} = ij$ (consider once more Figure 5 in Section **??**). If we now move around a plaquette starting at lattice site ij, and assume the hopping strength at that site is J in the x-direction and $Je^{iA_y(i)}$ in the y-direction:

$$ij \xrightarrow{J} (i+1)j \xrightarrow{Je^{iA_y(i+1)}} (i+1)(j+1) \xrightarrow{J} i(j+1) \xrightarrow{Je^{-iA_y(i)}} ij. \tag{36}$$

The total acquired hopping strength is $J^4 e^{i[A_y(i+1) - A_y(i)]}$. Now we choose $A_y(i) = \pi(i-1)$ and $A_y(i+1) = \pi i$ such that the phase factor in the total hopping strength equals $e^{i\pi}$, as desired.
Extending this to the whole lattice, for *hopping in the y-direction* (i.e. along $\boldsymbol{\delta}_2$) we have $J_{i+1} = J_i e^{i\pi}$.

Note that if we move up two sites in the x-direction, $J_{i+2} = J_{i+1}e^{i\pi} = J_i e^{i2\pi} = J_i$. Therefore we expect that periodicity is recovered when we enlarge the unit cell to two sites along the x-direction. Call these two sublattices **A** and **B**. For hopping along $\boldsymbol{\delta}_2$, on sublattice **A** the hopping strength is J and on **B** it is $Je^{i\pi}$. For hopping along $\boldsymbol{\delta}_1$ the hopping strength is J for both sublattices **A** and **B**. This setup is shown in Figure 17. When we hop in the $-y$-direction on sublattice **B** we have to take the complex conjugate of the hopping strength, such that the phase π is subtracted instead of added: $Je^{-i\pi}$.

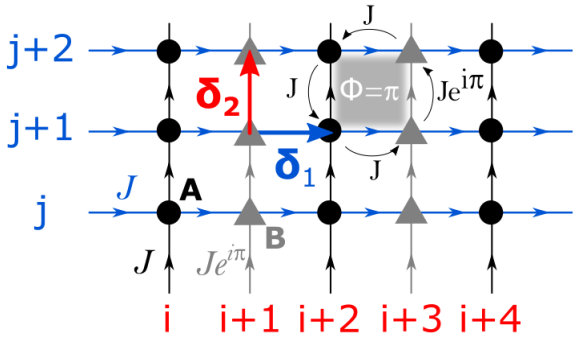

Figure 17: The setup for creating a π-flux per unit plaquette for the square lattice. In the top right it is shown that indeed a total phase of π is acquired in the hopping when moving around a square unit plaquette. Moving around two plaquettes gives the identity, $e^{i2\pi} = 1$, showing that we have doubled the size of our unit cell.

Now we use this to construct the Hamiltonian:

$$H = \frac{1}{2}\left(H_A + H_B\right); \tag{37}$$

$$H_A = -J\sum_{\boldsymbol{x}_A}\left[a^\dagger_{\boldsymbol{x}_A} b_{\boldsymbol{x}_A+\boldsymbol{\delta}_1} + a^\dagger_{\boldsymbol{x}_A} a_{\boldsymbol{x}_A+\boldsymbol{\delta}_2} + \text{H.c.}\right],$$

$$H_B = -J\sum_{\boldsymbol{x}_B}\left[b^\dagger_{\boldsymbol{x}_B} a_{\boldsymbol{x}_B+\boldsymbol{\delta}_1} + e^{-i\pi} b^\dagger_{\boldsymbol{x}_B} b_{\boldsymbol{x}_B+\boldsymbol{\delta}_2} + \text{H.c.}\right]. \tag{38}$$

The structure is periodic for this unit cell, so we can transform to momentum space:

$$H = -J\sum_{\boldsymbol{k}}\left[a^\dagger_{\boldsymbol{k}} a_{\boldsymbol{k}} \cos\boldsymbol{k}\cdot\boldsymbol{\delta}_2 + b^\dagger_{\boldsymbol{k}} b_{\boldsymbol{k}} \cos\left(\boldsymbol{k}\cdot\boldsymbol{\delta}_2 + \pi\right) + a^\dagger_{\boldsymbol{k}} b_{\boldsymbol{k}} \cos\boldsymbol{k}\cdot\boldsymbol{\delta}_1 + b^\dagger_{\boldsymbol{k}} a_{\boldsymbol{k}} \cos\boldsymbol{k}\cdot\boldsymbol{\delta}_1\right]. \tag{39}$$

Writing this into matrix form gives us

$$H = \sum_{\boldsymbol{k}} \begin{pmatrix} a^\dagger_{\boldsymbol{k}} & b^\dagger_{\boldsymbol{k}} \end{pmatrix} \mathcal{H}_{\boldsymbol{k}} \begin{pmatrix} a_{\boldsymbol{k}} \\ b_{\boldsymbol{k}} \end{pmatrix}, \tag{40}$$

where $\mathcal{H}_{\boldsymbol{k}}$ is the 2×2-matrix

$$\mathcal{H}_{\boldsymbol{k}} = -J\begin{pmatrix} \cos k_y & \cos k_x \\ \cos k_x & \cos\left(k_y+\pi\right) \end{pmatrix}. \tag{41}$$

Note that every entry of the matrix can still be derived immediately using Figure 17, where one has to take into account the displacement vector $\boldsymbol{\delta}_i$ *and* a possible phase factor.
The eigenvalues of this matrix give the following two energy bands which are shown in Figure 18:

$$\varepsilon_{1,2} = \pm\frac{J}{\sqrt{2}}\sqrt{2+\cos\left(2k_x\right)+\cos\left(2k_y\right)}. \tag{42}$$

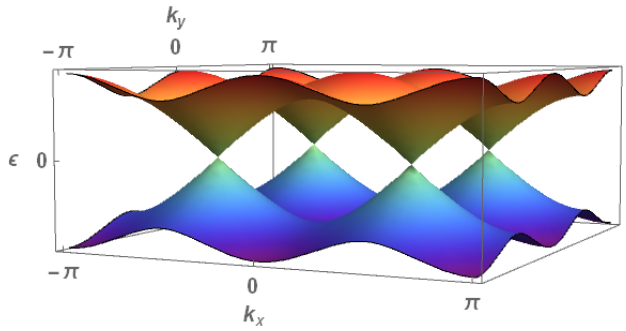

Figure 18: The energy spectrum for the square lattice with flux per unit plaquette $\Phi = \pi$ and $J \neq 0$.

Flux $\Phi = \dfrac{2\pi}{3}$ We now adapt the technique from the previous paragraph to achieve a flux per unit plaquette of $2\pi/3$. This means we demand that along the y-axis $J_{i+1} = J_i e^{i2\pi/3}$. Observe that we now need to move up three sites in the x-direction to obtain a phase difference of 2π. Therefore we insert three sublattices **A**, **B** and **C** to recover the translational invariance in both directions. The construction is displayed in Figure 19.

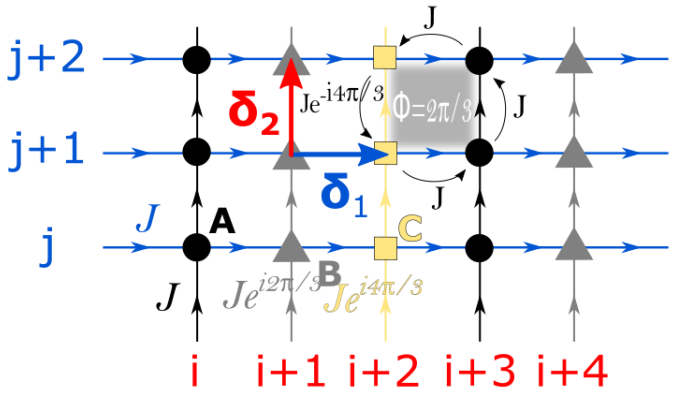

Figure 19: The setup for creating a $2\pi/3$-flux per unit plaquette for the square lattice. Moving around three plaquettes gives total phase factor of 1, showing that we have tripled the size of our unit cell.

For hopping along $\boldsymbol{\delta}_2$, on sublattice **A** the hopping strength is J, on **B** it is $Je^{i2\pi/3}$ and on **C** it is $Je^{i4\pi/3}$. For hopping along $\boldsymbol{\delta}_1$ the hopping strength is J for all sublattices **A**, **B** and **C**.
We use this structure to immediately rewrite the Hamiltonian in $\boldsymbol{k}$-space in matrix form,

$$H = \sum_{\boldsymbol{k}} \begin{pmatrix} a_{\boldsymbol{k}}^\dagger & b_{\boldsymbol{k}}^\dagger & c_{\boldsymbol{k}}^\dagger \end{pmatrix} \mathcal{H}_{\boldsymbol{k}} \begin{pmatrix} a_{\boldsymbol{k}} \\ b_{\boldsymbol{k}} \\ c_{\boldsymbol{k}} \end{pmatrix}, \tag{43}$$

where the Bloch Hamiltonian is derived to be equal to

$$\mathcal{H}_{\boldsymbol{k}} = -\frac{J}{2} \begin{pmatrix} 2\cos k_y & e^{ik_x} & e^{-ik_x} \\ e^{-ik_x} & 2\cos(k_y + 2\pi/3) & e^{ik_x} \\ e^{ik_x} & e^{-ik_x} & 2\cos(k_y + 4\pi/3) \end{pmatrix}. \tag{44}$$

This gives us three energy bands. As the expressions for the eigenvalues are quite involved, we will not show them here and only plot them as a function of $\boldsymbol{k}$ in Figure 20.

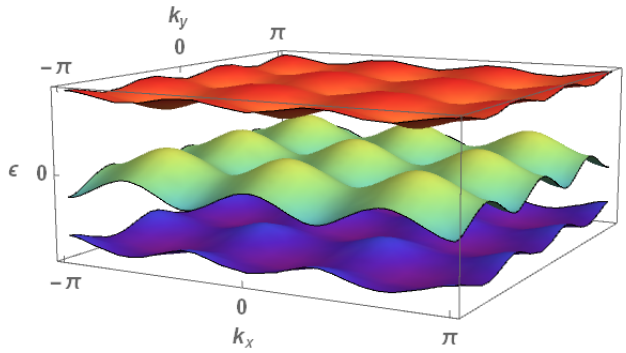

Figure 20: The energy spectrum for the square lattice with a flux of $\Phi = 2\pi/3$ per unit plaquette and $J > 0$.

The square lattice with $2\pi/3$-flux is the first model we encounter that has nontrivial Chern numbers. We compute them using the method developed in Section 1.3.
Because the unit cell has tripled in the x-direction, the Brillouin zone becomes three times smaller in that direction: $(k_x, k_y) \in [0, 2\pi/3] \times [0, 2\pi]$.

For the $\boldsymbol{k}$-grid with parameters $q_x = 3,\ q_y = 1,\ N_x = 9, N_y = 27$ we find the following result:

$$\begin{aligned} c_1 &= 1 \\ c_2 &= -2 \\ c_3 &= 1 \end{aligned} \tag{45}$$

Indeed one sees that $c_1 + c_2 + c_3 = 0$.

2.2.2 The brick lattice

Now we examine if the strategy we have developed for the square lattice, can be extended to the brick lattice. We expect the extension to be natural as their structures are much alike. The unit plaquette is now a rectangle of area $2 \cdot 1^2$.

Flux $\Phi = \pi$ This is equivalent to putting a flux of $\pi/2$ through every square plaquette. So along the y-axis we have $J_{i+1} = J_i e^{i\pi/2}$. The construction shown in Figure 21a needs 8 sublattices **A**, **B**,...,**H** to retrieve periodicity.

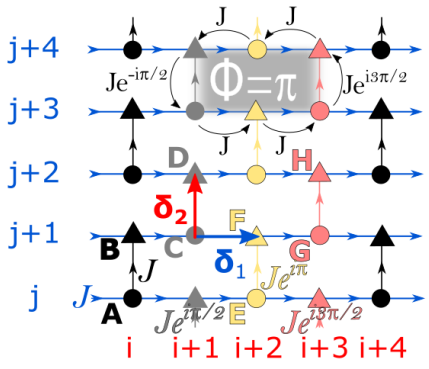

(a) A setup for creating a π-flux per unit plaquette for the brick lattice.

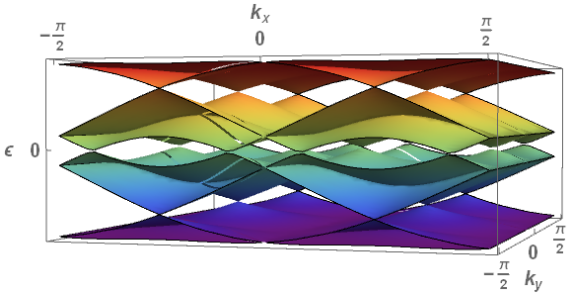

(b) The corresponding energy spectrum as a function of $\boldsymbol{k}$ plotted for $\boldsymbol{k} \in [-\pi/2, \pi/2] \times [-\pi/2, \pi/2]$.

As originally the brick lattice contained two sublattices, we see we have quadrupled the unit cell. Now this is a little unexpected, because we retrieve translational invariance by enclosing two rectangular plaquettes (which would correspond to doubling the unit cell). Furthermore, when we compute the energy bands from the 8×8 Bloch Hamiltonian matrix we observe that there are effectively 4 energy bands instead of 8 (see Figure 21b). These pairs of bands can be considered as one energy band because they cross each other multiple times, and do not only touch in Dirac points. This indicates that we can construct π-flux in the brick lattice in a more insightful way.

It turns out that it is indeed possible to solve this problem by using four sublattices, when we change the gauge and coordinate system. As in the end all physics is independent of these two, the results will not depend on which point of view we use to describe our lattice.
By putting a phase of 0 and π on each vertical bond alternately, we can obtain a flux of π through each rectangular plaquette with only 4 sublattice species (Figure 22a).

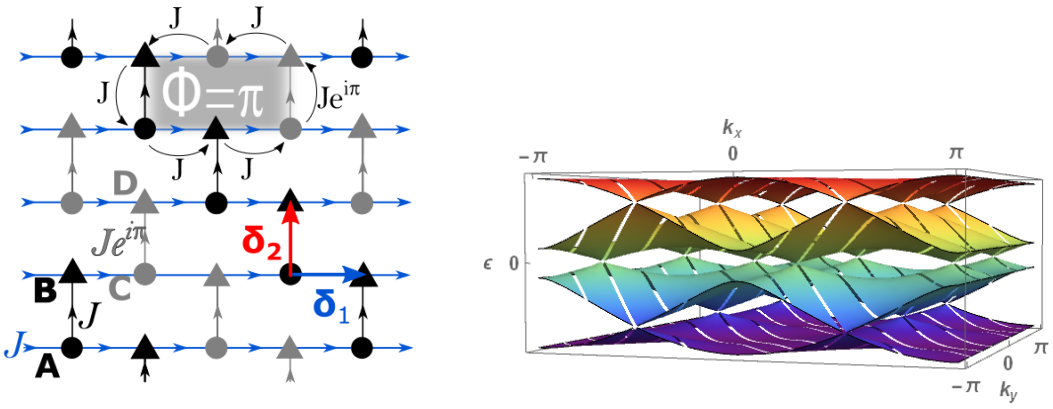

(a) Another setup using 4 lattice species instead of 8.

(b) The corresponding energy spectrum as a function of $\boldsymbol{k}$.

Figure 22

Now this setup requires a certain choice of coordinate system and gauge of the vector potential. But even without specifying them we can compute the Bloch Hamiltonian:

$$\mathcal{H}_{\boldsymbol{k}} = -t \begin{pmatrix} 0 & e^{-i\boldsymbol{k}\cdot\boldsymbol{\delta}_1} + e^{-i\boldsymbol{k}\cdot\boldsymbol{\delta}_2} & 0 & e^{i\boldsymbol{k}\cdot\boldsymbol{\delta}_1} \\ e^{i\boldsymbol{k}\cdot\boldsymbol{\delta}_1} + e^{i\boldsymbol{k}\cdot\boldsymbol{\delta}_2} & 0 & e^{-i\boldsymbol{k}\cdot\boldsymbol{\delta}_1} & 0 \\ 0 & e^{i\boldsymbol{k}\cdot\boldsymbol{\delta}_1} & 0 & e^{-i\boldsymbol{k}\cdot\boldsymbol{\delta}_1} + e^{-(\boldsymbol{k}\cdot\boldsymbol{\delta}_2+\pi)} \\ e^{-i\boldsymbol{k}\cdot\boldsymbol{\delta}_1} & 0 & e^{i\boldsymbol{k}\cdot\boldsymbol{\delta}_1} + e^{(\boldsymbol{k}\cdot\boldsymbol{\delta}_2+\pi)} & \end{pmatrix}. \tag{46}$$

The four corresponding eigenvalues are shown in Figure 22b. When compared with the spectrum in Figure 21b we see that indeed their shapes are the same. Note that for the Hamiltonian using 8 sublattices the Brillouin zone is twice as small as for the one using 4 sublattices. Therefore the spectra are equivalent when considering the eigenvalues of the first setup on a domain that is twice as small.

Flux $\Phi = \frac{4\pi}{3}$ As said before, the square lattice with $2\pi/3$ flux is topologically nontrivial. For this reason we also compute the brick lattice with $4\pi/3$ flux per rectangular plaquette. We can achieve this using the setup given in Figure 23a. Because we need a minimum of 6 sublattice species, the energy spectrum consists of 6 energy bands as shown in Figure 23b.

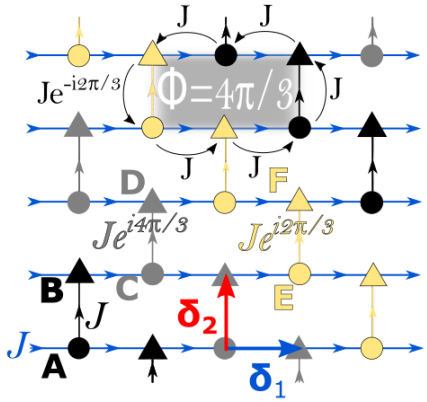

(a) The sublattice structure for the brick lattice with $4\pi/3$-flux per rectangular plaquette.

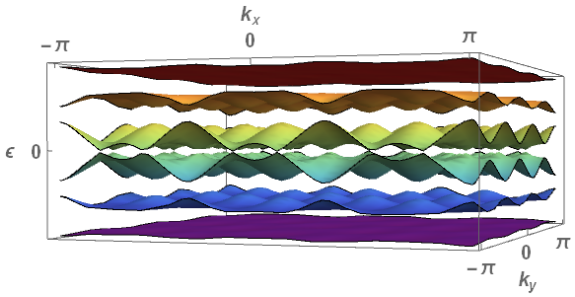

(b) The corresponding 6 energy bands for $J > 0$.

Figure 23

Because the unit cell contains 6 sites, the Brillouin zone is $[0, 2\pi/6] \times [0, 2\pi]$.

For a $\boldsymbol{k}$-grid with parameters $q_x = 6$, $q_y = 1$, $N_x = 12$, $N_y = 18$ we find the following result using the method from Section 1.3:

$$\begin{aligned} c_1 &= -1 & c_2 &= 2 \\ c_3 &= 0 & c_4 &= -2 \\ c_5 &= 2 & c_6 &= -1 \end{aligned} \tag{47}$$

2.2.3 The triangular lattice

We continue with flux on the triangular lattice (Figure 10). Recall that the unit lattice vectors are $\boldsymbol{\delta}_1 = (1,0)$, $\boldsymbol{\delta}_2 = \left(\frac{1}{2}, \frac{\sqrt{3}}{2}\right)$ and $\boldsymbol{\delta}_3 = \left(-\frac{1}{2}, \frac{\sqrt{3}}{2}\right)$. Note that we can hop around a triangular plaquette by following $\boldsymbol{\delta}_1 \to \boldsymbol{\delta}_3 \to -\boldsymbol{\delta}_2$.
From now on we try to construct a consistent setup of sublattices and hopping phases without specifying a gauge or coordinate system, as was done for the brick lattice.

Flux $\Phi = \pi$ As indicated before, the triangular lattice can be viewed as a tilted version of the square lattice with an extra diagonal bond. Note that a flux of π through a triangular plaquette corresponds to a flux of 2π through a (tilted) square plaquette (which we can describe without complex hopping). It is therefore natural to add complex hopping only on the extra diagonal bond, as shown in Figure 24a.

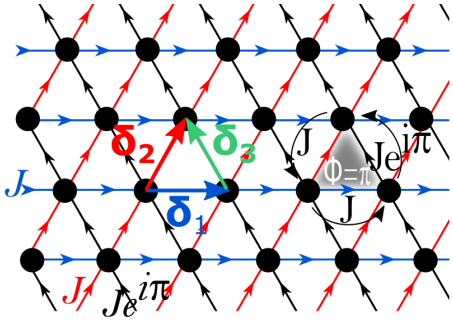

(a) By putting a hopping strength of $te^{i\pi}$ along every diagonal bond in the direction of $\boldsymbol{\delta}_3$, a flux of π through each plaquette is induced.

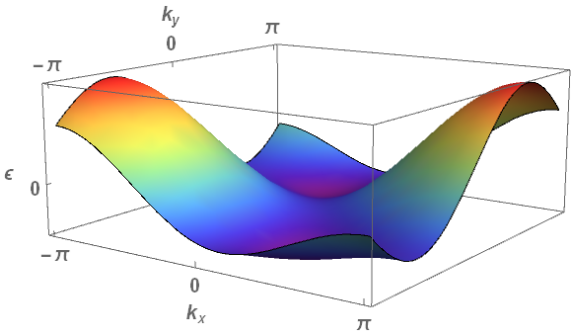

(b) The single energy band for π-flux per triangular plaquette with $J > 0$.

Figure 24

Indeed when moving around any triangular plaquette the hopping phases add up to a total of π. Observe that now translational invariance is immediate, because the surroundings of every site look the same: hopping along $\pm\boldsymbol{\delta}_{1,2}$ will always be with strength J, and along $\pm\boldsymbol{\delta}_3$ with strength $Je^{\pm i\pi}$. Therefore no extension of the unit cell is needed here. This conclusion makes sense when we skip back to the analogy with a tilted square lattice: π-flux through a triangular plaquette corresponds to 2π-flux through a (tilted) square. Thus the Hamiltonian will be a one-dimensional matrix:

$$H = -J \sum_{\boldsymbol{k}} a^\dagger_{\boldsymbol{k}} \left(e^{i\boldsymbol{k}\cdot\boldsymbol{\delta}_1} + e^{i\boldsymbol{k}\cdot\boldsymbol{\delta}_2} + e^{i(\boldsymbol{k}\cdot\boldsymbol{\delta}_3 + \pi)} + \text{H.c.} \right) a_{\boldsymbol{k}}. \tag{48}$$

The energy, plotted in Figure 24b, is equal to:

$$\varepsilon = -2J \left[\cos k_x - 2 \sin\left(k_x/2\right) \sin\left(\sqrt{3}k_y/2\right) \right]. \tag{49}$$

Flux $\Phi = \dfrac{2\pi}{3}$ As for the case of π-flux, we achieve a $2\pi/3$-flux by taking the hopping along $\boldsymbol{\delta}_1$ equal to J and alternate the strength along $\boldsymbol{\delta}_{2,3}$ with phase factors equal to multiples of $2\pi/3$. From Figure 25a one can see that we need 3 sublattice species **A**, **B** and **C** to retrieve translational invariance. Note that this agrees with the picture for the square lattice, where a $4\pi/3$-flux per square plaquette would imply the presence of 3 sublattices.

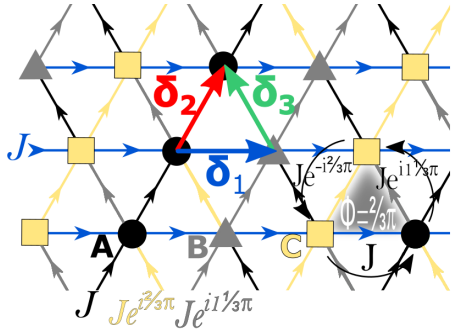

(a) The setup for inducing a flux of $2\pi/3$ through each triangular plaquette: the black arrows indicate hopping strength J, the yellow bonds $Je^{i2\pi/3}$ and the grey bonds $Je^{i4\pi/3}$.

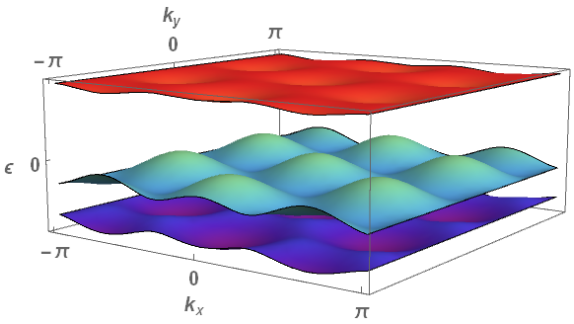

(b) The corresponding 3 energy bands for $J > 0$.

Figure 25

Using this one can derive that for

$$H = \sum_{\boldsymbol{k}} \begin{pmatrix} a_{\boldsymbol{k}}^\dagger & b_{\boldsymbol{k}}^\dagger & c_{\boldsymbol{k}}^\dagger \end{pmatrix} \mathcal{H}_{\boldsymbol{k}} \begin{pmatrix} a_{\boldsymbol{k}} \\ b_{\boldsymbol{k}} \\ c_{\boldsymbol{k}} \end{pmatrix}, \tag{50}$$

we have

$$\mathcal{H}_{\boldsymbol{k}} = -\frac{J}{2} \begin{pmatrix} 2\cos \boldsymbol{k}\cdot\boldsymbol{\delta}_2 & e^{-i\boldsymbol{k}\cdot\boldsymbol{\delta}_1} + e^{i(\boldsymbol{k}\cdot\boldsymbol{\delta}_3 + 2\pi/3)} & e^{i\boldsymbol{k}\cdot\boldsymbol{\delta}_1} + e^{-i(\boldsymbol{k}\cdot\boldsymbol{\delta}_3 + 4\pi/3)} \\ e^{i\boldsymbol{k}\cdot\boldsymbol{\delta}_1} + e^{-i(\boldsymbol{k}\cdot\boldsymbol{\delta}_3 + 2\pi/3)} & 2\cos\left(\boldsymbol{k}\cdot\boldsymbol{\delta}_2 + 4\pi/3\right) & e^{-i\boldsymbol{k}\cdot\boldsymbol{\delta}_1} + e^{i\boldsymbol{k}\cdot\boldsymbol{\delta}_3} \\ e^{-i\boldsymbol{k}\cdot\boldsymbol{\delta}_1} + e^{i(\boldsymbol{k}\cdot\boldsymbol{\delta}_3 + 4\pi/3)} & e^{i\boldsymbol{k}\cdot\boldsymbol{\delta}_1} + e^{-i\boldsymbol{k}\cdot\boldsymbol{\delta}_3} & 2\cos\left(\boldsymbol{k}\cdot\boldsymbol{\delta}_2 + 2\pi/3\right) \end{pmatrix}. \tag{51}$$

This expression solves for three energy bands, plotted in Figure 25b.

2.2.4 The Kagome lattice

Recall that the lattice unit vectors to move between the sublattices of the Kagome lattice are the same as for the triangular lattice.
Because it is a special version of the triangular lattice (see Figure 12), we expect the solutions to be very similar to the ones in the previous paragraph.

Flux $\Phi = \pi$ As for the triangular lattice, for every triangular plaquette in the Kagome lattice we choose two bonds along which no phase is picked up, and one bond with a phase of π. We can do this in a consistent manner by hopping along $\pm\boldsymbol{\delta}_{1,2}$ with strength J, while along $\pm\boldsymbol{\delta}_3$ we hop with strength $Je^{\pm i\pi}$. See Figure 26a.
Again translational invariance in immediate, as we can describe this setup with three sublattices **A**, **B** and **C** as for the zero-flux Kagome lattice. Also, note that the flux through a hexagonal plaquette is zero. As a hexagon consists of 6 triangles this equals $6 \times \pi = 0 \mod 2\pi$. This means this model can be implicated using a uniform magnetic field.

We can now derive our Bloch Hamiltonian:

$$\mathcal{H}_{\boldsymbol{k}} = -J \begin{pmatrix} 0 & \cos \boldsymbol{k}\cdot\boldsymbol{\delta}_1 & \cos \boldsymbol{k}\cdot\boldsymbol{\delta}_2 \\ \cos \boldsymbol{k}\cdot\boldsymbol{\delta}_1 & 0 & \cos\left(\boldsymbol{k}\cdot\boldsymbol{\delta}_3 + \pi\right) \\ \cos \boldsymbol{k}\cdot\boldsymbol{\delta}_2 & \cos\left(\boldsymbol{k}\cdot\boldsymbol{\delta}_3 + \pi\right) & 0 \end{pmatrix}. \tag{52}$$

This matrix has three energy eigenvalues:

$$\varepsilon_1 = -J,$$
$$\varepsilon_{2,3} = \frac{J}{2}\left[1 \pm \sqrt{3 + 2\cos\left(2k_x\right) + 4\cos k_x \cos\left(\sqrt{3}k_y\right)}\right]. \tag{53}$$

Comparing this to the eigenenergies for the Kagome lattice without any flux in Equation (30), they are the same apart from a minus sign. Due to the phase π that we put on bonds between sublattice **B** and **C**, those bonds become attractive instead of repulsive (or vice versa) as $e^{\pm i\pi} = -1$. We conclude that a π-flux per triangular plaquette in the Kagome lattice is equivalent to inverting the sign of the hopping. One can see that this puts the flat band on the bottom of the spectrum, which makes it more suitable for probing in optical lattice systems.

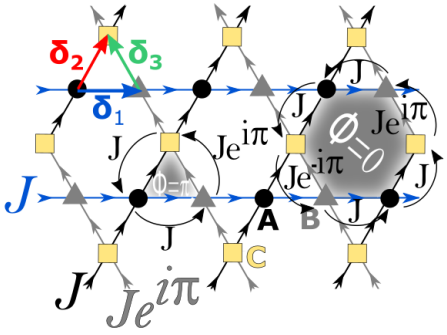

(a) The sublattice structure and hopping phases for π-flux through a triangular plaquette.

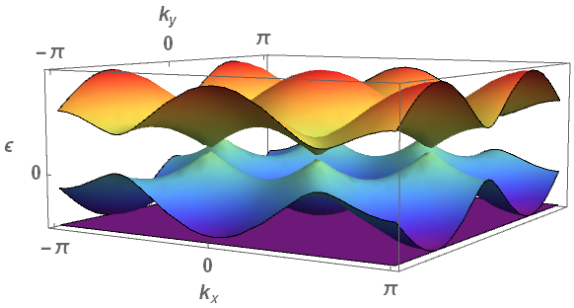

(b) The energy bands for $J > 0$, which is equivalent to the spectrum of Figure 13 mirrored in the plane $\varepsilon = 0$.

Figure 26

Flux $\Phi = \dfrac{2\pi}{3}$ For this case we can naturally extend the $2\pi/3$-flux for the triangular lattice to the Kagome lattice (Figure 27a). The phase attributed to taking a loop around a hexagon is $4\pi/3$. For a uniform magnetic field on would expect that the net flux is zero as $6 \times 2\pi/3 = 0 \mod 2\pi$. Therefore this model can not be implicated using a uniform magnetic field. As the chosen setup triples the size of our system - the same for the triangular lattice - we now need 9 sublattices to retrieve translational invariance. Our Bloch Hamiltonian will then be a 9×9-matrix (we will not show it here) with 9 different energy eigenvalues, plotted in Figure 27b.

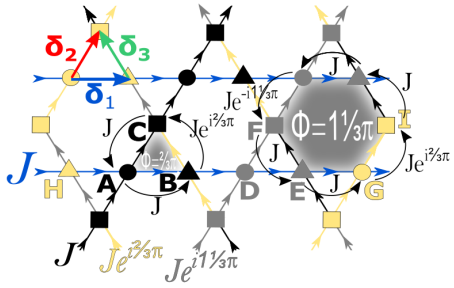

(a) The Kagome lattice for $2\pi/$-flux through a triangular plaquette with 9 sublattice species and three different hopping strengths.

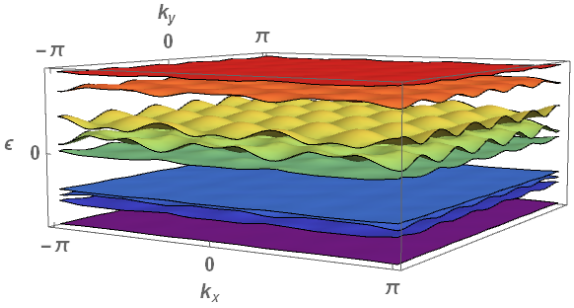

(b) The corresponding energy bands for $J > 0$.

Figure 27

When comparing this spectrum to that of Figure 13 where no magnetic field is present, we see that the degeneracy of the touching points has been lifted. This mean that each energy band has a well-defined Chern number.
The Brillouin zone of the Kagome lattice is the same as for the triangular lattice, as can be shown by constructing the so-called Wigner-Seitz cell. The width between two opposing sides of the hexagon is 2π. For $2\pi/3$-flux the unit cell size is tripled, and so the distance between the opposing sides becomes $2\pi/3$. We make a grid on the rectangle containing this hexagon as shown in Figure 28.

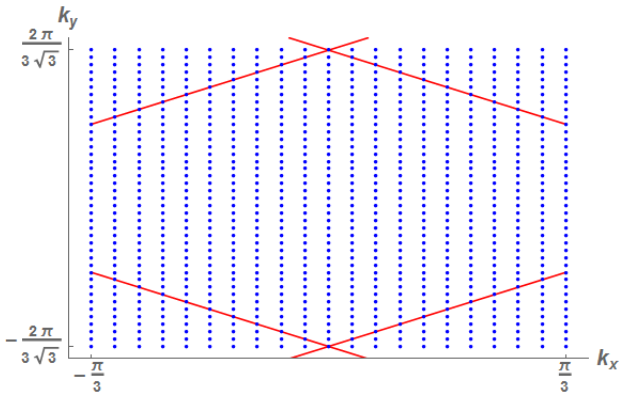

Figure 28: The grid in momentum space used to discretize the Brillouin zone for the Kagome lattice with $2\pi/3$-flux. For the mathematical details on the exact construction see Appendix B.2.

For certain points $\boldsymbol{k}_\alpha$ on this grid the expression in Equation 19 diverges, due to the denominator being equal to zero. Therefore we shift the lattice by an infinitesimal amount to perform the numerical computation.

By periodicity of the lattice the opposing sides of this hexagonal Brillouin zone are identified. Instead of the normal torus T^2 it has the topology of the double torus. It turns out that implementing these periodic boundary conditions is quite involved, so for practical reasons we split the plaquettes crossing over the borders in triangles (for a detailed description we refer to Appendix B.2). This gives the following results for the nine energy bands:

$$\begin{aligned} c_1 &= 1 & c_2 &= 1 & c_3 &= 1 \\ c_4 &= -2 & c_5 &= 1 & c_6 &= 1 \\ c_7 &= -2 & c_8 &= -2 & c_9 &= 1 \end{aligned} \tag{54}$$

Once again, the sum of the Chern numbers equals zero.
Besides the spectrum containing nondegenerate energy bands that are topologically nontrivial, it has several flat bands in the lower part of its energy spectrum. As these are the bands that we would use in an optical lattice setup, this spectrum is convenient for probing the effect of strong interactions on flat bands.

2.2.5 The dice lattice

In the dice lattice the parallelogrammatic plaquettes all have the same size, but three different possible orientations. Recall that the lattice unit vectors are $\boldsymbol{\delta}_1 = \left(\frac{\sqrt{3}}{2}, -\frac{1}{2}\right)$, $\boldsymbol{\delta}_2 = (0, 1)$ and $\boldsymbol{\delta}_3 = \left(-\frac{\sqrt{3}}{2}, -\frac{1}{2}\right)$. It is not as straightforward as before to induce certain values of flux using a complex hopping strength. We shall only derive the Hamiltonian for a π-flux per plaquette, and see that it has a very interesting property in the energy spectrum.

Flux $\Phi = \pi$ When making a loop around a plaquette in the dice lattice, we will always need only two of three lattice unit vectors. Both of them we use in positive *and* negative direction, e.g. $\boldsymbol{\delta}_1 \to \boldsymbol{\delta}_2 \to -\boldsymbol{\delta}_1 \to -\boldsymbol{\delta}_2$. This already shows that we need to at least double our unit cell in size, or the phase factors will always cancel out. Indeed we can construct a flux of π by using 6 sublattice species, as shown in Figure 29.

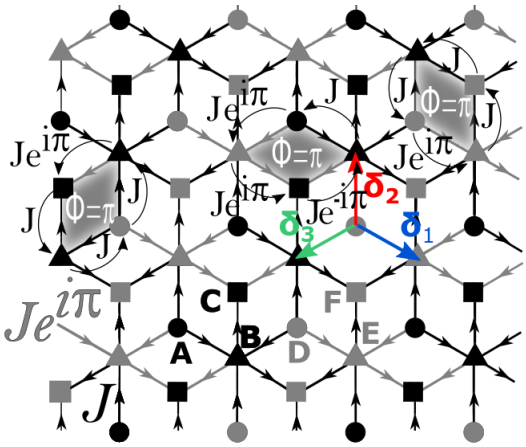

Figure 29: The sublattice structure and distribution of two different hopping strengths to obtain a π-flux per plaquette per the dice lattice.

Using this we construct the Bloch Hamiltonian:

$$\mathcal{H}_{\boldsymbol{k}} = -\frac{J}{2}\times$$

$$\begin{pmatrix}
0 & e^{-i\boldsymbol{k}\cdot\boldsymbol{\delta}_1} & 0 & 0 & e^{-i\boldsymbol{k}\cdot\boldsymbol{\delta}_2}+e^{-i(\boldsymbol{k}\cdot\boldsymbol{\delta}_3+\pi)} & 0 \\
e^{i\boldsymbol{k}\cdot\boldsymbol{\delta}_1} & 0 & e^{-i\boldsymbol{k}\cdot\boldsymbol{\delta}_2}+e^{-i(\boldsymbol{k}\cdot\boldsymbol{\delta}_3+\pi)} & e^{i\boldsymbol{k}\cdot\boldsymbol{\delta}_2}+e^{i\boldsymbol{k}\cdot\boldsymbol{\delta}_3} & 0 & e^{-i\boldsymbol{k}\cdot\boldsymbol{\delta}_1} \\
0 & e^{i\boldsymbol{k}\cdot\boldsymbol{\delta}_2}+e^{i(\boldsymbol{k}\cdot\boldsymbol{\delta}_3+\pi)} & 0 & 0 & e^{i(\boldsymbol{k}\cdot\boldsymbol{\delta}_1+\pi)} & 0 \\
0 & e^{-i\boldsymbol{k}\cdot\boldsymbol{\delta}_2}+e^{-i\boldsymbol{k}\cdot\boldsymbol{\delta}_3} & 0 & 0 & e^{-i(\boldsymbol{k}\cdot\boldsymbol{\delta}_1+\pi)} & 0 \\
e^{i\boldsymbol{k}\cdot\boldsymbol{\delta}_2}+e^{i(\boldsymbol{k}\cdot\boldsymbol{\delta}_3+\pi)} & 0 & e^{-i(\boldsymbol{k}\cdot\boldsymbol{\delta}_1+\pi)} & e^{i(\boldsymbol{k}\cdot\boldsymbol{\delta}_1+\pi)} & 0 & e^{-i\boldsymbol{k}\cdot\boldsymbol{\delta}_2}+e^{-i\boldsymbol{k}\cdot\boldsymbol{\delta}_3} \\
0 & e^{i\boldsymbol{k}\cdot\boldsymbol{\delta}_1} & 0 & 0 & e^{i\boldsymbol{k}\cdot\boldsymbol{\delta}_2}+e^{i\boldsymbol{k}\cdot\boldsymbol{\delta}_3} & 0
\end{pmatrix} \tag{55}$$

When we compute the 6 eigenvalues, we get the following surprising result:

$$\begin{aligned}
\varepsilon_1 &= 0, & \varepsilon_2 &= 0, \\
\varepsilon_3 &= -\sqrt{\frac{3}{2}}J, & \varepsilon_4 &= -\sqrt{\frac{3}{2}}J, \\
\varepsilon_5 &= \sqrt{\frac{3}{2}}J, & \varepsilon_6 &= \sqrt{\frac{3}{2}}J.
\end{aligned} \tag{56}$$

Therefore the dice lattice with a π-flux per unit plaquette has three flat bands in the energy spectrum, each with a degeneracy of 2 (see Figure 30a). This implies that every possible wavepacket present on the lattice interferes destructively with itself and is therefore locked in, making this setup an interesting system physically as it will be very sensitive to perturbations [14].

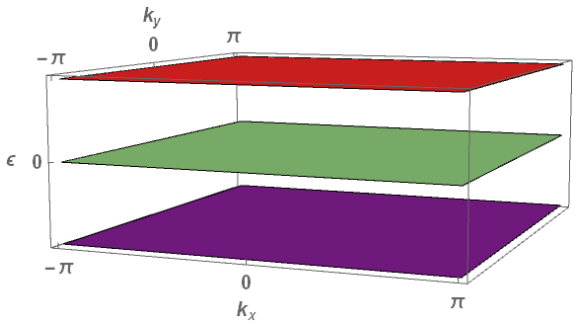

(a) The three 2-fold degenerate flat bands for the dice lattice with π-flux.

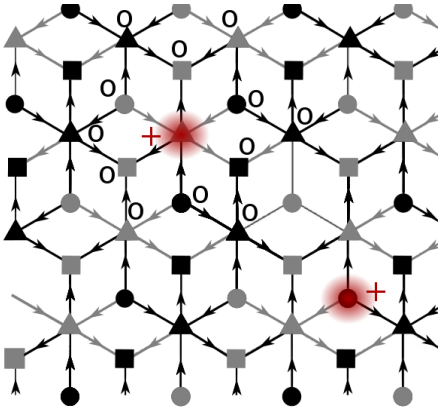

(b) Every wavepacket on the dice lattice interferes destructively with itself. The wavepacket can propagate to another site in two ways. Along one of them the wavefunction will pick up a phase factor $e^{\pm i\pi} = -1$, changing the amplitude from positive to negative.

Figure 30

In Figure 30b we show two examples of wavepackets localized on one site which interfere with themselves destructively in every direction, because of the phase $e^{i\pi}$ they pick up along one way. This switches positive amplitude to negative and vice versa. One can see that this is true for both the 3-fold and 6-fold coordinated sites.

2.3 Hofstadter butterfly

Before we start working on how to establish these lattice structures optically and induce a magnetic flux in the system, we generalize the computations of the energy spectrum as seen above for the square and triangular lattice. This will lead to a historically very important result: the *Hofstadter butterfly*. In 1976 Hofstadter publishes on the energy levels and wavefunctions of electrons in magnetic fields [15]. Specifically, for the example of a square lattice he shows that the allowed energy values as a function of the magnetic field results in a recursive pattern (the butterfly) which takes into account the symmetries of the lattice. This is the first example of a 'fractal' set, as Mandelbrot introduced the word 3 years after.

2.3.1 The square lattice

In the table below the results for the square lattice that we have computed up until now are summarized.

$\Phi = 2\pi\frac{p}{q}$	p	q	dimension of $\mathcal{H}_{\boldsymbol{k}}$
0 ($\hat{=}2\pi$)	1	1	1×1
π	1	2	2×2
$\frac{2\pi}{3}$	1	3	3×3

Note that we always look for $p, q \in \mathbb{N}$ that are relatively prime.

We see that the dimensions of the Hamiltonian is strongly linked to the value of q. This makes sense: for a flux of $2\pi/q$ we need to take q square plaquettes to retrieve translational invariance. Therefore the unit cell consists of q sites along the x-direction, and the Hamiltonian is a $q \times q$ matrix. Even for $p \neq 1$ the flux through q plaquettes will be $2\pi p$ which is just a multiple of 2π and therefore equivalent to zero.

We can conclude that for $\Phi = 2\pi p/q$ the Hamiltonian will be a $q \times q$-matrix. The unit cell consists of q sublattice species $S_m,\ m = 1, \ldots, q$. As before each S_m will connect to itself by $\pm\boldsymbol{\delta}_2$ with a phase factor of $2\pi\frac{p}{q}(m-1)$, as well as to its neighbours S_{m-1} by $-\boldsymbol{\delta}_1$ and S_{m+1} by $+\boldsymbol{\delta}_1$. Therefore the generalized matrix will have elements only on the diagonal, the off-diagonals and the corners (due to the periodicity of the lattice). Thus we derive the Hamiltonian to be as follows:

$$H = \sum_{\boldsymbol{k}} \begin{pmatrix} s^\dagger_{1,\boldsymbol{k}} & s^\dagger_{2,\boldsymbol{k}} & \ldots & s^\dagger_{q,\boldsymbol{k}} \end{pmatrix} \mathcal{H}_{\boldsymbol{k}} \begin{pmatrix} a_{1,\boldsymbol{k}} \\ a_{2,\boldsymbol{k}} \\ \vdots \\ a_{q,\boldsymbol{k}} \end{pmatrix}, \tag{57}$$

with

$$\mathcal{H}_{\boldsymbol{k}} = -\frac{J}{2}\times$$
$$\begin{pmatrix} 2\cos k_y & e^{ik_x} & 0 & 0 & & 0 & e^{-ik_x} \\ e^{-ik_x} & 2\cos\left(k_y + 2\pi\frac{p}{q}\right) & e^{ik_x} & 0 & & 0 & 0 \\ 0 & e^{-ik_x} & 2\cos\left(k_y + 2\pi\frac{p}{q}\cdot 2\right) & e^{ik_x} & \ldots & 0 & 0 \\ 0 & 0 & e^{-ik_x} & 2\cos\left(k_y + 2\pi\frac{p}{q}\cdot 3\right) & & 0 & 0 \\ & & \vdots & & \ddots & & \\ e^{ik_x} & 0 & 0 & 0 & \ldots & e^{-ik_x} & 2\cos\left(k_y + 2\pi\frac{p}{q}\cdot(q-1)\right) \end{pmatrix}. \tag{58}$$

The q eigenvalues of this matrix correspond to the energy bands. By plotting the image of the energy for all values $\Phi = 2\pi p/q,\ q = 1, \ldots, n$ where $n \in \mathbb{N}$ determines the resolution, we obtain the Hofstadter butterfly as shown in Figure 31. We can observe two symmetry axes. One is along $\varepsilon = 0$, showing that for every positive energy value there is also the negative one. Later in this work we will see that this a characteristic of a system that possesses *chiral symmetry*. The other symmetry axis is along $2\pi p/q = \pi$, because $e^{i2\pi p/q} = e^{-i2\pi(1-p/q)}$ such that $\varepsilon_\Phi = \varepsilon_{2\pi-\Phi}$. This basically shows that it is arbitrary if the magnetic field is in the direction of $+\hat{\boldsymbol{z}}$ or $-\hat{\boldsymbol{z}}$; the magnitude of the flux is what determines the physics.
Also note that when q is even, the two bands in the middle merge at $\varepsilon = 0$. This due to the bands touching at zero energy in the Dirac point at the edges of the Brillouin zone (as in Figure 18 for example).

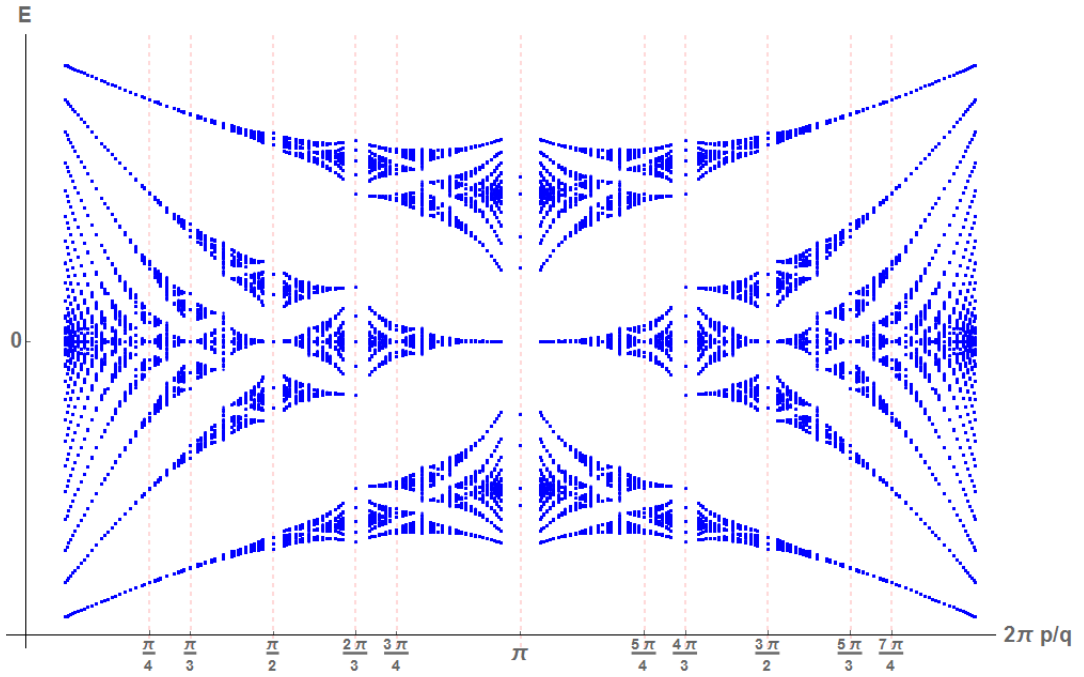

Figure 31: The Hofstadter butterfly for the square lattice.
We computed the energies for each fractional value of $\frac{p}{q}$, $p = 1, \ldots, q$; $q = 1, \ldots, 12$ on a grid in $\boldsymbol{k}$-space whose squares have sides of length $\frac{2\pi}{25}$.

2.3.2 The triangular lattice

To argue how many sublattices need to be introduced for the triangular lattice to induce translational invariance in the system, we refer back to the analogy with the square lattice. Translational invariance is obtained when the flux through a square plaquette equals a multiple of 2π, equivalent to a flux of π through a triangular plaquette. In the table below we compute the number of sublattices for some values of $\Phi_\triangle = \pi p/q$.

$\Phi_\triangle = \pi\frac{p}{q}$	$\Phi_\square = 2\pi\frac{p}{q}$	p	q	dimension of $\mathcal{H}_{\boldsymbol{k}}$
$0(\hat{=}2\pi)$	0	1	1	1×1
π	2π	1	1	1×1
$\pi/2$	π	1	2	2×2
$\pi/3$	$2\pi/3$	2	3	3×3
$2\pi/3$	$4\pi/3$	2	3	3×3
$\pi/4$	$\pi/2$	1	4	4×4
$3\pi/4$	$3\pi/2$	3	4	4×4
$\pi/5$	$2\pi/5$	2	5	5×5

It seems the number of sublattices can thus be taken equal to q. This means we can rewrite

$$H = \sum_{\boldsymbol{k}} \begin{pmatrix} S^\dagger_{1,\boldsymbol{k}} & S^\dagger_{2,\boldsymbol{k}} & \ldots & S^\dagger_{q,\boldsymbol{k}} \end{pmatrix} \mathcal{H}_{\boldsymbol{k}} \begin{pmatrix} S_{1,\boldsymbol{k}} \\ S_{2,\boldsymbol{k}} \\ \vdots \\ S_{q,\boldsymbol{k}} \end{pmatrix}, \tag{59}$$

where $\mathcal{H}$ is now a $q \times q$-matrix.

Using the same alignment of sublattices as in Figure 25a, a particle can hop from species S_m to itself using the vectors $\pm\boldsymbol{\delta}_2$. Then it can hop to S_{m-1} with $-\boldsymbol{\delta}_1$ and $+\boldsymbol{\delta}_3$, and to S_{m+} with $+\boldsymbol{\delta}_1$ and $-\boldsymbol{\delta}_3$. Taking into account the phase factors for the vectors $\pm\boldsymbol{\delta}_{2,3}$ we compute the generalized Bloch Hamiltonian for an arbitrary value of q to be:

$$\mathcal{H}_{\boldsymbol{k}} = -\frac{J}{2}\begin{pmatrix} D_1 & A_1 & 0 & 0 & \dots & A_q^* \\ A_1^* & D_2 & A_2 & 0 & \dots & 0 \\ 0 & A_2^* & D_3 & A_3 & \dots & 0 \\ & & \vdots & & \ddots & \\ A_q & 0 & 0 & 0 & \dots & D_q \end{pmatrix}, \tag{60}$$

where $D_i = 2\cos\left(\boldsymbol{k}\cdot\boldsymbol{\delta}_2 + 2\pi p/q(i-1)\right)$ are the diagonal elements and $A_i = e^{-i\boldsymbol{k}\cdot\boldsymbol{\delta}_1} + e^{i(\boldsymbol{k}\cdot\boldsymbol{\delta}_3 + \pi p/q(2i-1))}$ make up the off-diagonal elements. Due to periodicity of the lattice A_q and A_q^* appear in the bottom left and upper right corner.

Like for the square lattice, we can plot the relation between magnetic field and energy eigenvalues resulting in the Hofstadter butterfly for the triangular lattice (Figure 32). This fractal pattern is symmetric in the point $\varepsilon = 0,\ 2\pi p/q = \pi/2$. So inverting the direction of the magnetic field causes an inversion of the spectrum, $\varepsilon_\Phi = -\varepsilon_{2\pi-\Phi}$, contrary to the square lattice.
The energy bands are always distinct: there are no Dirac points. We will see that this means that the Chern number characterizing the topological properties are well-defined.

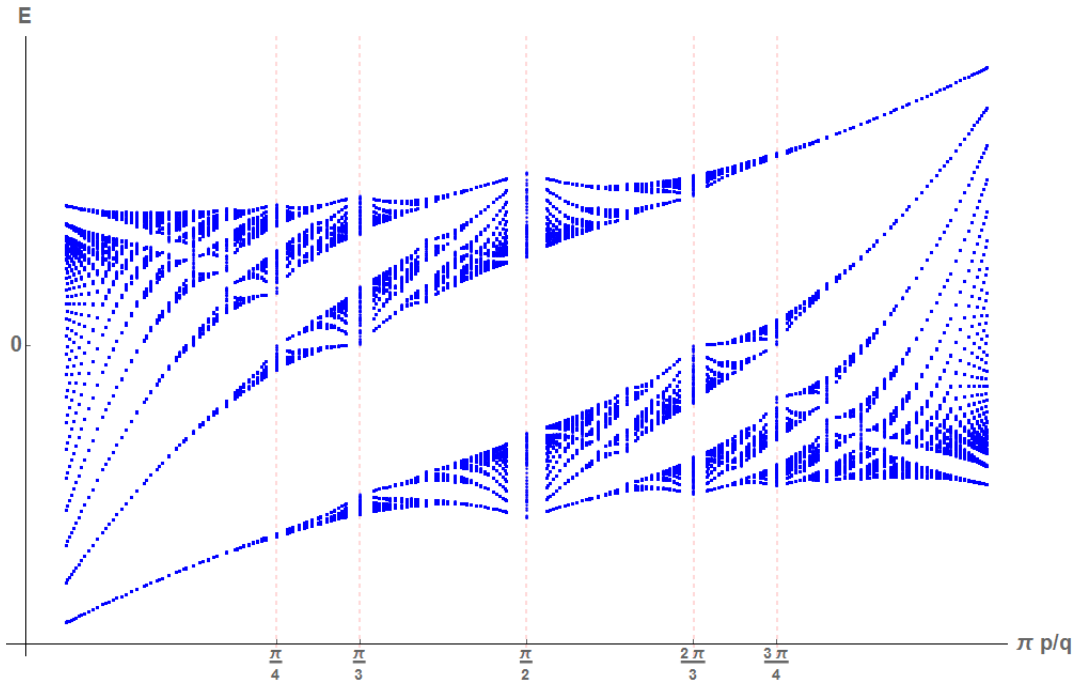

Figure 32: The Hofstadter butterfly for the triangular lattice. We computed the energies for each fractional value of $\dfrac{p}{q},\ p = 1,\dots,q-1;\ q = 1,\dots,10$ on a grid in $\boldsymbol{k}$-space whose squares have sides of length $\dfrac{2\pi}{25}$.

3 Generation of gauge fields using lattice shaking

In the previous chapter we have shown that for specific values of the magnetic flux the Kagome and dice lattice indeed have flat bands at low energies. Next, we want to use optical lattices to simulate these systems. In optical lattices the particles that hop around are neutral atoms, which are not susceptible to a magnetic field: they do not attain an Aharonov-Bohm phase when moving around a plaquette.

In this chapter we introduce a method that generates a gauge field through the lattice, equivalent to the application of a perpendicular magnetic field. We show that by shaking the lattice in the plane one obtains a complex hopping strength, which - as before - can be used to construct a net flux through a plaquette. This lattice shaking is equivalent to adding a time-periodic on-site modulation term to the Hamiltonian, which thus becomes dependent on time. We then use the Floquet formalism for time-periodic Hamiltonians to show that all physics is determined by the time-average of the system up to second order. Finally we demonstrate that for purely sinusoidal shaking we can tune the effective hopping strength. By adding a tilt and a phase shift on top of that, we can generate the phase factors in the hopping which are equivalent to the presence of a gauge field.

3.1 Time-periodic modulation

In optical lattices the atoms are located in the wells of the potential. Shaking the lattice configuration periodicaly in the plane is equivalent to moving each lattice site up and down, because this shifts the lattice potential in real space. An atom located at a site $\boldsymbol{x}$ will then be moving up and down along the edges of the potential well.
The frequency ω of the lattice shaking needs to be large, such that the period of the shaking $T = 2\pi/\omega$ is short compared to the timescale of the hopping: $\hbar\omega \gg J$. If this is not the case the atoms will move along with the minima of the potential wells adiabatically. At the same time, the frequency can not be too large: the atoms can be exited to a higher energy state which makes the tight-binding approximation invalid. Therefore the energy associated with the shaking needs to be much smaller than the depth of the potential well: $\hbar\omega \ll V_0$.

When these two conditions are satisfied, shaking the lattice is equivalent to adding a time-dependent kinetic term to the Hamiltonian that is periodic and site-dependent:

$$H(t) = -J \sum_{\boldsymbol{x},\ell} \left\{ a^\dagger_{\boldsymbol{x}+\boldsymbol{\delta}_\ell} a_{\boldsymbol{x}} + \text{H.c.} \right\} - \sum_{\boldsymbol{x}} \mu_{\boldsymbol{x}}(t) \hat{n}_{\boldsymbol{x}}. \tag{61}$$

The operator in the additional term is the number operator $\hat{n}_{\boldsymbol{x}} = a^\dagger_{\boldsymbol{x}} a_{\boldsymbol{x}}$. Because the time-dependent chemical potential is periodic, $\mu_{\boldsymbol{x}}(t+T) = \mu_{\boldsymbol{x}}(t)$, the Hamiltonian is as well: $H(t+T) = H(t)$. This means we can describe our system in the *Floquet state formalism* [16]. The Floquet state formalism follows from Floquet's theorem for time-periodic systems, which is analogous to the way Bloch states follow from Bloch's theorem for spatially periodic systems.
The Floquet states are the solutions to the time-dependent Schrödinger equation,

$$i\hbar|\psi_n(t)\rangle = H|\psi_n(t)\rangle, \tag{62}$$

of the form:

$$|\psi_n(t)\rangle = |u_n(t)\rangle e^{-i\varepsilon_n t/\hbar}. \tag{63}$$

Here $|u_n(t+T)\rangle = |u_n(t)\rangle$ are the Floquet modes that contain the time periodicity, and ε_n is the quantum number which now corresponds to the energy.

Due to the time-periodicity of the Hamiltonian, the energy of the system is quasi-conserved: the spectrum repeats for every multiple addition of $\hbar\omega$. Therefore, ε_n is a well-defined quantum number that we shall call the quasi-energy. Note the resemblance with the quantum number $\mathbf{k}$ for Bloch waves within the Brillioun zone, that we can shift by $\boldsymbol{k} + \boldsymbol{k}_i = \boldsymbol{k}$.

As we are interested in the evolution of the system on timescales much larger than T, we can compute the effective Hamiltonian in which we average the result of every period T. We will explicitly derive this result using the Floquet-Magnus expansion in Section 3.2. First we show that the time-dependence of the Hamiltonian is equivalent to multiplying with a time-dependent phase factor by applying a gauge transformation.

3.1.1 Gauge transformation of the time-dependent Hamiltonian

One can multiply any time-dependent wavefunction $|\psi(t)\rangle$ with a phase factor without changing the physics of the system, because a phase factor is a unitary operator for which $U^\dagger = U^{-1}$ (gauge transformation). We can show this by deriving what happens when we transform $|\psi(t)\rangle \to |\psi'(t)\rangle = e^{i\theta t}|\psi(t)\rangle$ where θ is a constant. The transformation of the Hamiltonian defined such that the Schrödinger equation is maintained:

$$\begin{aligned} i\partial_t|\psi'(t)\rangle &= H|\psi'(t)\rangle \\ i\partial_t\left(e^{i\theta t}|\psi(t)\rangle\right) &= H\left(e^{i\theta t}|\psi(t)\rangle\right) \\ e^{i\theta t}\left(-\theta + i\partial_t\right)|\psi(t)\rangle &= e^{i\theta t}H|\psi(t)\rangle \\ i\partial_t|\psi(t)\rangle &= \underbrace{\left(H+\theta\right)}_{=\tilde{H}}|\psi(t)\rangle \end{aligned}$$

Therefore transforming the wavefunction with a constant phase factor is equivalent to shifting the Hamiltonian with a constant amount. Indeed, a shift in energy does not change the physics of the system.

Instead of θ being constant, we can also derive what happens when $\theta \to \theta(t)$ is time-dependent:

$$\begin{aligned} i\partial_t\left(e^{i\theta(t)}|\psi(t)\rangle\right) &= H\left(e^{i\theta(t)}|\psi(t)\rangle\right) \\ &\downarrow \\ i\partial_t|\psi(t)\rangle &= \left(H+\theta'(t)\right)\psi(t) \\ &= \widetilde{H}(t)|\psi(t)\rangle \end{aligned}$$

Adding a time-dependent term to the Hamiltonian is thus equivalent to a gauge transformation of the wavefunctions.

We will use this result to rewrite the Hamiltonian given in Equation 61. For this we switch to the second quantization formalism, in which the phase factor becomes $e^{i\theta_{\boldsymbol{x}}(t)\hat{n}_{\boldsymbol{x}}}$. We can rewrite the Hamiltonian (61) as the time-independent part multiplied by a time-dependent phase factor by putting

$$\theta'_{\boldsymbol{x}}(t) = -\mu_{\boldsymbol{x}}(t). \tag{64}$$

The time-independent part is just the tight-binding Hamiltonian for nearest neighbour hopping. The properties of the derivative ensure that the phase has the same periodicity as the chemical potential: $\theta_{\boldsymbol{x}}(t+T) = \theta_{\boldsymbol{x}}(t)$.

In general, when transforming a wavefunction $\psi \to U\psi$, the operators transform as $O \to UOU^\dagger$. Therefore the ladder operators in our system transform as

$$a^\dagger_{\boldsymbol{x}} \longrightarrow e^{i\theta_{\boldsymbol{x}}(t)\hat{n}_{\boldsymbol{x}}}a^\dagger_i e^{-i\theta_{\boldsymbol{x}}(t)\hat{n}_{\boldsymbol{x}}}, \tag{65}$$

$$a_{\boldsymbol{x}} \longrightarrow e^{i\theta_{\boldsymbol{x}}(t)\hat{n}_{\boldsymbol{x}}}a_{\boldsymbol{x}} e^{-i\theta_{\boldsymbol{x}}(t)\hat{n}_{\boldsymbol{x}}}. \tag{66}$$

Applying these transformations changes the form of the Hamiltonian. In Appendix C.1 we derive that the number operator is invariant under this transformation, and that the hopping operator transforms as:

$$a^\dagger_{\boldsymbol{x}+\boldsymbol{\delta}_\ell} a_{\boldsymbol{x}+\boldsymbol{\delta}_\ell} \longrightarrow \exp\left[i\left(\theta_{\boldsymbol{x}+\boldsymbol{\delta}_\ell}(t) - \theta_{\boldsymbol{x}}(t)\right)\right] a^\dagger_{\boldsymbol{x}+\boldsymbol{\delta}_\ell} a_{\boldsymbol{x}+\boldsymbol{\delta}_\ell}. \tag{67}$$

Using the result from Equation (67) we can rewrite our Hamiltonian (61) as

$$H(t) = -\sum_{\boldsymbol{x}} J e^{i\left(\theta_{\boldsymbol{x}+\boldsymbol{\delta}_\ell}(t) - \theta_{\boldsymbol{x}}(t)\right)} \left\{ a^\dagger_{\boldsymbol{x}+\boldsymbol{\delta}_\ell} a_{\boldsymbol{x}} + \text{H.c.} \right\}. \tag{68}$$

It seems that the hopping strength is now already complex. But this phase factor will not generate a net flux through a plaquette, because the contributions will always cancel out. For example consider the square lattice and its lattice unit vectors $\boldsymbol{\delta}_1 = (1,0)$, $\boldsymbol{\delta}_2 = (0,1)$. When moving around a plaquette $\boldsymbol{\delta}_1 \to \boldsymbol{\delta}_2 \to -\boldsymbol{\delta}_1 \to -\boldsymbol{\delta}_2$ the sum of the phases becomes:

$$\begin{aligned}[\theta_{\boldsymbol{x}+\boldsymbol{\delta}_1}(t) - \theta_{\boldsymbol{x}}(t)] + [\theta_{\boldsymbol{x}+\boldsymbol{\delta}_1+\boldsymbol{\delta}_2}(t) - \theta_{\boldsymbol{x}+\boldsymbol{\delta}_1}(t)] \\ + [\theta_{\boldsymbol{x}+\boldsymbol{\delta}_2}(t) - \theta_{\boldsymbol{x}+\boldsymbol{\delta}_1+\boldsymbol{\delta}_2}(t)] + [\theta_{\boldsymbol{x}}(t) - \theta_{\boldsymbol{x}+\boldsymbol{\delta}_2}(t)] = 0.\end{aligned} \tag{69}$$

For other lattice structures we get the same result. This is just a consequence of the invariance of the flux under gauge transformations. In the next section we will see that when we compute the time-average of the system, the hopping strength *can* be altered by this gauge transformation.

3.2 Effective Hamiltonian

Our first step towards generating gauge fields is realizing that the effective physics is determined by the time-average of the system up to second order. For this we rewrite the Hamiltonian (61) for two-dimensional lattices in the following way:

$$H(t) = -\sum_{\boldsymbol{x},\ell} J e^{i\vartheta_{\boldsymbol{\delta}_\ell}(t)} \left\{ a^\dagger_{\boldsymbol{x}+\boldsymbol{\delta}_\ell} a_{\boldsymbol{x}} + \text{ H.c.} \right\}. \tag{70}$$

Here $\vartheta_{\boldsymbol{\delta}_\ell}(t) = \theta_{\boldsymbol{x}+\boldsymbol{\delta}_\ell}(t) - \theta_{\boldsymbol{x}}(t)$ is the phase factor obtained when hopping from site $\boldsymbol{x}$ to $\boldsymbol{x}+\boldsymbol{\delta}_\ell$. We demand that its time average equals zero:

$$\langle \vartheta_{\boldsymbol{\delta}_\ell} \rangle_T = \frac{1}{T} \int_0^T dt\ \vartheta_{\boldsymbol{\delta}_\ell}(t) = 0. \tag{71}$$

If this is not the case, the Floquet analysis is not valid: after each cycle T a certain amount of energy is added to Hamiltonian, violating the condition tat $H(t+T) = H(t)$.

Because the periodicity of $\theta_{\boldsymbol{x}}(t)$ is small, we expect the physics on longer time scales to be effectively determined by the average of its behaviour. Therefore to describe the system we introduce an effective Hamiltonian which is the time-average of the time-dependent Hamiltonian:

$$\begin{aligned}H_{\text{eff}} &= \frac{1}{T} \int_0^T dt H(t) \\ &= -\frac{1}{T} \sum_{\boldsymbol{x},\ell} J \left(\int_0^T dt\ e^{i\vartheta_{\boldsymbol{\delta}_\ell}(t)} \right) \left\{ a^\dagger_{\boldsymbol{x}+\boldsymbol{\delta}_\ell} a_{\boldsymbol{x}} + \text{H.c.} \right\}.\end{aligned}$$

The integration of the time-dependent phase factor depends on the expression for $\vartheta_{\boldsymbol{\delta}_\ell}(t)$.

3.2.1 High-frequency approximation

Using the Floquet-Magnus expansion in powers of ω^{-1} [16], we can show that the effective Hamiltonian H_{eff} is *exact* up to second order.
First we compare the evolution operators for the time-dependent Hamiltonian $H(t)$ and H_{eff}. Recall that the evolution operator $U(t)$ for a time-dependent Hamiltonian is defined as

$$U(t) = \mathcal{T} \exp\left[-i \int_0^t H(t')dt'\right]. \tag{72}$$

Here $\mathcal{T}$ is the time-ordering operator, defined as

$$\mathcal{T}\left[A(t)B(t')\right] = \begin{cases} A(t)B(t') & \text{if } t < t', \\ \pm B(t')A(t) & \text{if } t > t'. \end{cases}$$

The $+(-)$-sign depends on the bosonic (fermionic) nature of the operators.
We can expand this time-ordered exponential integral in powers of T using the time-ordered products $P_n(t) = (-i)^n \int_0^t dt_1 \ldots \int_0^{t_{n-1}} dt_n \; H(t_1) \ldots H(t_n)$ as was done by Dyson originally (see [17]):

$$U(t) = \mathbb{1} + \sum_{n=1}^{\infty} P_n(t). \tag{73}$$

We can consider the evolution operator after a period T up to second order in $T \sim \omega^{-1}$:

$$U(T) = \mathbb{1} - i \int_0^T dt_1 \; H(t_1) - \int_0^T dt_1 \int_0^{t_1} dt_2 \; H(t_1)H(t_2) + \mathcal{O}(T^3). \tag{74}$$

To justify using H_{eff} to compute the physics of our time-periodically driven system, we want to show this equals - the evolution operator corresponding to the effective Hamiltonian:

$$\tilde{U}(T) = \exp\left[-iH_{\text{eff}}T\right] \stackrel{!}{=} U(T). \tag{75}$$

For this we expand $H_{\text{eff}}T = \sum_{n=1}^{\infty} H_{\text{eff}}^{(n)} T^n$ in powers of T, such that

$$\tilde{U}(T) = \mathbb{1} - iH_{\text{eff}}^{(1)}T - iH_{\text{eff}}^{(2)}T^2 - \frac{1}{2}\left(H_{\text{eff}}^{(1)}\right)^2 T^2 + \mathcal{O}(T^3). \tag{76}$$

For zeroth and first order we see

$$\begin{aligned} 0^{\text{th}} \text{ order}: \quad & \mathbb{1} = \mathbb{1} \\ 1^{\text{st}} \text{ order}: \quad & -i \int_0^T dt_1 \; H(t_1) = -iH_{\text{eff}}^{(1)}T \\ & H_{\text{eff}}^{(1)} = \frac{1}{T} \int_0^T dt_1 \; H(t_1) \end{aligned}$$

Therefore it is true that the effective Hamiltonian equals the time averaged Hamiltonian up to first order. Now comparing the second order terms:

$$\begin{aligned} 2^{\text{nd}} \text{ order}: \quad & -\int_0^T dt_1 \int_0^{t_1} dt_2 \; H(t_1)H(t_2) = -iH_{\text{eff}}^{(2)}T^2 - \frac{1}{2}\left(H_{\text{eff}}^{(1)}\right)^2 T^2 \\ & H_{\text{eff}}^{(2)} = \frac{i}{2}\left(H_{\text{eff}}^{(1)}\right)^2 - \frac{i}{T^2} \int_0^T dt_1 \int_0^{t_1} dt_2 \; H(t_1)H(t_2) \end{aligned}$$

We can use the result from first order that $H_{\text{eff}}^{(1)} = \frac{1}{T}\int_0^T dt_1 \; H(t_1)$.

To solve for the second coefficient $H_{\text{eff}}^{(2)}$ we assume that our time-dependent Hamiltonian has the gauge-transformed form of a phase factor multiplied with a time-independent part as in Equation (70):

$$H(t) = \sum_{\boldsymbol{x},\ell} e^{i\vartheta_{\boldsymbol{\delta}_\ell}(t)} \hat{h}_{\boldsymbol{x},\boldsymbol{\delta}_\ell}, \qquad \hat{h}_{\boldsymbol{x},\boldsymbol{\delta}_\ell} = -J\left\{a^\dagger_{\boldsymbol{x}+\boldsymbol{\delta}_\ell} a_{\boldsymbol{x}} + \text{H.c.}\right\}. \tag{77}$$

Remember that $\vartheta_{\boldsymbol{\delta}_\ell}(t+T) = \vartheta_{\boldsymbol{\delta}_\ell}(t)$, implying that $\vartheta_{\boldsymbol{\delta}_\ell}(T) = \vartheta_{\boldsymbol{\delta}_\ell}(0)$. We see that now

$$H_{\text{eff}}^{(2)} = \frac{i}{T^2} \sum_{\substack{\boldsymbol{x},\ell \\ \boldsymbol{x}',\ell'}} \left[\frac{1}{2} \left(\int_0^T dt_1 \; e^{i\vartheta_{\boldsymbol{\delta}_\ell}(t_1)} \right) \left(\int_0^T dt_1 \; e^{i\vartheta_{\boldsymbol{\delta}'_\ell}(t_1)} \right) \right.$$
$$\left. - \int_0^T dt_1 \left(e^{i\vartheta_{\boldsymbol{\delta}_\ell}(t_1)} \int_0^{t_1} dt_2 \; e^{i\vartheta_{\boldsymbol{\delta}_{\ell'}}(t_2)} \right) \right] \hat{h}_{\boldsymbol{x},\boldsymbol{\delta}_\ell} \hat{h}_{\boldsymbol{x}',\boldsymbol{\delta}_{\ell'}}. \tag{78}$$

Using the periodicity of powers of $\vartheta_{\boldsymbol{\delta}_\ell}(t)$, it turns out that

$$H_{\text{eff}}^{(2)} = 0. \tag{79}$$

Therefore the effective Hamiltonian is an exact description of the system up to second order in ω^{-1}. A detailed calculation of the result above can be found in Appendix C.2.

3.3 Generation of flux

With the effective Hamiltonian we can generate complex hopping strength that are constant in time. For this we choose a specific form of $\theta_{\boldsymbol{x}}$. Here we consider sinusoidal modulations of the Hamiltonian, which will turn out to have analytic solutions. After this we combine a resonant tilt with site-dependent phase shifts to generate complex phase factors. First we show below that a sinusodal modulation effectively results in the hopping strength becoming proportional to the zero-th order Bessel function.

3.3.1 Sinusoidal modulation

We consider a shaking where the chemical potential depends on ω in a sinusoidal manner:

$$\mu_{\boldsymbol{x}}(t) = A_{\boldsymbol{x}} \cos \omega t. \tag{80}$$

The phase is then defined according to Equation (64):

$$\theta_{\boldsymbol{x}}(t) = \frac{A_{\boldsymbol{x}}}{\omega} \sin \omega t. \tag{81}$$

When a particle hops, the phase factor depends on the difference in phase of the two sites:

$$\vartheta_{\boldsymbol{\delta}_\ell}(t) = \underbrace{\frac{A_{\boldsymbol{x}+\boldsymbol{\delta}_\ell} - A_{\boldsymbol{x}}}{\omega}}_{=\mathcal{A}_{\boldsymbol{\delta}_\ell}/\omega} \sin \omega t$$

The amplitude of the shaking varies for different hopping directions. This depends on the type of lattice shaking and the structure of the lattice.
To obtain the effective Hamiltonian we have to compute the following expression:

$$\int_0^T dt \; e^{i\vartheta_{\boldsymbol{\delta}_\ell}(t)} = \int_0^T dt \; e^{i\mathcal{A}_{\boldsymbol{\delta}_\ell}\omega^{-1}\sin\omega t}. \tag{82}$$

To do so we first rewrite the exponential in terms of Bessel functions $\mathcal{J}_m$ using the Jacobi-Anger expansion:

$$e^{iz\sin\varphi} = \sum_{m=-\infty}^{\infty} \mathcal{J}_m(z) e^{im\varphi}. \tag{83}$$

Applying this to Equation (82) we see

$$\begin{aligned}\frac{1}{T}\int_0^T dt\; e^{i\mathcal{A}_{\boldsymbol{\delta}_\ell}\omega^{-1}\sin\omega t} &= \frac{1}{T}\int_0^T dt \sum_m \mathcal{J}_m\left(\frac{\mathcal{A}_{\boldsymbol{\delta}_\ell}}{\omega}\right) e^{im\omega t} \\ &= \frac{\omega}{2\pi}\sum_m \mathcal{J}_m\left(\frac{\mathcal{A}_{\boldsymbol{\delta}_\ell}}{\omega}\right)\cdot\frac{2\pi}{\omega}\delta_{m,0} \\ &= \mathcal{J}_0\left(\frac{\mathcal{A}_{\boldsymbol{\delta}_\ell}}{\omega}\right).\end{aligned}$$

The effective Hamiltonian follows to be

$$H_{\text{eff}} = -\sum_{\boldsymbol{x}} J\mathcal{J}_0\left(\frac{\mathcal{A}_{\boldsymbol{\delta}_\ell}}{\omega}\right)\left\{a^\dagger_{\boldsymbol{x}+\boldsymbol{\delta}_\ell}a_{\boldsymbol{x}} + \text{H.c.}\right\}. \tag{84}$$

In Figure 33 we have plotted $\mathcal{J}_0\left(\frac{\mathcal{A}_{\boldsymbol{\delta}_\ell}}{\omega}\right)$ as a function of the difference in amplitude.

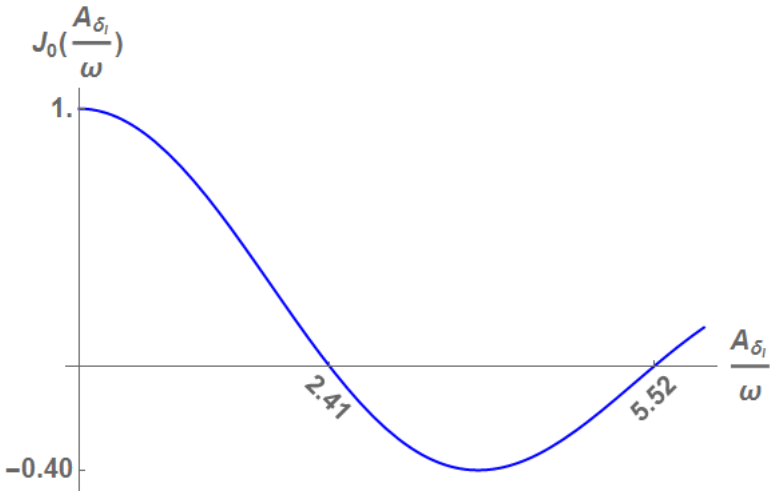

Figure 33: The Bessel function $\mathcal{J}_0(A)$ for $0 \leq A \leq 6$. The values of A for which the function equals zero are indicated.

We can therefore tune the strength of the hopping from positive to zero to negative by varying the strength of the shaking amplitude in direction of $\boldsymbol{\delta}_\ell$.

3.3.2 Resonant driving

We now turn to resonant driving, for which we put certain lattice sites on a different potential height. To do so we add a tilt proportional to the number operator to the Hamiltonian:

$$H(t) = -\sum_{\boldsymbol{x},\ell} J\left(a^\dagger_{\boldsymbol{x}+\boldsymbol{\delta}_\ell}a_{\boldsymbol{x}} + \text{H.c.}\right) + \sum_{\boldsymbol{x}}\left(A_{\boldsymbol{x}}\cos\omega t + \Delta_{\boldsymbol{x}}\right)\hat{n}_{\boldsymbol{x}}. \tag{85}$$

The phase defining the gauge transformation becomes:

$$\vartheta_{\boldsymbol{\delta}_\ell}(t) = \frac{\mathcal{A}_{\boldsymbol{\delta}_\ell}}{\omega}\sin\omega t + \mathcal{D}_{\boldsymbol{\delta}_\ell}t, \tag{86}$$

where $\mathcal{D}_{\boldsymbol{\delta}_\ell} = \Delta_{\boldsymbol{x}+\boldsymbol{\delta}_\ell} - \Delta_{\boldsymbol{x}}$ is the tilt between two neighbouring sites. To find the effective Hamiltonian we average this over one period:

$$\frac{1}{T}\int_0^T dt\; e^{i\mathcal{A}_{\boldsymbol{\delta}_\ell}\omega^{-1}\sin\omega t}e^{i\mathcal{D}_{\boldsymbol{\delta}_\ell}t} = \frac{1}{T}\int_0^T dt\sum_m \mathcal{J}_m\left(\frac{\mathcal{A}_{\boldsymbol{\delta}_\ell}}{\omega}\right)e^{i(m\omega+\mathcal{D}_{\boldsymbol{\delta}_\ell})t} \tag{87}$$

This integral is solvable when $\mathcal{D}_{\boldsymbol{\delta}_\ell} = -\nu_{\boldsymbol{\delta}_\ell}\omega,\ \nu_{\boldsymbol{\delta}_\ell} \in \mathbb{Z}$ is *resonant* with the driving frequency. We can again solve using a Kronecker delta function:

$$\begin{aligned}\frac{1}{T}\int_0^T dt \sum_m \mathcal{J}_m\left(\frac{\mathcal{A}_{\boldsymbol{\delta}_\ell}}{\omega}\right) e^{i(m-\nu_{\boldsymbol{\delta}_\ell})\omega t} &= \sum_m \mathcal{J}_m\left(\frac{\mathcal{A}_{\boldsymbol{\delta}_\ell}}{\omega}\right)\delta_{m,\nu_{\boldsymbol{\delta}\ell}} \\ &= \mathcal{J}_{\nu_{\boldsymbol{\delta}_\ell}}\left(\frac{\mathcal{A}_{\boldsymbol{\delta}_\ell}}{\omega}\right).\end{aligned}$$

The expression for the effective Hamiltonian becomes

$$H_{\text{eff}} = -\sum_{\boldsymbol{x}} J\mathcal{J}_{\nu_{\boldsymbol{\delta}_\ell}}\left(\frac{\mathcal{A}_{\boldsymbol{\delta}_\ell}}{\omega}\right)\left\{a^\dagger_{\boldsymbol{x}+\boldsymbol{\delta}_\ell}a_{\boldsymbol{x}} + \text{H.c.}\right\}. \tag{88}$$

Now this result is not necessary of more value than the one from the previous paragraph. But when we combine this resonant tilt with a phase shift, the hopping strength becomes complex:

$$H(t) = -\sum_{\boldsymbol{x},\ell} J\left(a^\dagger_{\boldsymbol{x}+\boldsymbol{\delta}_\ell}a_{\boldsymbol{x}} + \text{H.c.}\right) + \sum_{\boldsymbol{x}}\left(A_{\boldsymbol{x}}\cos\left(\omega t + \phi_{\boldsymbol{x}}\right) + \Delta_{\boldsymbol{x}}\right)\hat{n}_{\boldsymbol{x}}. \tag{89}$$

For $A_{\boldsymbol{x}} = A,\ \forall \boldsymbol{x}$ the phase defining the gauge transformation becomes:

$$\begin{aligned}\vartheta_{\boldsymbol{\delta}_\ell} &= \frac{A}{\omega}\left(\sin\left(\omega t + \phi_{\boldsymbol{x}+\boldsymbol{\delta}_\ell}\right) - \sin\left(\omega t + \phi_{\boldsymbol{x}}\right)\right) - \nu_{\boldsymbol{\delta}_\ell}\omega t \\ &= \frac{2A}{\omega}\sin\left(\varphi_{\boldsymbol{\delta}_\ell}\right)\sin\left(\omega t + \Phi_{\boldsymbol{\delta}_\ell}\right) - \nu_{\boldsymbol{\delta}_\ell}\omega t.\end{aligned}$$

The difference in phase shifts of neighbouring sites is denoted by $\varphi_{\boldsymbol{\delta}_\ell} = (\phi_{\boldsymbol{x}+\boldsymbol{\delta}_\ell} - \phi_{\boldsymbol{x}})/2$ and the sum by $\Phi_{\boldsymbol{\delta}\ell} = (\phi_{\boldsymbol{x}+\boldsymbol{\delta}_\ell} + \phi_{\boldsymbol{x}})/2$. The sine function containing $\varphi_{\boldsymbol{\delta}_\ell}$ is independent of time. In the other sine function $\Phi_{\boldsymbol{\delta}_\ell}$ is just a shift of ωt. To perform the time average we substitute $t \to t - \Phi_{\boldsymbol{\delta}_\ell}/\omega$:

$$\begin{aligned}\frac{1}{T}\int_0^T dt\ e^{iA\omega^{-1}\sin(\phi_{\boldsymbol{\delta}_\ell})\sin\left(\omega t + \Phi_{\boldsymbol{\delta}_\ell}\right)}e^{-i\nu_{\boldsymbol{\delta}_\ell}\omega t} &= \frac{1}{T}\int_0^T dt\ e^{iA\omega^{-1}\sin(\phi_{\boldsymbol{\delta}_\ell})\sin\omega t}e^{-i\nu_{\boldsymbol{\delta}_\ell}\left(\omega t - \Phi_{\boldsymbol{\delta}_\ell}\right)} \\ &= e^{i\nu_{\boldsymbol{\delta}_\ell}\Phi_{\boldsymbol{\delta}_\ell}}\mathcal{J}_{\nu_{\boldsymbol{\delta}_\ell}}\left(\frac{A}{\omega}\sin(\varphi_{\boldsymbol{\delta}_\ell})\right).\end{aligned}$$

Renaming $\tilde{\mathcal{A}}_{\boldsymbol{\delta}_\ell} = A/\omega\sin(\varphi_{\boldsymbol{\delta}_\ell})$ finally the effective Hamiltonian becomes

$$H_{\text{eff}} = -\sum_{\boldsymbol{x}} J\mathcal{J}_{\nu_{\boldsymbol{\delta}_\ell}}(\tilde{\mathcal{A}}_{\boldsymbol{\delta}_\ell})e^{i\nu_{\boldsymbol{\delta}_\ell}\Phi_{\boldsymbol{\delta}_\ell}}\left\{a^\dagger_{\boldsymbol{x}+\boldsymbol{\delta}_\ell}a_{\boldsymbol{x}} + \text{H.c.}\right\}. \tag{90}$$

Effectively the hopping coefficient now equals $J_{\text{eff}} = J\mathcal{J}_{\nu_{\boldsymbol{\delta}_\ell}}(\tilde{\mathcal{A}}_{\boldsymbol{\delta}_\ell})e^{i\nu_{\boldsymbol{\delta}_\ell}\Phi_{\boldsymbol{\delta}_\ell}}$ which is a complex number. By choosing the phase shifts of neighbouring sites $\phi_{\boldsymbol{x}}$ and $\phi_{\boldsymbol{x}+\boldsymbol{\delta}_\ell}$ wisely we can construct a nontrivial phase factor. Observe that putting $\phi_{\boldsymbol{x}} = \phi_{\boldsymbol{x}+\boldsymbol{\delta}_\ell}$ might pose problems, as this results in $\tilde{\mathcal{A}}_{\boldsymbol{\delta}_\ell} = 0$. For $\nu_{\boldsymbol{\delta}_\ell} \neq 0$ the Bessel functions $\mathcal{J}_{\nu_{\boldsymbol{\delta}_\ell}}(0)$ will be zero, completely inhibiting the hopping between the two sites. Therefore constructing the site-dependent phase shift is not necessarily a straightforward process.

4 Experimental setup for probing flat bands

Up until now we have seen the energy spectra of several two-dimensional lattice structures, and how these are affected when applying a magnetic field. We have shown that some of these are topologically nontrivial and what kind of physical phenomena this implies. In practice, conducting an experiment which explicitly measures the topological properties of a system is difficult, because solid state systems in general do not allow for experimental control of parameters such as the hopping strength, nonuniformity of the magnetic field, deformations of the lattice structure etc. This is where the simulation of solid state systems proves to have a huge advantage as this allows us to tune the hopping strength and generate a gauge field such that we can generate energy spectra containing a flat band.

In this chapter, we start by introducing the mechanism behind optical lattices with cold atoms. Then we put forward the potential that generates the Kagome and dice lattice structures. Finally, we use the results from the previous chapter to generate a gauge flux through these lattices.

4.1 Optical lattices

After the realization of a Bose-Einstein condensate with ultracold atoms in 1995 [18], many experiments have been conducted to study quantum effects of many-body systems in optical setups. More recently these atoms have been put in a periodic structure (the *optical lattice*), where they simulate solid states physics. There are multiple advantages of using an optical lattice as opposed to real solids. First of all, because the atoms are cooled to extremely low temperatures of the order $\sim \mu K$ the quantummechanical processes are slow and therefore easier to observe. Moreover the system is free of disorder and lattice vibrations, which is extremely hard to achieve for actual solids. The mobility of the atoms can be tuned during the experiment by changing the intensity of the laser. The fact that optical lattices are environments in which many of the parameters can be controlled is what makes them suitable for investigating e.g. their topological properties. Different lattice structures can be tested in the same experimental setup.

The mechanism of trapping atoms in an optical lattice structure is based on the coupling between the atoms and laser photons. Lasers producing photons with an energy $\hbar\omega_0$ that is exactly equal to a transition between two atomic levels are resonant: the atoms will be excited. For optical lattices, we put the laser frequency at a *detuning* $\delta = \omega_0 - \omega_L$, where ω_L is the frequency of the laser. For large enough δ only second-order perturbation processes are relevant, characterized by the dipole force [5]:

$$\boldsymbol{F}_{\text{dip}}(\boldsymbol{x}) = \boldsymbol{\nabla} V(\boldsymbol{x}) \qquad \text{with} \quad V_{\text{dip}}(\boldsymbol{x}) = \frac{1}{2}\alpha(\omega_L)\left[|\boldsymbol{E}(\boldsymbol{x})|^2\right]. \tag{91}$$

The electric field $\boldsymbol{E}(\boldsymbol{x})$, provided here by the laser, induces a dipole moment in the (neutrally charged) atoms. The strength of the potential is characterized by the polarizability $\alpha(\omega_L) \propto \delta = \omega_0 - \omega_L$, where δ is the *detuning* and ω_0 and ω_L are the resonance and laser frequency respectively. For red-detuned light $\delta > 0$ the atoms can minimize their energy by being at the position of minimum amplitude (antinodes). Vice versa, for blue-detuned light $\delta < 0$ the atoms will move towards places of maximum amplitude (nodes). If we create a standing wave pattern we can thus control the positions of the atoms.

4.1.1 Optical potential

By overlapping two counterpropagating laser beams we can create a standing wave pattern:

$$V(x) = V_0 \cos^2(qx). \tag{92}$$

The depth of the potential V_0 depends on the intensity and detuning of the lasers. The lattice constant is inversely proportional to the wavevector of the standing wave: $a = \pi/q = \lambda/2$.

By adding another pair of counterpropagating beams in a direction orthogonal to this pair, we obtain a two-dimensional lattice. In the resulting potential the relative polarizations of the lasers determine the precise orientation of the lattice:

$$V(x,y) = V_0 \left[\cos^2(qx) + \cos^2(qy) + 2\left(\hat{\boldsymbol{\epsilon}}_x \cdot \hat{\boldsymbol{\epsilon}}_y\right)\cos(qx)\cos(qy)\right]. \tag{93}$$

This configuration generates the square lattice, as shown in Figure 34.

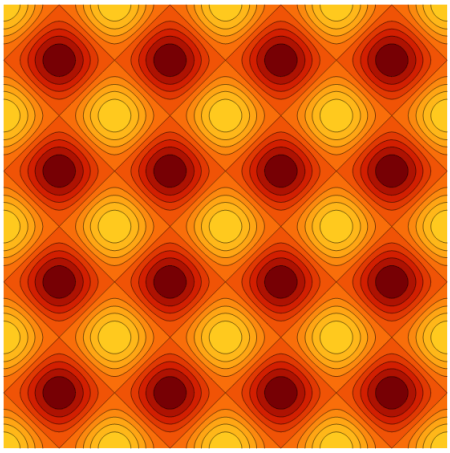

Figure 34: The standing wave pattern given by Equation (93) with $\hat{\boldsymbol{\epsilon}}_x \cdot \hat{\boldsymbol{\epsilon}}_y = 0$. The red sites correspond to $V(x,y) \to 0$ (nodes) whereas the yellow sites indicate maximum values of $V(x,y)$. Thus for this potential the atoms will arrange in the structure of a square lattice for both red and blue detuning of the lasers.

Square lattice We can rewrite the optical potential for the square lattice in terms of its reciprocal lattice vectors $\boldsymbol{\kappa}_x = 2\pi(1,0)$ and $\boldsymbol{\kappa}_y = 2\pi(0,1)$:

$$V_{\text{sq}}(x,y) = V_0 \sum_{i=x,y} \cos^2\left(\boldsymbol{\kappa}_i \cdot \boldsymbol{x}\right). \tag{94}$$

Triangular lattice As for the square lattice, we can use the reciprocal lattice vectors of the triangular lattice to obtain the optical potential. The three reciprocal lattice vectors are:

$$\boldsymbol{\kappa}_1 = 2\pi(1,0), \qquad \boldsymbol{\kappa}_2 = 2\pi\left(-\frac{1}{2}, -\frac{1}{2}\sqrt{3}\right) \qquad \text{and} \qquad \boldsymbol{\kappa}_3 = 2\pi\left(-\frac{1}{2}, \frac{1}{2}\sqrt{3}\right). \tag{95}$$

The potential for the triangular lattice then equals $V_{\text{tr}}(\boldsymbol{x}) = V_0 \sum_{i=1}^{3} \cos^2(\boldsymbol{\kappa}_i \cdot \boldsymbol{x})$ as shown in Figure 35.

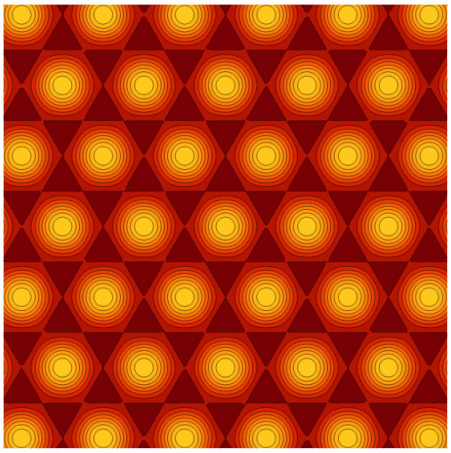

Figure 35: The standing wave pattern for the triangular lattice. The triangular structure is now generated by the yellow sites, which correspond to maximum values of the potential $V(\boldsymbol{x})$. So for red detuned lasers the atoms will arrange in a triangular pattern.

Experimentally this structure can be obtained by putting three counterpropagating beams in the plane, separated by an angle of 120°. This will cause a mixing of the beams as in Equation (93). Because we have three beams we can not choose the polarization orthogonal to one another, but it can be shown that when each beam has a polarization orthogonal to the plane the correct terms remain [19].

Kagome and dice lattice We can use the triangular lattice potential to generate the Kagome structure, by using a superlattice that 'removes' one out of every three sites of the triangular lattice [20]. Here we specifically follow the potential given by Burkov et al. [21]:

$$V_{\mathrm{Kg}}(\boldsymbol{x}) = \sum_{i=1}^{3} \left[\cos\left(\boldsymbol{k}_i \cdot \boldsymbol{x} + \boldsymbol{\rho}_i \frac{\pi}{2}\right) - 2\cos\left(\frac{\boldsymbol{k}_i}{3} \cdot \boldsymbol{x} + \boldsymbol{\rho}_i \frac{\pi}{2}\right) \right]^2 , \tag{96}$$

where $\boldsymbol{\rho} = (1, -1, 1)$. Note that in the second term we subtract a term with a period that is three times as large. This generates the potential shown in Figure 36a, corresponding to the Kagome structure for red-detuned light.

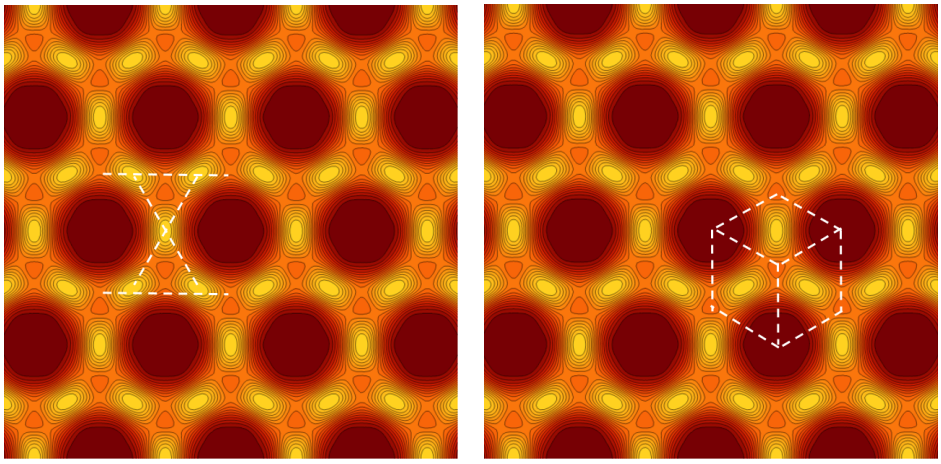

(a) The potential given in Equation (96). The Kagome structure is indicated by the dashed white lines, formed by the yellow maxima of the potential.

(b) The same potential, but now the dice structure is indicated; the red sites (absolute minima) are 6-fold coordinated while the orange sites (local minima) are 3-fold coordinated.

Figure 36

It turns out that this potential also generates a dice lattice-like structure for blue-detuned light, as shown in Figure 36b. The complication is that the 3-fold and 6-fold coordinated sites are at different potential heights. We can lift them to equal heights by adding the following two potential terms [21]:

$$V_{\mathrm{Dc},1}(\boldsymbol{x}) = \sum_{i=1}^{3} 4\cos^2\left(\boldsymbol{\kappa}_i \cdot \boldsymbol{x}\right), \tag{97}$$

$$V_{\mathrm{Dc},2}(\boldsymbol{x}) = -\sum_{i=1}^{3} 4\cos^2\left(\tilde{\boldsymbol{\kappa}}_i \cdot \boldsymbol{x}\right) \qquad \text{with } \tilde{\boldsymbol{\kappa}}_1 = 2\pi\left(\frac{1}{2\sqrt{3}}, \frac{1}{2}\right), \; \tilde{\boldsymbol{\kappa}}_2 = 2\pi\left(-\frac{1}{\sqrt{3}}, 0\right), \; \tilde{\boldsymbol{\kappa}}_3 = 2\pi\left(\frac{1}{2\sqrt{3}}, -\frac{1}{2}\right). \tag{98}$$

The sum of these potentials $V_{\mathrm{KD}}(\boldsymbol{x}) = V_{\mathrm{Kg}}(\boldsymbol{x}) + V_{\mathrm{Dc},1}(\boldsymbol{x}) + V_{\mathrm{Dc},2}(\boldsymbol{x})$ is shown in Figure 37.

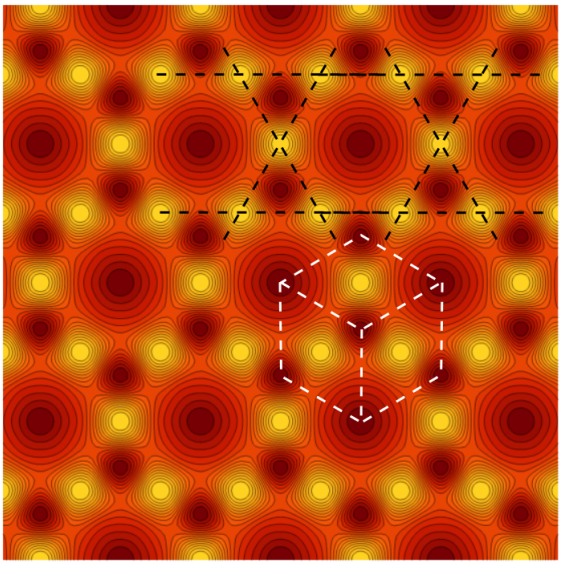

Figure 37: The potential $V_{KD}(\boldsymbol{x})$ which gives the Kagome structure for red-detuned light and the dice structure for blue-detuned light. The Kagome bonds are illustrated by the dashed black lines. The dice bonds are illustrated by the dashed white lines.

4.2 The hopping strength

In optical lattices the atoms are located in the (anti)nodes, which act as a potential well (see Figure 38). Quantummechanically the atoms will behave as wavepackets, for which the strength of localization is proportional to the depth of the potential well. The potential barrier between two neighbouring sites corresponds to the probability of the particle tunneling (i.e. hopping) from one site to the other.

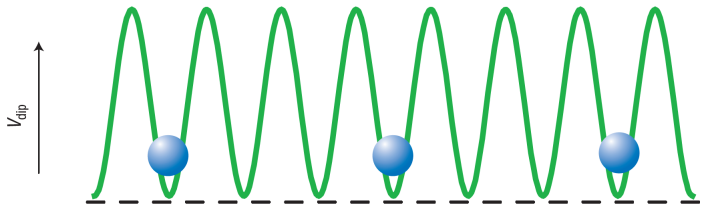

Figure 38: Atoms located in the minima of V_{dip}. They can hop to a neighbouring minimum by tunneling through a potential barrier. Figure taken from [22].

Consider a one-dimensional chain of lattice sites created by an optical potential $V(x) = V_0 \sin^2(qx)$ (Figure 38) where $q = 2\pi/\lambda$ is the wavevector determined by the wavelength of the laser λ. The Hamiltonian in first quantization equals that of a free particle confined in a harmonic potential:

$$\mathbf{H} = -\frac{1}{2m}\partial_x^2 + V_0 \sin^2(qx). \tag{99}$$

Using the tight-binding approximation (with nearest-neighbour hopping) the Hamiltonian in second quantization equals

$$H = -J \sum_i a_{x_i}^\dagger a_{x_{i+1}}. \tag{100}$$

The minima of the potential are denoted with x_j, $j, 1 \ldots, N$, where N is the total number of sites in the system. The hopping strength J in the tight-binding Hamiltonian thus becomes a tunneling strength, which we show below is characterized by the strength of the potental V_0 and the recoil energy $E_r = q^2/(2m)$ ($\hbar = 1$). The recoil energy indicates the momentum of the atom after emitting a photon.
The probability of this tunneling is linked to the height of the potential barrier in between the sites; for a higher potential barrier the wavefunctions of the particles will be more localized. Therefore their overlap (corresponding to their tunneling probability) will be smaller. The hopping parameter J has the dimension of energy. We can express the overlap between two neighbouring particles in terms of energy using

$$J = -\langle \psi(x - x_i) | \mathbf{H} | \psi(x - x_{i+1}) \rangle. \tag{101}$$

To compute the value of J we derive a more explicit form for the wavefunctions. For a system that is periodic in real space, the uniquely defined momenta k are contained in the first Brillouin zone $\{-\pi/a, \pi/a\}$. Here a is the lattice constant. We can apply the Bloch theorem and rewrite the wavefunctions as

$$\phi_k(x) = e^{ikx} u_k(x), \tag{102}$$

where k is in the first Brillouin zone and $u_k(x)$ is a function that has the same periodicity as the crystal: $u_k(x + 1) = u_k$. The Bloch functions are orthogonal.
When this system is in the groundstate, which we assume to be the case, the particles will be located at the minima of the potential. Therefore it will be localized in real space, and it is more useful to rewrite the Bloch function to a real-space representation. We do this with the Wannier function, defined as:

$$w(x - x_i) = \frac{1}{\sqrt{N}} \sum_k e^{-ikx_i} \phi_k(x). \tag{103}$$

This function gives us the amplitude at position x of a wavefunction centered at site x_i. It can indeed be shown that this depends only on the relative distance $x - x_i$, which we expect for a periodic system.

We use the result from Equation (103) and plug this into Equation (101):

$$\begin{aligned} J &= -\int dx\ w^*(x - x_i) \left[-\frac{1}{2m} \partial_x^2 + V_0 \sin^2(qx) \right] w(x - x_{i+1}) \\ &= -\frac{1}{N} \int dx \sum_{k,k'} \left\{ e^{ikx_i} \phi_k^*(x) \left[-\frac{1}{2m} \partial_x^2 + V_0 \sin^2(qx) \right] e^{-ik'x_{i+1}} \phi_{k'}(x) \right\} \\ &= -\frac{1}{N} \int dx \sum_{k,k'} \left\{ e^{i(kx_i - k'x_{i+1})} \phi_k^*(x) \left[-\frac{1}{2m} \frac{\partial^2 \phi_{k'}(x)}{\partial x^2} + V_0 \sin^2(qx) \phi_{k'}(x) \right] \right\}. \end{aligned} \tag{104}$$

For the next step we focus on the expression in the square brackets. Using the time-independent Schrödinger equation we know this equals:

$$\left[-\frac{1}{2m} \frac{\partial^2}{\partial x^2} + V_0 \sin^2(qx) \right] \phi_{k'}(x) = E_{k'} \phi_{k'}(x). \tag{105}$$

When we substitute $\chi = qx$ and plug in the expression for the recoil energy we see that

$$\begin{aligned} \left[-\underbrace{\frac{q^2}{2m}}_{E_r} \frac{\partial^2}{\partial \chi^2} + V_0 \sin^2(\chi) \right] \phi_{k'}(\chi) &= E_{k'} \phi_{k'}(\chi) \\ \left[-\frac{\partial^2}{\partial \chi^2} + \frac{V_0}{E_r} \sin^2(\chi) \right] \phi_{k'}(\chi) &= \varepsilon_{k'} \phi_{k'}(\chi) \text{ with } \varepsilon_{k'} = \frac{E_{k'}}{E_r} \end{aligned} \tag{106}$$

This differential equation is the *Mathieu equation*:

$$\frac{d^2y}{dx^2} + [A - 2B\cos(2x)]\, y = 0$$
$$\left[-\frac{d^2}{dx^2} - 4B\sin^2 x)\right] y = (A - 2B)y, \tag{107}$$

where we have used $\cos 2\theta = 1 - 2\sin^2\theta$ and multiplied the equation by -1. The parameters of the equation above equal those of Equation (106) when $A = \varepsilon_{k'} - V_0/(2E_r)$ and $B = -V_0/(4E_r)$. A further constraint on the Mathieu equation (107) is that the solutions y must equal the Bloch wavefunctions, which are bound states. It has been shown that this equation can be asymptotically solved for $|B| \gg 1$ (implying that $V_0 \gg 4E_r$) such that the hopping strength equals [5, 23, 24]:

$$J \simeq \frac{4}{\pi} E_r \left(\frac{V_0}{E_r}\right)^{\frac{3}{4}} \exp\left[-2\left(\frac{V_0}{E_r}\right)^{\frac{1}{2}}\right]. \tag{108}$$

4.3 Shaking the lattice

In this section we show how to shake the lattice to generate certain the fluxes computed in Chapter 2. We consider once more the Hamiltonian from the previous chapter that effectively produces a complex hopping coefficient:

$$H(t) = -\sum_{\boldsymbol{x},\ell} J\left(a^\dagger_{\boldsymbol{x}+\boldsymbol{\delta}_\ell} a_{\boldsymbol{x}} + \text{H.c.}\right) + \sum_{\boldsymbol{x}} \left(A_{\boldsymbol{x}} \cos\left(\omega t + \phi_{\boldsymbol{x}}\right) + \Delta_{\boldsymbol{x}}\right) \hat{n}_{\boldsymbol{x}}.$$

By making specific choices for $\phi_{\boldsymbol{x}}$ and $\Delta_{\boldsymbol{x}}$ (plus the introduction of sublattices) we reproduce the Hamiltonians derived in Chapter 2. To illustrate the mechanism we first derive the square lattice with π-flux. After that we continue with $2\pi/3$-flux for the Kagome lattice. With regard to the dice lattice with π-flux, it turns out that constructing a model which uses resonant driving with a site-dependent phase shift is not so straightforward. Due to time constraint we have to omit this result in this thesis.

4.3.1 An example

We start by applying lattice shaking to a simple model: the square lattice with π-flux per unit square plaquette, studied in Section 2.2.1. Recall that we can solve for the energy spectrum of this setup by using two sublattice species. We therefore add an on-site modulation and shift for each sublattice separately:

$$H = (H_A + H_B)\,; \tag{109}$$

$$H_A = -\sum_{\boldsymbol{x}_A} \frac{J}{2}\left(a^\dagger_{\boldsymbol{x}_A} b_{\boldsymbol{x}_A+\boldsymbol{\delta}_1} + a^\dagger_{\boldsymbol{x}_A} a_{\boldsymbol{x}_A+\boldsymbol{\delta}_2} + \text{H.c.}\right) + \sum_{\boldsymbol{x}_A} \left(A\cos(\omega t + \phi_{\boldsymbol{x}_A}) + \Delta_{\boldsymbol{x}_A}\right) \hat{n}_{\boldsymbol{x}_A},$$

$$H_B = -\sum_{\boldsymbol{x}_B} \frac{J}{2}\left(b^\dagger_{\boldsymbol{x}_B} a_{\boldsymbol{x}_B+\boldsymbol{\delta}_1} + b^\dagger_{\boldsymbol{x}_B} b_{\boldsymbol{x}_B+\boldsymbol{\delta}_2} + \text{H.c.}\right) + \sum_{\boldsymbol{x}_B} \left(A\cos(\omega t + \phi_{\boldsymbol{x}_B}) + \Delta_{\boldsymbol{x}_B}\right) \hat{n}_{\boldsymbol{x}_B}. \tag{110}$$

Comparing this expression with the one in Equation (37) we see that we have to choose the shift $\Delta_{\boldsymbol{x}_{A,B}}$ and the phase $\phi_{\boldsymbol{x}_{A,B}}$ such that only the $b^\dagger b$-term obtains a phase factor $e^{i\pi}$. A construction is shown in Figure 39a.
We compute the effective hopping coefficient for this construction using the results from Section ?? for each distinct (positive) hopping direction:

	$\nu_{\boldsymbol{\delta}_\ell}$	$\varphi_{\boldsymbol{\delta}_\ell}$	$\Phi_{\boldsymbol{\delta}_\ell}$	$J_{\text{eff}}\left(\tilde{\mathcal{A}}_{\boldsymbol{\delta}_\ell}\right)/2$
$a^\dagger_{\boldsymbol{x}_A+\boldsymbol{\delta}_2} a_{\boldsymbol{x}_A}$	2	$\pm\frac{\pi}{2}$	0	$J\mathcal{J}_2\left(\frac{A}{\omega}\right)$
$b^\dagger_{\boldsymbol{x}_A+\boldsymbol{\delta}_1} a_{\boldsymbol{x}_A} \Big/ a^\dagger_{\boldsymbol{x}_B+\boldsymbol{\delta}_1} b_{\boldsymbol{x}_B}$	0	$\pm\frac{\pi}{4}$	0	$J\mathcal{J}_0\left(\frac{A}{\sqrt{2}\omega}\right)$
$b^\dagger_{\boldsymbol{x}_B+\boldsymbol{\delta}_2} b_{\boldsymbol{x}_B}$	2	$\pm\frac{\pi}{2}$	$\frac{\pi}{2}$	$J\mathcal{J}_2\left(\frac{A}{\omega}\right)e^{i\pi}$

Recall that $\tilde{\mathcal{A}}_{\boldsymbol{\delta}_\ell} = \frac{A}{\omega}\sin\frac{\varphi_{\boldsymbol{\delta}_\ell}}{2}$ with $\varphi_{\boldsymbol{\delta}_\ell} = (\phi_{\boldsymbol{x}+\boldsymbol{\delta}_\ell} - \phi_{\boldsymbol{x}})/2$, and that the phase factor is defined as $e^{i\nu_{\boldsymbol{\delta}_\ell}\Phi_{\boldsymbol{\delta}_\ell}}$ with $\Phi_{\boldsymbol{\delta}_\ell} = (\phi_{\boldsymbol{x}+\boldsymbol{\delta}_\ell} + \phi_{\boldsymbol{x}})/2$. The Bessel functions $\mathcal{J}_0$ and $\mathcal{J}_2$ are even functions, so that sign of $\tilde{\mathcal{A}}_{\boldsymbol{\delta}_\ell}$ is arbitrary.

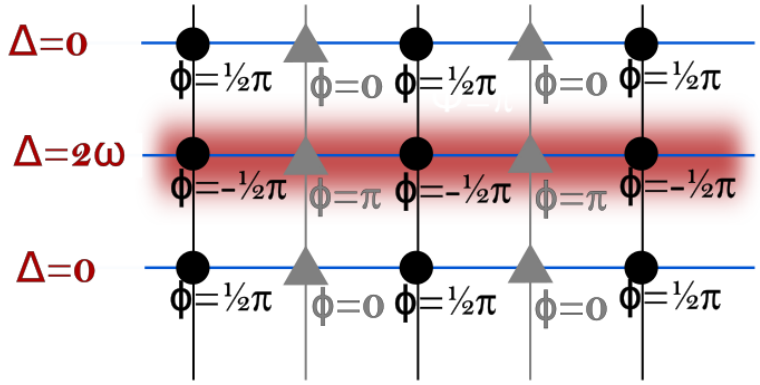

(a) Setup for shaking the square lattice to generate a π-flux, where $\Delta_{\boldsymbol{x}_{A,B}} = 0, 2\omega$ and $\phi_{\boldsymbol{x}_A} = \pm\pi/2$, $\phi_{\boldsymbol{x}_B} = 0, \pi 2$ alternatingly. The black circles indicate sublattice **A** and the grey triangles **B** (see Figure 17).

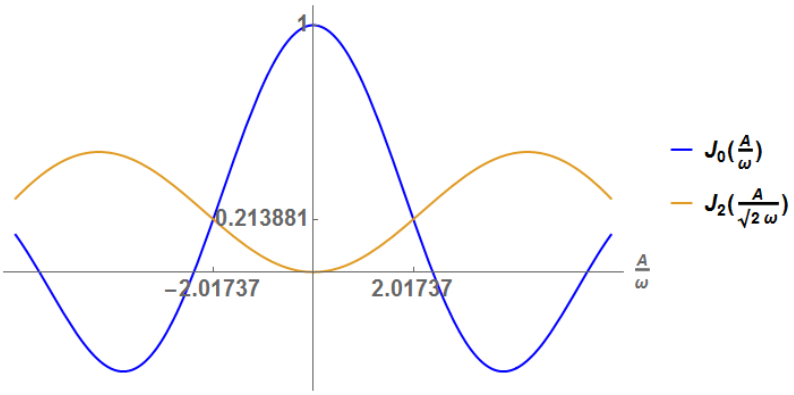

(b) A plot of the values of $\mathcal{J}_0(A/\omega)$ and $\mathcal{J}_2(A/(\sqrt{2}\omega))$ against the parameter A/ω. The values of A/ω for which the two are equal are indicated on the horizontal axis.

Figure 39

Therefore this construction results in a π-phase factor only when particles hop from sublattice **B** to **B**. In Section 2.2.1 we have derived the Bloch Hamiltonian for an equal hopping strength J on all bonds. Here the Bloch Hamiltonian has the same structure, but every matrix element has its own hopping strength:

$$\mathcal{H}_{\boldsymbol{k}} = -J \begin{pmatrix} \mathcal{J}_2\left(\frac{A}{\omega}\right)\cos k_y & \mathcal{J}_0\left(\frac{A}{\sqrt{2}\omega}\right)\cos k_x \\ \mathcal{J}_0\left(\frac{A}{\sqrt{2}\omega}\right)\cos k_x & \mathcal{J}_2\left(\frac{A}{\omega}\right)\cos\left(k_y+\pi\right) \end{pmatrix}. \tag{111}$$

We are interested in the value of A/ω for which $\mathcal{J}_0(A/(\sqrt{2}\omega)) \approx \mathcal{J}_2(A/\omega)$. The two functions are shown in Figure 39b. We see that for $A/\omega \approx \pm 2$ they are approximately equal, and the system will have nearly the same hopping strength between all sites.

4.3.2 The Kagome lattice

We now move to generating flux in the Kagome lattice. First we generate a π-flux per triangular plaquette, which puts the flat band on the bottom of the energy spectrum (but still degenerate). After that we lift the degeneracy by generating a flux of $2\pi/3$.

Flux $\Phi = \pi$ We start by determining the phase shift and tilt needed to reproduce the construction in Section 2.2.4. We introduce the setup shown in Figure 40. Note that to ensure that the bonds between sites are not inhibited due to $\varphi_{\boldsymbol{\delta}_\ell}$ being zero, we put the phases equal to odd multiples of $\pi/4$.

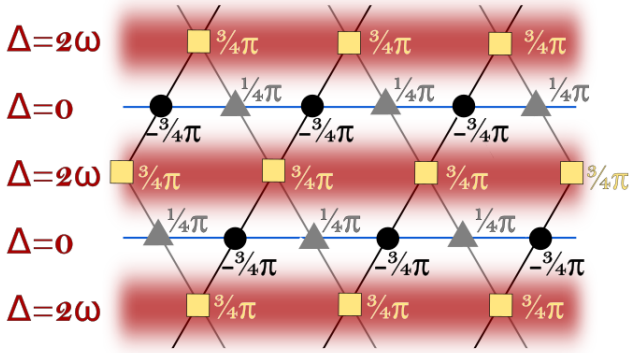

Figure 40: Setup for shaking the Kagome lattice to generate a π-flux per triangular plaquette, where $\Delta_{\boldsymbol{x}_{A,B}} = 0$, $\Delta_{\boldsymbol{x}_C} = 2\omega$ and $\phi_{\boldsymbol{x}_A} = -3\pi/4$, $\phi_{\boldsymbol{x}_B} = 1\pi/4$ and $\phi_{\boldsymbol{x}_C} = 3\pi/4$. The black circles indicate sublattice **A**, the grey triangles **B** and the yellow squares sublattice **C** (see Figure 26a).

Again we recompute the hopping strengh for each distinct hopping direction:

	$\nu_{\boldsymbol{\delta}_\ell}$	$\varphi_{\boldsymbol{\delta}_\ell}$	$\Phi_{\boldsymbol{\delta}_\ell}$	$J_{\text{eff}}\left(\tilde{\mathcal{A}}_{\boldsymbol{\delta}_\ell}\right)/2$
$b^\dagger_{\boldsymbol{x}_A+\boldsymbol{\delta}_1} a_{\boldsymbol{x}_A} \Big/ a^\dagger_{\boldsymbol{x}_B+\boldsymbol{\delta}_1} b_{\boldsymbol{x}_B}$	0	$\pm\frac{\pi}{2}$	$-\frac{\pi}{2}$	$J\mathcal{J}_0\left(\frac{A}{\omega}\right)$
$c^\dagger_{\boldsymbol{x}_A+\boldsymbol{\delta}_2} a_{\boldsymbol{x}_A} \Big/ a^\dagger_{\boldsymbol{x}_C+\boldsymbol{\delta}_2} c_{\boldsymbol{x}_C}$	2	$\pm\frac{3\pi}{4}$	0	$J\mathcal{J}_2\left(\frac{A}{\sqrt{2}\omega}\right)$
$c^\dagger_{\boldsymbol{x}_B+\boldsymbol{\delta}_3} b_{\boldsymbol{x}_B} \Big/ b^\dagger_{\boldsymbol{x}_C+\boldsymbol{\delta}_3} c_{\boldsymbol{x}_C}$	2	$\pm\frac{\pi}{4}$	$\frac{\pi}{2}$	$J\mathcal{J}_2\left(\frac{A}{\sqrt{2}\omega}\right)e^{i\pi}$

Using this the Bloch Hamiltonian becomes:

$$\mathcal{H}_{\boldsymbol{k}} = -J \begin{pmatrix} 0 & \mathcal{J}_0\left(\frac{A}{\omega}\right)\cos \boldsymbol{k}\cdot\boldsymbol{\delta}_1 & \mathcal{J}_2\left(\frac{A}{\sqrt{2}\omega}\right)\cos \boldsymbol{k}\cdot\boldsymbol{\delta}_2 \\ \mathcal{J}_0\left(\frac{A}{\omega}\right)\cos \boldsymbol{k}\cdot\boldsymbol{\delta}_1 & 0 & \mathcal{J}_2\left(\frac{A}{\sqrt{2}\omega}\right)\cos\left(\boldsymbol{k}\cdot\boldsymbol{\delta}_3+\pi\right) \\ \mathcal{J}_2\left(\frac{A}{\sqrt{2}\omega}\right)\cos \boldsymbol{k}\cdot\boldsymbol{\delta}_2 & \mathcal{J}_2\left(\frac{A}{\sqrt{2}\omega}\right)\cos\left(\boldsymbol{k}\cdot\boldsymbol{\delta}_3+\pi\right) & 0 \end{pmatrix}. \tag{112}$$

Once more, for $A/\omega \approx \pm 2$ all the hopping strength will be approximately equal.

Flux $\Phi = \frac{2\pi}{3}$ To obtain the phase factors shown in Figure 27a, we adapt the same tilt as in the previous paragraph. We use odd multiples of $\pi/6$ to prevent inhibition of any of the bonds. A structure corresponding to a $2\pi/3$-flux per triangular plaquette is shown in Figure 41a. One can check that indeed the phases of sites which are at different potential height add up to 0 (2π), $2\pi/3$ or $4\pi/3$.

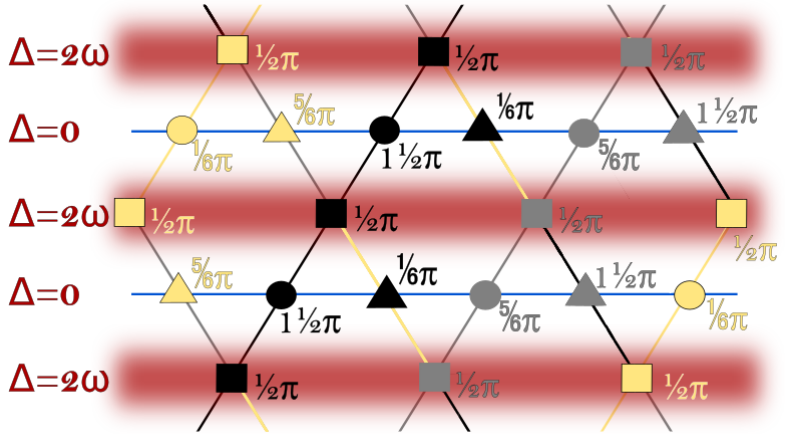

(a) Setup for shaking the Kagome lattice to generate a $2\pi/3$-flux per triangular plaquette, with the tilt and site-dependent phase indicated for each sublattice.

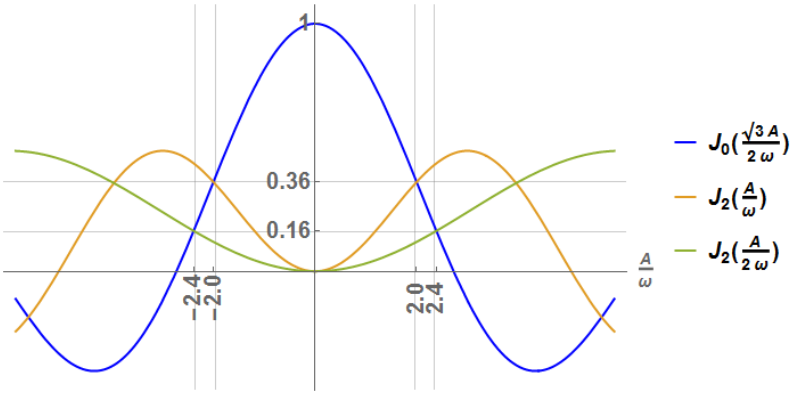

(b) The three Bessel functions which occur in the hopping strength for the setup of (a). One can see that for $A/\omega \sim 2.0 - 2.5$ they are approximately equal.

Figure 41

To see how the hopping strengths are affected, we consider the difference of the on-site phases $\varphi_{\boldsymbol{\delta}_\ell}$. Hopping horizontally (along $\boldsymbol{\delta}_1$) between sites at potential height $\Delta = 0$ results in a hopping strength of $J\mathcal{J}_0(\sqrt{3}A/(2\omega))$. Moving along a diagonal bond ($\boldsymbol{\delta}_{2,3}$) can give a hopping strength of either $J\mathcal{J}_2(A/\omega)$ or $J\mathcal{J}_2(A/(2\omega))$. From the plot of these three functions in Figure 41b we can see that they are never exactly equal. Only for $A/\omega \sim 2.0 - 2.5$ their differences are minimal.

Conclusion & Outlook

Topological insulators that exhibit the Quantum Hall Effect or Fractional Quantum Hall Effect are promising systems for applications in technology. To obtain a better understanding of their properties and how they come about, it pays to examine them in a clean and controllable environment. In this thesis we have proposed a setup that generates flat energy bands using simulation with cold atoms in optical lattices for the Kagome lattice structure.

We have seen that the Kagome lattice has a degenerate energy spectrum where the upper band is flat. By applying a nonuniform magnetic field that corresponds to a $2\pi/3$-flux per triangular plaquette we were able to lift this degeneracy and generate flat bands at the bottom of the energy spectrum, such that they can be used for probing in cold atom systems. Furthermore, we have shown that states in these energy bands indeed possess nontrival topological properties.

By generating an optical potential with the structure of the Kagome lattice, we were able to simulate this system with cold atoms. We created a gauge field - equivalent to a magnetic field - by shaking the lattice, resulting in an on-site periodic modulation. Using the Floquet state formalism we have shown that the effective physics is determined by the time-average of the system. Combining this with resonant driving and a site-dependent phase shift we have constructed a model resulting in the desired energy spectrum. This setup can be used in experiments to probe the flat bands.

Additionally, we have seen that by a slight adjustment of the optical potential, we can obtain the dice structure as well as the Kagome structure in one lattice configuration. Therefore, with this setup one would be able to probe the energy spectra of two different systems within one experimental setup.

We have shown that the dice lattice with π-flux has a completely non-dispersive spectrum with three flat bands. Unfortunately, we were not able to produce the non-dispersive energy spectrum of the dice lattice using the same technique as for the Kagome lattice. There are, however, more complex ways of shaking the lattice that might be more effective (e.g. pulses of linear shaking [25]). For future work this is something worth looking into. Also, for experimental setups that cannot generate a perfect Kagome or dice lattice because the lasers can only be put at right angles, it would be useful to test whether the topological properties are conserved under deformations of the lattice structure.

By implementing interactions, one is immediately in the strong interactions regime. For states in the flat bands, which have no dispersion, interactions will be significant instantly. We thus expect to see e.g. the Fractional Quantum Hall Effect more easily compared to energy bands that are not flat. Using the setup proposed in this thesis, one can generate the flat bands to investigate strongly correlated effects.

References

[1] Tsuneya Ando, Yukio Matsumoto, and Yasutada Uemura. "Theory of Hall effect in a two-dimensional electron system". In: *Journal of the Physical Society of Japan* 39.2 (1975), pp. 279–288.

[2] K v Klitzing, Gerhard Dorda, and Michael Pepper. "New method for high-accuracy determination of the fine-structure constant based on quantized Hall resistance". In: *Physical Review Letters* 45.6 (1980), p. 494.

[3] Horst L Stormer. "Nobel lecture: The fractional quantum Hall effect". In: *Reviews of Modern Physics* 71.4 (1999), p. 875.

[4] Siddharth A Parameswaran, Rahul Roy, and Shivaji L Sondhi. "Fractional quantum Hall physics in topological flat bands". In: *Comptes Rendus Physique* 14.9 (2013), pp. 816–839.

[5] Immanuel Bloch, Jean Dalibard, and Wilhelm Zwerger. "Many-body physics with ultracold gases". In: *Reviews of Modern Physics* 80.3 (2008), p. 885.

[6] Takahiro Fukui, Yasuhiro Hatsugai, and Hiroshi Suzuki. "Chern numbers in discretized brillouin zone: Efficient method of computing (spin) hall conductances". In: *Journal of the Physical Society of Japan* 74.6 (2005), pp. 1674–1677.

[7] Joseph E Avron, Daniel Osadchy, and Ruedi Seiler. "A topological look at the quantum Hall effect". In: *Physics Today* 56.8 (2003), pp. 38–42.

[8] János K Asbóth, László Oroszlány, and András Pályi. "A Short Course on Topological Insulators". In: *arXiv preprint arXiv:1509.02295* (2016).

[9] B Andrei Bernevig and Taylor L Hughes. *Topological insulators and topological superconductors*. Princeton University Press, 2013.

[10] J.F.R. Archilla et al. *Quodons in Mica: Nonlinear Localized Travelling Excitations in Crystals*. Springer Series in Materials Science. Springer International Publishing, 2015. ISBN: 9783319210452. URL: `https://books.google.es/books?id=A9hJCgAAQBAJ`.

[11] Fa Wang and Ying Ran. "Nearly flat band with Chern number C= 2 on the dice lattice". In: *Physical Review B* 84.24 (2011), p. 241103.

[12] Yakir Aharonov and David Bohm. "Significance of electromagnetic potentials in the quantum theory". In: *Physical Review* 115.3 (1959), p. 485.

[13] Richard P Feynman, Robert B Leighton, and Matthew Sands. *The Feynman Lectures on Physics, Desktop Edition Volume I*. Vol. 1. Basic books, 2013.

[14] Julien Vidal, Rémy Mosseri, and Benoit Douçot. "Aharonov-Bohm cages in two-dimensional structures". In: *Physical review letters* 81.26 (1998), p. 5888.

[15] Douglas R Hofstadter. "Energy levels and wave functions of Bloch electrons in rational and irrational magnetic fields". In: *Physical review B* 14.6 (1976), p. 2239.

[16] Egidijus Anisimovas et al. "High-frequency approximation for periodically driven quantum systems from a Floquet-space perspective". In: *New Journal of Physics* 17.9 (2015), p. 093039.

[17] Sergio Blanes et al. "The Magnus expansion and some of its applications". In: *Physics Reports* 470.5 (2009), pp. 151–238.

[18] Mike H Anderson et al. "Observation of Bose-Einstein condensation in a dilute atomic vapor". In: *science* 269.5221 (1995), pp. 198–201.

[19] C Becker et al. "Ultracold quantum gases in triangular optical lattices". In: *New Journal of Physics* 12.6 (2010), p. 065025.

[20] B Damski et al. "Quantum gases in trimerized kagomé lattices". In: *Physical Review A* 72.5 (2005), p. 053612.

[21] AA Burkov and Eugene Demler. "Vortex-peierls states in optical lattices". In: *Physical review letters* 96.18 (2006), p. 180406.

[22] Immanuel Bloch. "Ultracold quantum gases in optical lattices". In: *Nature Physics* 1.1 (2005), pp. 23–30.

[23] Josef Meixner and Friedrich Wilhelm Schäfke. *Mathieusche Funktionen und Sphäroidfunktionen: mit Anwendungen auf physikalische und technische Probleme*. Vol. 71. Springer-Verlag, 2013.

[24] Milton Abramowitz and Irene A Stegun. *Handbook of mathematical functions: with formulas, graphs, and mathematical tables*. Vol. 55. Courier Corporation, 1964.

[25] Julian Struck et al. "Tunable gauge potential for neutral and spinless particles in driven optical lattices". In: *Physical review letters* 108.22 (2012), p. 225304.

[26] Emil J Bergholtz and Zhao Liu. "Topological flat band models and fractional Chern insulators". In: *International Journal of Modern Physics B* 27.24 (2013), p. 1330017.

[27] T Andrijauskas et al. "Three-level Haldane-like model on a dice optical lattice". In: *Physical Review A* 92.3 (2015), p. 033617.

[28] Markus Greiner et al. "Quantum phase transition from a superfluid to a Mott insulator in a gas of ultracold atoms". In: *nature* 415.6867 (2002), pp. 39–44.

[29] Andreas P Schnyder et al. "Classification of topological insulators and superconductors in three spatial dimensions". In: *Physical Review B* 78.19 (2008), p. 195125.

[30] Bo Li et al. "Basic Properties of Periodic Functions." In: *Formalized Mathematics* 17.1-4 (2009), pp. 245–248.

A Symmetries of the Hamiltonian

In this appendix we connect the existence of topological invariants to symmetries in the system. We have mentioned before that a topological invariant is defined globally and is therefore not affected by local deformations. As the topological invariant (Chern number) discussed above can be computed from the energy bands, it is linked to global symmetries of the Hamiltonian that state general properties of the energy spectrum.

A.1 Symmetry classes

We start with a short introduction on what a symmetry encompasses. According to Wigner's theorem, for an eigenstate $|\psi\rangle$ of $\mathcal{H}$ a transformation $S : H \to H$ is a symmetry when the probability $\langle\psi|\psi\rangle$ is conserved. This constrains the operator S to be unitary - $SS^\dagger = \mathbb{1}$ - or anti-unitary: anti-linear $\langle S\psi|S\psi\rangle = \langle\psi|\psi\rangle^*$ and unitary. Note that we can always multiply this unitary operator with a complex phase factor whose modulus equals one.

We consider three symmetries, each explained in more detail in the sections below: time-reversal symmetry, particle-hole symmetry and chiral symmetry.

Time-reversal symmetry (TRS) A system with TRS is symmetric under time reversal $t \to -t$. According to Wigner's theorem we can represent the time reversal operator by an anti-unitary operator $C_{\mathtt{TR}} = U_{\mathtt{TR}}K$, where $U_{\mathtt{TR}}$ is unitary and K denotes complex conjugation. We can deduce the action of the time reversal operator on a TR symmetric Hamiltonian starting from the overlap by appplying it to a test state $H|\psi\rangle$:

$$\begin{aligned} C_{\mathtt{TR}}\Big(H|\psi\rangle\Big) = U_{\mathtt{TR}}H^*|\psi^*\rangle =& U_{\mathtt{TR}}H^*U_{\mathtt{TR}}^\dagger U_{\mathtt{TR}}K|\psi\rangle = U_{\mathtt{TR}}H^*U_{\mathtt{TR}}^\dagger C_{\mathtt{TR}}|\psi\rangle \overset{!}{=} C_{\mathtt{TR}}(H)C_{\mathtt{TR}}|\psi\rangle \\ &\Rightarrow \boxed{C_{\mathtt{TR}}(H) = U_{\mathtt{TR}}H^*U_{\mathtt{TR}}^\dagger} \end{aligned} \tag{113}$$

Note that $H^* = H^{\mathrm{T}}$ because H is Hermitian.

In $\boldsymbol{k}$-space the transformation $t \to -t$ reverses the sign of the momentum $\boldsymbol{k} \to -\boldsymbol{k}$:

$$C_{\mathtt{TR}}(\mathcal{H}_{\boldsymbol{k}}) = \mathcal{H}_{-\boldsymbol{k}} = U_{\mathtt{TR}}\mathcal{H}_{\boldsymbol{k}}^* U_{\mathtt{TR}}^{-1} = C_{\mathtt{TR}}\mathcal{H}_{\boldsymbol{k}}C_{\mathtt{TR}}^{-1}, \tag{114}$$

There is still one degree of freedom for the time-reversal operator, resulting from the fact that $C_{\mathtt{TR}}^2 = \mathbb{1}$. There may be a phase factor in front with absolute value $|\alpha| = 1$. Observe that

$$\begin{aligned} C_{\mathtt{TR}}^2 = U_{\mathtt{TR}}KU_{\mathtt{TR}}K = U_{\mathtt{TR}}U_{\mathtt{TR}}^*K^2 = U_{\mathtt{TR}}U_{\mathtt{TR}}^* &= \alpha\mathbb{1} \\ U_{\mathtt{TR}}\underbrace{U_{\mathtt{TR}}^*U_{\mathtt{TR}}^{\mathrm{T}}}_{=\mathbb{1}} &= \alpha U_{\mathtt{TR}}^{\mathrm{T}} \\ U_{\mathtt{TR}} = \alpha U_{\mathtt{TR}}^{\mathrm{T}} = \alpha(\alpha U_{\mathtt{TR}}^{\mathrm{T}})^{\mathrm{T}} = \alpha^2 U_{\mathtt{TR}} &\Rightarrow \alpha^2 = 1 \\ \alpha = \pm 1 &\Rightarrow U_{\mathtt{TR}} = \pm U_{\mathtt{TR}}^{\mathrm{T}} \end{aligned}$$

The positive sign is for spinless or integer spin systems, also referred to as *TRS (even)*. The negative sign is for half-integer spin systems, referred to as *TRS (odd)* [29].

Particle-hole symmetry (PHS) This symmetry denotes the two different ways one can describe a system: in terms of its particles (occupied sites) or its holes (unoccupied sites). The PHS operator is also anti-unitary, and therefore has the same form as TRS. But the spectrum is inverted as the energy of the unoccupied sites is exactly opposite to that of the occupied sites. The condition for PHS is then

$$C_{\mathtt{PH}}(H) = -H = U_{\mathtt{PH}}H^*U_{\mathtt{PH}}^{-1}. \tag{115}$$

In $\boldsymbol{k}$-space this amounts to

$$C_{\mathtt{PH}}(\mathcal{H}_{\boldsymbol{k}}) = -\mathcal{H}_{-\boldsymbol{k}} = U_{\mathtt{PH}}\mathcal{H}^*_{\boldsymbol{k}}U^{-1}_{\mathtt{PH}} = C_{\mathtt{PH}}\mathcal{H}_{\boldsymbol{k}}C^{-1}_{\mathtt{PH}}. \tag{116}$$

Once again we have an extra degree of freedom in the sign of the transpose of the operator $C_{\mathtt{PH}} = \pm C^{\mathrm{T}}_{\mathtt{PH}}$, now corresponding to the triplet superconducting state for the positive sign and the singlet superconducting state for the negative sign [29].

Chiral symmetry (SLS) A third type of symmetry can be deduced by applying the TRS and PHS operators subsequently:

$$\begin{aligned} P(H) = -H = C_{\mathtt{PH}}(C_{\mathtt{TR}}(H)) = C_{\mathtt{PH}}(UH^*U^{-1}) \\ = U'(UH^*U^{-1})^*U'^{-1} = \underbrace{U'U^*}_{=P} H \underbrace{U^*U'^{-1}}_{=P^{-1}} = PHP^{-1}. \end{aligned} \tag{117}$$

From this we can see that applying the operator twice gives $P^2(H) = P(-H) = H$, and therefore $P^2 = \mathbb{1}$ (for any arbitrary Hamiltonian).
Likewise in $\boldsymbol{k}$-space we get

$$P(\mathcal{H}_{\boldsymbol{k}}) = C_{\mathtt{PH}}(C_{\mathtt{TR}}(\mathcal{H}_{\boldsymbol{k}}) = C_{\mathtt{PH}}(\mathcal{H}_{-\boldsymbol{k}})) = -\mathcal{H}_{\boldsymbol{k}} = P\mathcal{H}_{\boldsymbol{k}}P^{-1}. \tag{118}$$

This defines P as a product of two unitary operators, which sets P to be unitary itself as well:

$$PP^{-1} = U' \underbrace{U^* \, U^{\mathrm{T}}}_{=\mathbb{1}} U'^{-1} = \mathbb{1}. \tag{119}$$

In general, when a system possesses any two of the three symmetries considered above, it will automatically possess the third one as well.

Symmetry classes The presence or absence of each of the three symmetries introduced above in a system determines its topological properties. If the system is topological, its ground states can be partitioned into two topological sectors ($\mathbb{Z}_2$) or into sectors labeled by integers ($\mathbb{Z}$).

		TRS	PHS	SLS	d=1	d=2	d=3
Standard	A (unitary)	0	0	0	-	$\mathbb{Z}$	-
(Wigner-Dyson)	AI (orthogonal)	+1	0	0	-	-	-
	AII (symplectic)	−1	0	0	-	$\mathbb{Z}_2$	$\mathbb{Z}_2$
Chiral	AIII (chiral unitary)	0	0	1	$\mathbb{Z}$	-	$\mathbb{Z}$
(sublattice)	BDI (chiral orthogonal)	+1	+1	1	$\mathbb{Z}$	-	-
	CII (chiral symplectic)	−1	−1	1	$\mathbb{Z}$	-	$\mathbb{Z}_2$
BdG	D	0	+1	0	$\mathbb{Z}_2$	$\mathbb{Z}$	-
	C	0	−1	0	-	$\mathbb{Z}$	-
	DIII	−1	+1	1	$\mathbb{Z}_2$	$\mathbb{Z}_2$	$\mathbb{Z}$
	CI	+1	−1	1	-	-	$\mathbb{Z}$

Figure 42: The symmetry classes of Altland and Zirnbauer (1997) determining the possible topological sectors based on the presence and/or absence of TRS, PHS and SLS, for $d = 1, 2, 3$ spatial dimensions. [29]

A.2 Implications for two-dimensional Hamiltonians

In the next section we derive general conditions for the presence of TRS, PHS and SLS. First we consider some generic properties of the Pauli matrices and two-dimensional Hamiltonians.
For lattice structures with two sublattice species, the Bloch Hamiltonian will be a 2×2-matrix. Therefore one can always rewrite the Hamiltonian in terms of Pauli matrices:

$$\mathcal{H}_{\boldsymbol{k}} = \boldsymbol{v}(\boldsymbol{k}) \cdot \boldsymbol{\sigma}. \tag{120}$$

Here $\boldsymbol{\sigma} = (\sigma_x, \sigma_y, \sigma_z)$ is the vector of Pauli matrices. We can split the vector $\boldsymbol{v}(\boldsymbol{k}) = v(\boldsymbol{k})\hat{\boldsymbol{v}}(\boldsymbol{k})$ into its magnitude and the unit vector $\hat{\boldsymbol{v}}(\boldsymbol{k}) \parallel \boldsymbol{v}(\boldsymbol{k})$ with $|\hat{\boldsymbol{v}}| = 1$.

A.2.1 Pauli matrices

First we compute the eigenvalues and eigenvectors of the Pauli matrices.
Consider σ_z:

$$\sigma_z = \begin{pmatrix} 1 & 0 \\ 0 & -1 \end{pmatrix}. \tag{121}$$

As it is diagonal we see that its eigenvalues are $\lambda_z = \pm 1$. The corresponding eigenstates are $\uparrow = \begin{pmatrix} 1 \\ 0 \end{pmatrix}$ and $\downarrow = \begin{pmatrix} 0 \\ 1 \end{pmatrix}$.
Next we look at σ_x:

$$\sigma_x = \begin{pmatrix} 0 & 1 \\ 1 & 0 \end{pmatrix}. \tag{122}$$

Computing the eigenvalues we again have $\lambda_x = \lambda_z = \pm 1$. The eigenstates are $|+\rangle = \frac{1}{\sqrt{2}} \begin{pmatrix} 1 \\ 1 \end{pmatrix} = \frac{\uparrow + \downarrow}{\sqrt{2}}$ and $|-\rangle = \frac{1}{\sqrt{2}} \begin{pmatrix} 1 \\ -1 \end{pmatrix} = \frac{\uparrow - \downarrow}{\sqrt{2}}$, expressed here in terms of the eigenstates of σ_z.
We diagonalize σ_x into σ_z by transforming it with the unitary matrix composed from its eigenstates: $U_x = \frac{1}{\sqrt{2}} \begin{pmatrix} 1 & 1 \\ -1 & 1 \end{pmatrix}$, giving

$$U_x^\dagger \sigma_x U_x = \sigma_z \tag{123}$$

$$\sigma_x = U_x \sigma_z U_x^\dagger. \tag{124}$$

We can express this unitary matrix as a sum of Pauli matrices and rewrite it as an exponential using Equation (127) derived explicitly below:

$$\begin{aligned} U_x &= \frac{1}{\sqrt{2}} (\mathbb{1} + i\sigma_y) \\ &= \mathbb{1} \cos \frac{\pi}{4} + i\sigma_y \sin \frac{\pi}{4} \\ &= e^{i(\pi/4)\sigma_y} \end{aligned}$$

Finally we consider σ_y:

$$\sigma_y = \begin{pmatrix} 0 & -i \\ i & 0 \end{pmatrix}. \tag{125}$$

Again the eigenvalues are $\lambda_y = \lambda_z = \pm 1$. The eigenstates are $|+i\rangle = \frac{1}{\sqrt{2}} \begin{pmatrix} 1 \\ i \end{pmatrix} = \frac{\uparrow + i\downarrow}{\sqrt{2}}$ and $|-i\rangle = \frac{1}{\sqrt{2}} \begin{pmatrix} 1 \\ -i \end{pmatrix} = \frac{\uparrow - i\downarrow}{\sqrt{2}}$. We find the unitary matrix transforming σ_y into σ_x to be $U_y = \frac{1}{\sqrt{2}} \begin{pmatrix} 1 & 1 \\ i & -i \end{pmatrix}$.

Using the properties of the Pauli matrices that $\sigma_i^2 = \mathbb{1}$ and $\{\sigma_i, \sigma_j\} = 2\delta_{ij}\mathbb{1}$ with $i, j \in \{x, y, z\}$ we see that for $m \in \mathbb{Z}$

$$\begin{aligned}(\hat{\boldsymbol{v}}(\boldsymbol{k}) \cdot \boldsymbol{\sigma})^{2m} &= \big((\hat{\boldsymbol{v}}(\boldsymbol{k}) \cdot \boldsymbol{\sigma})^2\big)^m \\ &= \big((\hat{v}_x(\boldsymbol{k})\sigma_x + \hat{v}_y(\boldsymbol{k})\sigma_y + \hat{v}_z(\boldsymbol{k})\sigma_z)^2\big)^m \\ &= \big((\hat{v}_x^2(\boldsymbol{k}) + \hat{v}_y^2(\boldsymbol{k}) + \hat{v}_z^2(\boldsymbol{k}))\mathbb{1}\big)^m \\ &= \big(|\hat{\boldsymbol{v}}(\boldsymbol{k})|^2\mathbb{1}\big)^m = \mathbb{1}^m = \mathbb{1}. \end{aligned} \tag{126}$$

And therefore $(\hat{\boldsymbol{v}}(\boldsymbol{k}) \cdot \boldsymbol{\sigma})^{2m+1} = \mathbb{1}(\hat{\boldsymbol{v}}(\boldsymbol{k}) \cdot \boldsymbol{\sigma}) = \hat{\boldsymbol{v}}(\boldsymbol{k}) \cdot \boldsymbol{\sigma}$. Note that we can also derive $(\boldsymbol{v}(\boldsymbol{k}) \cdot \boldsymbol{\sigma})^2 = v(\boldsymbol{k})^2(\hat{\boldsymbol{v}}(\boldsymbol{k}) \cdot \boldsymbol{\sigma})^2 = v^2(\boldsymbol{k})\mathbb{1}$. As stated in Equation (134) this is equal to the square of the eigenvalues. This technique can thus be used as a fast way to compute the energy spectrum for a bipartite system.
We use this result in Equation (126) to derive an expression for the exponential of this Hamiltonian:

$$\begin{aligned} e^{iv(\boldsymbol{k})(\hat{\boldsymbol{v}}(\boldsymbol{k}) \cdot \boldsymbol{\sigma})} &= \sum_m \frac{1}{m!} i^m v^m(\boldsymbol{k})(\hat{\boldsymbol{v}}(\boldsymbol{k}) \cdot \boldsymbol{\sigma})^m \\ &= \sum_k \frac{(-1)^m}{(2m)!} v^{2m}(\boldsymbol{k}) \underbrace{(\hat{\boldsymbol{v}}(\boldsymbol{k}) \cdot \boldsymbol{\sigma})^{2m}}_{\mathbb{1}} + i \sum_m \frac{(-1)^m}{(2m+1)!} v^{2m+1}(\boldsymbol{k}) \underbrace{(\hat{\boldsymbol{v}}(\boldsymbol{k}) \cdot \boldsymbol{\sigma})^{2m+1}}_{(\hat{\boldsymbol{v}}(\boldsymbol{k}) \cdot \boldsymbol{\sigma})} \\ &= \mathbb{1} \cos v(\boldsymbol{k}) + i(\hat{\boldsymbol{v}}(\boldsymbol{k}) \cdot \boldsymbol{\sigma}) \sin v(\boldsymbol{k}), \end{aligned} \tag{127}$$

where in the second equality we split the sum into even and odd terms, and used the series expansion for cosine and sine in the third equality.

Finally, consider the product of two Pauli matrices. Using the anticommutation relation and the commutation relation $[\sigma_i, \sigma_j] = 2i\varepsilon_{ij}{}^k\sigma_k$ we rewrite it as

$$\begin{aligned}\sigma_i\sigma_j &= \frac{1}{2}\Big(\{\sigma_i, \sigma_j\} + [\sigma_i, \sigma_j]\Big) \\ &= \delta_{ij}\mathbb{1} + i\varepsilon_{ij}{}^k\sigma_k \end{aligned}$$

For unit vectors $\hat{\boldsymbol{e}}_i$ we see that

$$\begin{aligned}(\hat{\boldsymbol{e}}_i \cdot \boldsymbol{\sigma})(\hat{\boldsymbol{e}}_j \cdot \boldsymbol{\sigma}) &= (\hat{\boldsymbol{e}}_i \cdot \hat{\boldsymbol{e}}_j)\mathbb{1} + i\varepsilon_{ij}{}^k(\hat{\boldsymbol{e}}_k \cdot \boldsymbol{\sigma}) \\ &= (\hat{\boldsymbol{e}}_i \cdot \hat{\boldsymbol{e}}_j)\mathbb{1} + i(\hat{\boldsymbol{e}}_i \times \hat{\boldsymbol{e}}_j) \cdot \boldsymbol{\sigma} \end{aligned}$$

In the last equality we have used that $\varepsilon_{ij}{}^k\hat{\boldsymbol{e}}_k = \varepsilon^{ijk}(\hat{\boldsymbol{e}}_i \times \hat{\boldsymbol{e}}_j)$.
We can generalize this to any two real vectors $\boldsymbol{u}, \boldsymbol{w}$:

$$(\boldsymbol{u} \cdot \boldsymbol{\sigma})(\boldsymbol{w} \cdot \boldsymbol{\sigma}) = \boldsymbol{u} \cdot \boldsymbol{w}\mathbb{1} + i(\boldsymbol{u} \times \boldsymbol{w}) \cdot \boldsymbol{\sigma}. \tag{128}$$

Now we assume that we have a complex vector $\boldsymbol{a} + i\boldsymbol{b}$. The dot product with the vector of Pauli matrices squared is then

$$\begin{aligned}\Big((\boldsymbol{a} + i\boldsymbol{b}) \cdot \boldsymbol{\sigma}\Big)^2 &= \Big(\boldsymbol{a} \cdot \boldsymbol{\sigma} + i\boldsymbol{b} \cdot \boldsymbol{\sigma}\Big)^2 \\ &= (a^2 + b^2 + 2i\boldsymbol{a} \cdot \boldsymbol{b})\mathbb{1} - 2\underbrace{\Big(\boldsymbol{a} \times \boldsymbol{b} + \boldsymbol{b} \times \boldsymbol{a}\Big)}_{=0} \cdot \boldsymbol{\sigma} \\ &= (a^2 + b^2 + 2i\boldsymbol{a} \cdot \boldsymbol{b})\mathbb{1} \end{aligned}$$

The second term in the second equality is zero due to the antisymmetry of the cross product.

A.2.2 Diagonalization of 2×2-Hamiltonians

To diagonalize a Hamiltonian of the form $\mathcal{H}_{\boldsymbol{k}} = \boldsymbol{v}(\boldsymbol{k}) \cdot \boldsymbol{\sigma}$ we look for a transformation

$$U^\dagger(\boldsymbol{v}(\boldsymbol{k}) \cdot \boldsymbol{\sigma})U = v(\boldsymbol{k})\sigma_z. \tag{129}$$

We expect that we can write this transformation as a rotation in spin-space with axes S_x, S_y, S_z (recall that $\boldsymbol{S} = \frac{\boldsymbol{\sigma}}{2}$):

$$U = e^{-i\boldsymbol{w}\cdot\boldsymbol{\sigma}}, \tag{130}$$

where we want to determine the vector $\boldsymbol{w} = \dfrac{\theta}{2}\hat{\boldsymbol{w}}$.

First we show that this transformation indeed corresponds to rotating $\boldsymbol{v}(\boldsymbol{k})$ by an angle θ. For this we use Equation (127) derived above:

$$e^{i\theta/2\hat{\boldsymbol{w}}\cdot\boldsymbol{\sigma}}\Big(\boldsymbol{v}(\boldsymbol{k}) \cdot \boldsymbol{\sigma}\Big)e^{-i\theta/2\hat{\boldsymbol{w}}\cdot\boldsymbol{\sigma}} = \\ \Big(\cos(\theta/2)\mathbb{1} + i\sin(\theta/2)\Big(\hat{\boldsymbol{w}} \cdot \boldsymbol{\sigma}\Big)\Big)\Big(\boldsymbol{v}(\boldsymbol{k}) \cdot \boldsymbol{\sigma}\Big)\Big(\cos(\theta/2)\mathbb{1} - i\sin(\theta/2)\Big(\hat{\boldsymbol{w}} \cdot \boldsymbol{\sigma}\Big)\Big).$$

Using the identity from Equation (128) multiple times, and the facts that
(i) $\boldsymbol{a} \times \boldsymbol{b} = -\boldsymbol{b} \times \boldsymbol{a}$,
(ii) $\boldsymbol{a} \cdot (\boldsymbol{b} \times \boldsymbol{a}) = 0$ and
(iii) Lagrange's formula $\boldsymbol{a} \times (\boldsymbol{b} \times \boldsymbol{c}) = \boldsymbol{b}(\boldsymbol{a} \cdot \boldsymbol{c}) - \boldsymbol{c}(\boldsymbol{a} \cdot \boldsymbol{b})$
we are left with the following terms:

$$\begin{aligned}&\big(\cos^2(\theta/2) - \sin^2(\theta/2)\big)\Big(\boldsymbol{v}(\boldsymbol{k}) \cdot \boldsymbol{\sigma}\Big)\mathbb{1} \\ &\qquad + 2\sin^2(\theta/2)\Big(\hat{\boldsymbol{w}} \cdot \boldsymbol{\sigma}\Big)\Big(\boldsymbol{v}(\boldsymbol{k}) \cdot \hat{\boldsymbol{w}}\Big) + 2\cos(\theta/2)\sin(\theta/2)\Big((\boldsymbol{v}(\boldsymbol{k}) \times \hat{\boldsymbol{w}}) \cdot \boldsymbol{\sigma}\Big) \\ &= \Big[\hat{\boldsymbol{w}}\Big(\boldsymbol{v}(\boldsymbol{k}) \cdot \hat{\boldsymbol{w}}\Big) + \cos\theta\,\Big(\boldsymbol{v} - \hat{\boldsymbol{w}}\Big(\boldsymbol{v}(\boldsymbol{k}) \cdot \hat{\boldsymbol{w}}\Big)\Big) + \sin\theta\Big(\boldsymbol{v}(\boldsymbol{k}) \times \hat{\boldsymbol{w}}\Big)\Big] \cdot \boldsymbol{\sigma} = \mathcal{R}_\theta^{\hat{\boldsymbol{w}}}\big(\boldsymbol{v}(\boldsymbol{k})\big)\boldsymbol{\sigma}.\end{aligned} \tag{131}$$

In the last line we have used the trigonometric identities
(i) $\cos^2(\theta/2) - \sin^2(\theta/2) = \cos\theta$,
(ii) $2\sin^2(\theta/2) = 1 - \cos\theta$ and
(iii) $2\cos(\theta/2)\sin(\theta/2) = \sin\theta$.

Now we take a closer look at the vector $\boldsymbol{w}$. It is characterized by two quantities:

1. The axis of rotation $\hat{\boldsymbol{w}} = C \cdot \big(\hat{\boldsymbol{z}} \times \boldsymbol{v}(\boldsymbol{k})\big) = C \begin{pmatrix} -v_y(\boldsymbol{k}) \\ v_x(\boldsymbol{k}) \\ 0 \end{pmatrix}$. The condition that this vector is normalized results in $C = \dfrac{1}{\sqrt{v_x^2(\boldsymbol{k}) + v_y^2(\boldsymbol{k})}}$. Note that we can rewrite this vector in the more convenient form (using $\boldsymbol{v}(\boldsymbol{k}) = v(\boldsymbol{k})\hat{\boldsymbol{v}}(\boldsymbol{k})$):

$$\hat{\boldsymbol{w}} = \frac{v(\boldsymbol{k})(\hat{\boldsymbol{z}} \times \hat{\boldsymbol{v}}(\boldsymbol{k}))}{\sqrt{v_x^2(\boldsymbol{k}) + v_y^2(\boldsymbol{k})}} = \frac{\hat{\boldsymbol{z}} \times \hat{\boldsymbol{v}}(\boldsymbol{k})}{\sqrt{\dfrac{v_x^2(\boldsymbol{k}) + v_y^2(\boldsymbol{k})}{v^2(\boldsymbol{k})}}} = \frac{\hat{\boldsymbol{z}} \times \hat{\boldsymbol{v}}(\boldsymbol{k})}{\sqrt{1 - \dfrac{v_z^2(\boldsymbol{k})}{v^2(\boldsymbol{k})}}} = \frac{\hat{\boldsymbol{z}} \times \hat{\boldsymbol{v}}(\boldsymbol{k})}{\sqrt{1 - (\hat{\boldsymbol{z}} \cdot \hat{\boldsymbol{v}}(\boldsymbol{k}))^2}}.$$

2. The angle of rotation $\cos\theta = \hat{\boldsymbol{z}} \cdot \hat{\boldsymbol{v}}(\boldsymbol{k})\left(= \dfrac{v_z(\boldsymbol{k})}{v(\boldsymbol{k})}\right)$, such that $\theta = \arccos(\hat{\boldsymbol{z}} \cdot \hat{\boldsymbol{v}}(\boldsymbol{k}))$.

Taking these results and plugging them into Equation (131) shows that

$$\begin{aligned}\mathcal{R}_\theta^{\hat{\boldsymbol{w}}}\big(\boldsymbol{v}(\boldsymbol{k})\big)\boldsymbol{\sigma} &= \left[0 + \big(\hat{\boldsymbol{z}}\cdot\hat{\boldsymbol{v}}(\boldsymbol{k})\big)\boldsymbol{v}(\boldsymbol{k}) + \frac{\sin\left(\arccos(\hat{\boldsymbol{z}}\cdot\hat{\boldsymbol{v}}(\boldsymbol{k}))\right)}{\sqrt{1-(\hat{\boldsymbol{z}}\cdot\hat{\boldsymbol{v}}(\boldsymbol{k}))^2}}\Big(\boldsymbol{v}(\boldsymbol{k})\times\big(\hat{\boldsymbol{z}}\times\hat{\boldsymbol{v}}(\boldsymbol{k})\big)\Big)\right]\cdot\boldsymbol{\sigma} \\ &= \big[\big(\hat{\boldsymbol{z}}\cdot\hat{\boldsymbol{v}}(\boldsymbol{k})\big)\boldsymbol{v}(\boldsymbol{k}) + \big(\boldsymbol{v}(\boldsymbol{k})\cdot\hat{\boldsymbol{v}}(\boldsymbol{k})\big)\hat{\boldsymbol{z}} - \big(\boldsymbol{v}(\boldsymbol{k})\cdot\hat{\boldsymbol{z}}\big)\hat{\boldsymbol{v}}(\boldsymbol{k})\big]\cdot\boldsymbol{\sigma} \\ &= v(\boldsymbol{k})(\hat{\boldsymbol{z}}\cdot\boldsymbol{\sigma}) = v(\boldsymbol{k})\sigma_z. \end{aligned} \tag{132}$$

In the second equality we have used that $\boldsymbol{v}(\boldsymbol{k})\cdot(\hat{\boldsymbol{z}}\times\hat{\boldsymbol{v}}(\boldsymbol{k})) = 0$ and $\sin\left(\arccos(\hat{\boldsymbol{z}}\cdot\boldsymbol{v}(\boldsymbol{k}))\right) = \sqrt{1-(\hat{\boldsymbol{z}}\cdot\hat{\boldsymbol{v}}(\boldsymbol{k}))^2}$.

A.3 Derivation of symmetry constraints

In this section we derive constraints on the Hamiltonian using evolution operator as defined in Section A.2.2,

$$\begin{aligned}\mathcal{H}_{\boldsymbol{k}} &= \boldsymbol{v}(\boldsymbol{k})\cdot\boldsymbol{\sigma} = v_x(\boldsymbol{k})\sigma_x + v_y(\boldsymbol{k})\sigma_y + v_z(\boldsymbol{k})\sigma_z, \\ U &= e^{-i\theta/2\hat{\boldsymbol{w}}\cdot\boldsymbol{\sigma}}.\end{aligned} \tag{133}$$

Because $\mathcal{H}_{\boldsymbol{k}}$ is Hermitian, the components $v_{(x,y,z)}(\boldsymbol{k})$ must be real. It immediately follows that the two energy bands are given by

$$\varepsilon_{\boldsymbol{k}}^{\pm} = \pm\sqrt{v_x^2(\boldsymbol{k}) + v_y^2(\boldsymbol{k}) + v_z^2(\boldsymbol{k})} = \pm v(\boldsymbol{k}). \tag{134}$$

We now demand that transforming the Hamiltonian with the unitary operator U results in the TRS or PHS given by Equation (114) and Equation (116), to see what constraints they give on the general form of the Hamiltonian:

$$\begin{aligned} U^\dagger K\mathcal{H}_{-\boldsymbol{k}}KU &\overset{!}{=} \pm\mathcal{H}_{\boldsymbol{k}} \\ &\Downarrow \\ e^{i\theta/2\hat{\boldsymbol{w}}\cdot\boldsymbol{\sigma}}\Big(\boldsymbol{v}(-\boldsymbol{k})\cdot\boldsymbol{\sigma}^*\Big)e^{-i\theta/2\hat{\boldsymbol{w}}\cdot\boldsymbol{\sigma}} &\overset{!}{=} \pm\boldsymbol{v}(\boldsymbol{k})\cdot\boldsymbol{\sigma}\end{aligned} \tag{135}$$

Here the positive sign denotes TRS and the negative sign PHS. We now focus on the left-hand side of the equation. First we use of the following property of Pauli matrices:

$$-\sigma_y\boldsymbol{\sigma}\sigma_y = \boldsymbol{\sigma}^*. \tag{136}$$

In this section we derive Equation (138) explicitly. Starting from Equation (135) and applying Equation (136) and Equation (126) we arrive at the following expression:

$$\begin{aligned}-\Big(\cos(\theta/2)\mathbb{1} + i\sin(\theta/2)\Big(\hat{\boldsymbol{w}}\cdot\boldsymbol{\sigma}\Big)\Big)\sigma_y\Big(\boldsymbol{v}(-\boldsymbol{k})\cdot\boldsymbol{\sigma}\Big)\sigma_y\Big(\cos(\theta/2)\mathbb{1} \\ - i\sin(\theta/2)\Big(\hat{\boldsymbol{w}}\cdot\boldsymbol{\sigma}\Big)\Big) \overset{!}{=} \pm\boldsymbol{v}(\boldsymbol{k})\cdot\boldsymbol{\sigma}\end{aligned} \tag{137}$$

We solve the left-hand side of this equation term by term:

$$1^{\text{st}}: \qquad -\cos^2(\theta/2)\sigma_y\Big(v_x(-\boldsymbol{k})\sigma_x + v_y(-\boldsymbol{k})\sigma_y + v_z(-\boldsymbol{k})\sigma_z\Big)\sigma_y = -\cos^2(\theta/2)\tilde{\boldsymbol{v}}(-\boldsymbol{k})\cdot\boldsymbol{\sigma}$$

Here we have defined $\tilde{\boldsymbol{v}}(\boldsymbol{k}) = (-v_x(\boldsymbol{k}), v_y(\boldsymbol{k}), -v_z(\boldsymbol{k}))$ which arises from the anticommutation relations of the Pauli matrices. We continue:

$$
\begin{aligned}
2^{\text{nd}}: \qquad & i\cos(\theta/2)\sin(\theta/2)\sigma_y\Big(\boldsymbol{v}(-\boldsymbol{k})\cdot\boldsymbol{\sigma}\Big)\sigma_y\Big(\hat{\boldsymbol{w}}\cdot\boldsymbol{\sigma}\Big) \\
& \qquad = i\cos(\theta/2)\sin(\theta/2)\left[\tilde{\boldsymbol{v}}(-\boldsymbol{k})\cdot\hat{\boldsymbol{w}}\mathbb{1} + i\Big(\tilde{\boldsymbol{v}}(-\boldsymbol{k})\times\hat{\boldsymbol{w}}\Big)\cdot\boldsymbol{\sigma}\right] \\
3^{\text{rd}}: \qquad & -i\cos(\theta/2)\sin(\theta/2)\Big(\hat{\boldsymbol{w}}\cdot\boldsymbol{\sigma}\Big)\sigma_y\Big(\boldsymbol{v}(-\boldsymbol{k})\cdot\boldsymbol{\sigma}\Big)\sigma_y \\
& \qquad = -i\cos(\theta/2)\sin(\theta/2)\left[\hat{\boldsymbol{w}}\cdot\tilde{\boldsymbol{v}}(-\boldsymbol{k})\mathbb{1} + i\underbrace{\Big(\hat{\boldsymbol{w}}\times\tilde{\boldsymbol{v}}(-\boldsymbol{k})\Big)}_{=-\tilde{\boldsymbol{v}}(-\boldsymbol{k})\times\hat{\boldsymbol{w}}}\cdot\boldsymbol{\sigma}\right] \\
4^{\text{th}}: \qquad & -\sin^2(\theta/2)\Big(\hat{\boldsymbol{w}}\cdot\boldsymbol{\sigma}\Big)\sigma_y\Big(\boldsymbol{v}(-\boldsymbol{k})\cdot\boldsymbol{\sigma}\Big)\sigma_y\Big(\hat{\boldsymbol{w}}\cdot\boldsymbol{\sigma}\Big) \\
& \qquad = -\sin^2(\theta/2)\left[2\Big(\tilde{\boldsymbol{v}}(-\boldsymbol{k})\cdot\hat{\boldsymbol{w}}\Big)\hat{\boldsymbol{w}} - \tilde{\boldsymbol{v}}(-\boldsymbol{k})\right]
\end{aligned}
$$

Note that the terms proportional to the identity cancel each other out. Using that
(i) $\cos^2(\theta/2) - \sin^2(\theta/2) = \cos\theta$,
(ii) $2\cos(\theta/2)\sin(\theta/2) = \sin\theta$ and
(iii) $2\sin^2(\theta/2) = 1 - \cos\theta$ adding up the four terms results in

$$
\Big[-\cos\theta\ \tilde{\boldsymbol{v}}(-\boldsymbol{k}) - \sin\theta\Big(\tilde{\boldsymbol{v}}(-\boldsymbol{k})\times\hat{\boldsymbol{w}}\Big) - (1-\cos\theta)\Big(\tilde{\boldsymbol{v}}(-\boldsymbol{k})\cdot\hat{\boldsymbol{w}}\Big)\hat{\boldsymbol{w}}\Big]\cdot\boldsymbol{\sigma} \overset{!}{=} \pm\boldsymbol{v}(\boldsymbol{k})\cdot\boldsymbol{\sigma}. \tag{138}
$$

Because the scalar product is one-to-one the vectors on the left hand side of the dot products must be equal. To look for further properties of this vector, we take its scalar product with $\hat{\boldsymbol{w}}$ (the terms with the cross product automatically become zero):

$$
\begin{gathered}
-\cos\theta\Big(\tilde{\boldsymbol{v}}(-\boldsymbol{k})\cdot\hat{\boldsymbol{w}}\Big) - \sin\theta\cdot 0 - (1-\cos\theta)\Big(\tilde{\boldsymbol{v}}(-\boldsymbol{k})\cdot\hat{\boldsymbol{w}}\Big)\underbrace{|\hat{\boldsymbol{w}}|^2}_{=1} \overset{!}{=} \pm\boldsymbol{v}(\boldsymbol{k})\cdot\hat{\boldsymbol{w}} \\
\Downarrow \\
-\tilde{\boldsymbol{v}}(-\boldsymbol{k})\cdot\hat{\boldsymbol{w}} \overset{!}{=} \pm\boldsymbol{v}(\boldsymbol{k})\cdot\hat{\boldsymbol{w}}
\end{gathered} \tag{139}
$$

This equation puts constraints on the components of $\boldsymbol{v}(\boldsymbol{k})$ for the three symmetries considered here.

Time-Reversal Symmetry In Equation (139) the positive sign indicates TRS. We see that we must have $-\tilde{\boldsymbol{v}}(-\boldsymbol{k}) = \boldsymbol{v}(\boldsymbol{k})$. Componentwise this results in:

$$
\begin{aligned}
v_x(-\boldsymbol{k}) &= v_x(\boldsymbol{k}) \\
-v_y(-\boldsymbol{k}) &= v_y(\boldsymbol{k}) \\
v_z(-\boldsymbol{k}) &= v_z(\boldsymbol{k})
\end{aligned} \tag{140}
$$

Partice-Hole Symmetry For PHS we apply the negative sign in Equation (139). We get the equality $\tilde{\boldsymbol{v}}(-\boldsymbol{k}) = \boldsymbol{v}(\boldsymbol{k})$, resulting in the conditions:

$$
\begin{aligned}
-v_x(-\boldsymbol{k}) &= v_x(\boldsymbol{k}) \\
v_y(-\boldsymbol{k}) &= v_y(\boldsymbol{k}) \\
-v_z(-\boldsymbol{k}) &= v_z(\boldsymbol{k})
\end{aligned} \tag{141}
$$

Chiral symmetry CHS is equivalent to sequentially applying TRS and PHS. Then we must have that $-\tilde{\boldsymbol{v}}(\boldsymbol{k}) = \boldsymbol{v}(\boldsymbol{k})$, giving the conditions:

$$\begin{aligned} v_x(\boldsymbol{k}) &= v_x(\boldsymbol{k}) \\ -v_y(\boldsymbol{k}) &= v_y(\boldsymbol{k}) \Rightarrow v_y(\boldsymbol{k}) = 0 \\ v_z(\boldsymbol{k}) &= v_z(\boldsymbol{k}) \end{aligned} \tag{142}$$

One can observe from the conditions given above that a chiral symmetric Hamiltonian corresponds to a partitioning of topological sectors immediately. Because $\hat{\boldsymbol{n}}(\boldsymbol{k})$ is a unit vector, its values are restricted to points on the two-sphere. Additionally, for CHS its y-component must be zero; thus the vector is confined to a plane and will trace out a circle on the two-sphere. The Hamiltonian cannot be continuously deformed to shrink this circle to a point and change its topological charge. Therefore the winding number is topologically protected and serves as a well-defined characteristic of the system.

In Equation (140), Equation (141) and Equation (142) the constrained component is the one proportional to σ_y. But as the Hamiltonian is invariant under gauge transformations, we can always rotate $\mathcal{H}_{\boldsymbol{k}}$ in three-dimensional $\boldsymbol{\sigma}$-space. The constraints will then have a different form. A case that occurs frequently is a Bloch Hamiltonian of which the diagonal elements are all zero, indicating that $v_z(\boldsymbol{k}) = 0$ for all $\boldsymbol{k}$. By a unitary transformation this is equivalent to the condition in Equation (142) and so these systems have chiral symmetry.

B Kagome lattice with $2\pi/3$-flux

In this appendix we explicitly write down the Hamiltonian for the Kagome lattice with $\Phi = 2\pi/3$ (Section 2.2.4). Then we show how to discretize the Brillouin zone to be able to compute its Chern number numerically.

B.1 Bloch Hamiltonian

Using the three unit vectors for the Kagome lattice,

$$\boldsymbol{\delta}_1 = (1,0), \qquad \boldsymbol{\delta}_2 = \left(\frac{1}{2}, \frac{\sqrt{3}}{2}\right) \quad \text{and} \quad \boldsymbol{\delta}_3 = \left(-\frac{1}{2}, \frac{\sqrt{3}}{2}\right), \tag{143}$$

and Figure 27a we derive the following Bloch Hamiltonian:

$$\mathcal{H}_{\boldsymbol{k}} = -\frac{J}{2}\times$$

$$\begin{pmatrix}
0 & \cos \boldsymbol{k}\cdot\boldsymbol{\delta}_2 & e^{-i\boldsymbol{k}\cdot\boldsymbol{\delta}_1} & 0 & 0 & 0 & 0 & 0 & e^{i\boldsymbol{k}\cdot\boldsymbol{\delta}_1} \\
\cos \boldsymbol{k}\cdot\boldsymbol{\delta}_2 & 0 & e^{i(\boldsymbol{k}\cdot\boldsymbol{\delta}_3+2\pi/3)} & 0 & 0 & 0 & 0 & 0 & e^{-i(\boldsymbol{k}\cdot\boldsymbol{\delta}_3+4\pi/3)} \\
e^{i\boldsymbol{k}\cdot\boldsymbol{\delta}_1} & e^{-i(\boldsymbol{k}\cdot\boldsymbol{\delta}_3+2\pi/3)} & 0 & e^{-i\boldsymbol{k}\cdot\boldsymbol{\delta}_1} & e^{i(\boldsymbol{k}\cdot\boldsymbol{\delta}_3+2\pi/3)} & 0 & 0 & 0 & 0 \\
0 & 0 & e^{i\boldsymbol{k}\cdot\boldsymbol{\delta}_1} & 0 & \cos(\boldsymbol{k}\cdot\boldsymbol{\delta}_2+4\pi/3) & e^{-i\boldsymbol{k}\cdot\boldsymbol{\delta}_1} & 0 & 0 & 0 \\
0 & 0 & e^{-i(\boldsymbol{k}\cdot\boldsymbol{\delta}_3+2\pi/3)} & \cos(\boldsymbol{k}\cdot\boldsymbol{\delta}_2+4\pi/3) & 0 & e^{i\boldsymbol{k}\cdot\boldsymbol{\delta}_3} & 0 & 0 & 0 \\
0 & 0 & 0 & e^{i\boldsymbol{k}\cdot\boldsymbol{\delta}_1} & e^{-i\boldsymbol{k}\cdot\boldsymbol{\delta}_3} & 0 & e^{-i\boldsymbol{k}\cdot\boldsymbol{\delta}_1} & e^{i\boldsymbol{k}\cdot\boldsymbol{\delta}_3} & 0 \\
0 & 0 & 0 & 0 & 0 & e^{i\boldsymbol{k}\cdot\boldsymbol{\delta}_1} & 0 & \cos(\boldsymbol{k}\cdot\boldsymbol{\delta}_2+4\pi/3) & e^{-i\boldsymbol{k}\cdot\boldsymbol{\delta}_1} \\
0 & 0 & 0 & 0 & 0 & e^{-i\boldsymbol{k}\cdot\boldsymbol{\delta}_3} & \cos(\boldsymbol{k}\cdot\boldsymbol{\delta}_2+4\pi/3) & 0 & e^{-i(\boldsymbol{k}\cdot\boldsymbol{\delta}_3+4\pi/3} \\
e^{-i\boldsymbol{k}\cdot\boldsymbol{\delta}_1} & e^{-i(\boldsymbol{k}\cdot\boldsymbol{\delta}_3+4\pi/3)} & 0 & 0 & 0 & 0 & e^{i\boldsymbol{k}\cdot\boldsymbol{\delta}_1} & e^{-i(\boldsymbol{k}\cdot\boldsymbol{\delta}_3+4\pi/3)} & 0
\end{pmatrix} \tag{144}$$

B.2 Chern number

As stated in Section 1.3 the Brillouin zone is a hexagon with a distance of $2\pi/3$ between opposing sides (because the unit cell is tripled in size). A discretization of this BZ is shown in Figure 28. This grid is constructed by discretizing the square $[-\pi/3, \pi/3] \times [-\pi/3, \pi/3]$ in the following way:

$$\begin{aligned}
&\boldsymbol{k}_\alpha = (k_x, k_y) \\
&\quad \Downarrow \\
&k_x = -\frac{\pi}{3} + \frac{\pi}{3\xi} i, && i = 0, \ldots, 2\xi \\
&k_y = -\frac{2}{3\sqrt{3}}\pi + \frac{\pi}{3\xi\sqrt{3}} j, && j = 0, \ldots, 4\xi.
\end{aligned} \tag{145}$$

The edges of the hexagon are now defined by

$$(k_y)^{(1)}_{\pm} = \frac{1}{\sqrt{3}} k_x \pm \frac{2}{3\sqrt{3}}\pi \qquad (k_y)^{(2)}_{\pm} = -\frac{1}{\sqrt{3}} k_x \pm \frac{2}{3\sqrt{3}}\pi \tag{146}$$

$$(k_x)^{(3)}_{\pm} = \pm\frac{\pi}{3}.$$

This construction ensures that we have grid points defined nicely along the edges of the Brillouin zone. Opposite edges are identified with each other without a twist.
When computing the flux of the gauge field through the Brillouin zone, which determines the Chern number, we split the rectangles crossing over the borders $(k_y)^{(1,2)}_{\pm}$ in triangles. We can denote each grid point defined in Equation (145) by its indices (i, j). The point $(1, 1)$ thus corresponds to the grid point in the bottom left corner with coordinates $(k_x, k_y) = (-\pi/3, -2/(3\sqrt{3}))$.

We use this to compute the gauge field in the bulk (including edges $(k_x)^{(3)}_{\pm}$), and separately for the oblique edges $(k_y)^{(1,2)}_{\pm}$:

$$\begin{aligned}
F^{\text{bulk}}_{(i,j)} &: (i,j) \to (i+1,j) \to (i+1,j+1) \to (i,j+1) \to (i,j), \\
F^{1,+}_{(i,j)} &: (i,j) \to (i+1,j) \to (i+1,j+1) \to (i,j), \\
F^{2,+}_{(i,j)} &: (i,j) \to (i+1,j) \to (i,j+1) \to (i,j), \\
F^{1,-}_{(i,j)} &: (i,j) \to (i+1,j+1) \to (i,j+1) \to (i,j), \\
F^{2,-}_{(i,j)} &: (i,j) \to (i+1,j-1) \to (i+1,j) \to (i,j).
\end{aligned} \tag{147}$$

The phase picked up along every step is defined in Equation (19).

C Time-dependent Hamiltonians

C.1 Gauge transformation of the ladder operators

In Section 3.1.1 we show that we can rewrite the time-dependent Hamiltonian by transforming the ladder operators as

$$\begin{aligned} a_{\boldsymbol{x}}^\dagger &\longrightarrow e^{i\theta_{\boldsymbol{x}}(t)\hat{n}_{\boldsymbol{x}}} a_i^\dagger e^{-i\theta_{\boldsymbol{x}}(t)\hat{n}_{\boldsymbol{x}}}, \\ a_{\boldsymbol{x}} &\longrightarrow e^{i\theta_{\boldsymbol{x}}(t)\hat{n}_{\boldsymbol{x}}} a_{\boldsymbol{x}} e^{-i\theta_{\boldsymbol{x}}(t)\hat{n}_{\boldsymbol{x}}}. \end{aligned}$$

To see how this affects the hopping and number operator in the Hamiltonian, we apply the transformed ladder operators on a test Fock state $|n_1, \ldots, n_{\boldsymbol{x}}, \ldots, n_L\rangle$ which we shall denote here as just $|n_{\boldsymbol{x}}\rangle$:

$$\begin{aligned} \tilde{a}_{\boldsymbol{x}}^\dagger |n_{\boldsymbol{x}}\rangle &= e^{i\theta_{\boldsymbol{x}}(t)\hat{n}_{\boldsymbol{x}}} a_{\boldsymbol{x}}^\dagger e^{-i\theta_{\boldsymbol{x}}(t)\hat{n}_{\boldsymbol{x}}} |n_{\boldsymbol{x}}\rangle \\ &= \left(e^{i\theta_{\boldsymbol{x}}(t)\hat{n}_{\boldsymbol{x}}} a_{\boldsymbol{x}}^\dagger |n_{\boldsymbol{x}}\rangle\right) e^{-i\theta_{\boldsymbol{x}}(t) n_{\boldsymbol{x}}} \\ &= \left(e^{i\theta_{\boldsymbol{x}}(t)\hat{n}_{\boldsymbol{x}}} |n_{\boldsymbol{x}}+1\rangle\right) e^{-i\theta_{\boldsymbol{x}}(t) n_{\boldsymbol{x}}} \sqrt{n_{\boldsymbol{x}}+1} \\ &= |n_{\boldsymbol{x}}+1\rangle e^{i\theta_{\boldsymbol{x}}(t)(n_{\boldsymbol{x}}+1)} e^{-i\theta_{\boldsymbol{x}}(t) n_{\boldsymbol{x}}} \sqrt{n_{\boldsymbol{x}}+1} \\ &= e^{i\theta_{\boldsymbol{x}}(t)} \sqrt{n_{\boldsymbol{x}}+1} |n_{\boldsymbol{x}}+1\rangle, \end{aligned}$$

$$\begin{aligned} \tilde{a}_{\boldsymbol{x}} |n_{\boldsymbol{x}}\rangle &= e^{i\theta_{\boldsymbol{x}}(t)\hat{n}_{\boldsymbol{x}}} a_{\boldsymbol{x}} e^{-i\theta_{\boldsymbol{x}}(t)\hat{n}_{\boldsymbol{x}}} |n_{\boldsymbol{x}}\rangle \\ &= \left(e^{i\theta_{\boldsymbol{x}}(t)\hat{n}_{\boldsymbol{x}}} a_{\boldsymbol{x}} |n_{\boldsymbol{x}}\rangle\right) e^{-i\theta_{\boldsymbol{x}}(t) n_{\boldsymbol{x}}} \\ &= \left(e^{i\theta_{\boldsymbol{x}}(t)\hat{n}_{\boldsymbol{x}}} |n_{\boldsymbol{x}}-1\rangle\right) e^{-i\theta_{\boldsymbol{x}}(t) n_{\boldsymbol{x}}} \sqrt{n_{\boldsymbol{x}}} \\ &= |n_{\boldsymbol{x}}-1\rangle e^{i\theta_{\boldsymbol{x}}(t)(n_{\boldsymbol{x}}-1)} e^{-i\theta_{\boldsymbol{x}}(t) n_{\boldsymbol{x}}} \sqrt{n_{\boldsymbol{x}}} \\ &= e^{-i\theta_{\boldsymbol{x}}(t)} \sqrt{n_{\boldsymbol{x}}} |n_{\boldsymbol{x}}-1\rangle. \end{aligned}$$

From this we compute the number operator:

$$\begin{aligned} \hat{\tilde{n}}_{\boldsymbol{x}} |n_{\boldsymbol{x}}\rangle &= \tilde{a}_{\boldsymbol{x}}^\dagger \tilde{a}_{\boldsymbol{x}} |n_{\boldsymbol{x}}\rangle \\ &= \left(e^{-i\theta_{\boldsymbol{x}}(t)} \sqrt{n_{\boldsymbol{x}}}\right) \tilde{a}_{\boldsymbol{x}}^\dagger |n_{\boldsymbol{x}}-1\rangle \\ &= e^{i\theta_{\boldsymbol{x}}(t)} \sqrt{n_{\boldsymbol{x}}}\ e^{-i\theta_{\boldsymbol{x}}(t)} \sqrt{n_{\boldsymbol{x}}} |n_{\boldsymbol{x}}\rangle \\ &= n_{\boldsymbol{x}} |n_{\boldsymbol{x}}\rangle. \end{aligned}$$

We have shown that the number operator $\hat{n}_i$ is invariant under this transformation.
Computing the hopping operator, for which we consider $|\ldots n_{\boldsymbol{x}}, n_{\boldsymbol{x}+\boldsymbol{\delta}_\ell} \ldots\rangle$:

$$\begin{aligned} \tilde{a}_{\boldsymbol{x}+\boldsymbol{\delta}_\ell}^\dagger \tilde{a}_{\boldsymbol{x}} |n_{\boldsymbol{x}}, n_{\boldsymbol{x}+\boldsymbol{\delta}_\ell}\rangle &= \left(e^{-i\theta_{\boldsymbol{x}}(t)} \sqrt{n_{\boldsymbol{x}}}\right) \tilde{a}_{\boldsymbol{x}+\boldsymbol{\delta}_\ell}^\dagger |n_{\boldsymbol{x}}-1, n_{\boldsymbol{x}+\boldsymbol{\delta}_\ell}\rangle \\ &= e^{i\theta_{\boldsymbol{x}+\boldsymbol{\delta}_\ell}(t)} \sqrt{n_{\boldsymbol{x}+\boldsymbol{\delta}_\ell}+1}\ e^{-i\theta_{\boldsymbol{x}}(t)} \sqrt{n_{\boldsymbol{x}}} |n_{\boldsymbol{x}}-1, n_{\boldsymbol{x}+\boldsymbol{\delta}_\ell}+1\rangle \\ &= e^{i\left(\theta_{\boldsymbol{x}+\boldsymbol{\delta}_\ell}(t)-\theta_{\boldsymbol{x}}(t)\right)} \sqrt{n_{\boldsymbol{x}}(n_{\boldsymbol{x}+\boldsymbol{\delta}_\ell}+1)} |n_{\boldsymbol{x}}-1, n_{\boldsymbol{x}+\boldsymbol{\delta}_\ell}+1\rangle. \end{aligned}$$

And therefore the hopping operator transforms as

$$a_{\boldsymbol{x}+\boldsymbol{\delta}_\ell}^\dagger a_{\boldsymbol{x}+\boldsymbol{\delta}_\ell} \longrightarrow \exp\left[i\left(\theta_{\boldsymbol{x}+\boldsymbol{\delta}_\ell}(t) - \theta_{\boldsymbol{x}}(t)\right)\right] a_{\boldsymbol{x}+\boldsymbol{\delta}_\ell}^\dagger a_{\boldsymbol{x}+\boldsymbol{\delta}_\ell}.$$

C.2 Perturbation expansion of H in ω^{-1}

In this appendix we show that the second order term of the high-frequency expansion of H_{eff} equals zero explicitly:

$$H_{\text{eff}}^{(2)} = \frac{i}{T^2} \sum_{\substack{\boldsymbol{x},\ell \\ \boldsymbol{x}',\ell'}} \left[\frac{1}{2} \left(\int_0^T dt_1 \; e^{i\vartheta_{\boldsymbol{\delta}_\ell}(t_1)} \right) \left(\int_0^T dt_1 \; e^{i\vartheta_{\boldsymbol{\delta}'_\ell}(t_1)} \right) \right.$$
$$\left. - \int_0^T dt_1 \left(e^{i\vartheta_{\boldsymbol{\delta}_\ell}(t_1)} \int_0^{t_1} dt_2 \; e^{i\vartheta_{\boldsymbol{\delta}_{\ell'}}(t_2)} \right) \right] \hat{h}_{\boldsymbol{x},\boldsymbol{\delta}_\ell} \hat{h}_{\boldsymbol{x}',\boldsymbol{\delta}_{\ell'}} = 0.$$

To carry out the integration over the exponent of $\vartheta_{\boldsymbol{\delta}_\ell}(t)$ we expand it:

$$\int_0^T dt_1 \; e^{i\vartheta_{\boldsymbol{\delta}_\ell}(t_1)} = \int_0^T dt_1 \left[1 + i\vartheta_{\boldsymbol{\delta}_\ell}(t_1) - \frac{1}{2}\vartheta^2_{\boldsymbol{\delta}_\ell}(t_1) + \mathcal{O}\left(\vartheta^3_{\boldsymbol{\delta}_\ell}\right) \right]$$
$$\simeq T + i\left[\Theta_{\boldsymbol{\delta}_\ell}(T) - \Theta_{\boldsymbol{\delta}_\ell}(0)\right] - \frac{1}{2}\left[\tilde{\Theta}_{\boldsymbol{\delta}_\ell}(T) - \tilde{\Theta}_{\boldsymbol{\delta}_\ell}(0)\right]$$

Here $\partial_t \Theta_{\boldsymbol{\delta}_\ell}(t) = \vartheta_{\boldsymbol{\delta}_\ell}(t)$ and $\partial_t \tilde{\Theta}_{\boldsymbol{\delta}_\ell}(t) = \vartheta^2_{\boldsymbol{\delta}_\ell}(t)$. Note that because $\vartheta_{\boldsymbol{\delta}_\ell}(t)$ is periodic with T, its primitive function $\Theta_{\boldsymbol{\delta}_\ell}(t)$ will be as well. Furthermore, using that [30]

1. T is a period of $\vartheta_{\boldsymbol{\delta}_\ell}(t) \Longrightarrow T$ is a period of $\vartheta^2_{\boldsymbol{\delta}_\ell}(t)$,

we deduce that $\tilde{\Theta}_{\boldsymbol{\delta}_\ell}(t)$ is also periodic with T. Therefore $\Theta_{\boldsymbol{\delta}_| ell l}(t)\big|_0^T = \tilde{\Theta}_{\boldsymbol{\delta}_\ell}(t)\big|_0^T = 0$. The integration of terms of order $\vartheta^3_{\boldsymbol{\delta}_\ell}(t)$ and higher will not contribute using the same reasoning and the fact that

2. T is a period of $\vartheta_{\boldsymbol{\delta}_\ell}(T)$ and of $\vartheta^2_{\boldsymbol{\delta}_\ell}(t) \Longrightarrow T$ is a period of $\vartheta_{\boldsymbol{\delta}_\ell}(t)\vartheta^2_{\boldsymbol{\delta}_\ell}(t) = \vartheta^3_{\boldsymbol{\delta}_\ell}(t)$.

So we have shown that

$$\int_0^T dt_1 \; e^{i\vartheta_{\boldsymbol{\delta}_\ell}(t_1)} = T. \tag{148}$$

Now we focus on the second term in Equation (78) and again expand the exponential keeping everything up to second order:

$$\int_0^T dt_1 \left(e^{i\vartheta_{\boldsymbol{\delta}_\ell}(t_1)} \int_0^{t_1} dt_2 \; e^{i\vartheta_{\boldsymbol{\delta}_{\ell'}}(t_2)} \right)$$
$$= \int_0^T dt_1 \left[\left(1 + i\vartheta_{\boldsymbol{\delta}_\ell}(t_1) - \frac{1}{2}\vartheta^2_{\boldsymbol{\delta}_\ell}(t_1) + \mathcal{O}\left(\vartheta^3_{\boldsymbol{\delta}_\ell}\right) \right) \left(t_1 + i\left[\Theta_{\boldsymbol{\delta}_{\ell'}}(t_1) - \Theta_{\boldsymbol{\delta}_{\ell'}}(0)\right] - \frac{1}{2}\left[\tilde{\Theta}_{\boldsymbol{\delta}_{\ell'}}(t_1) - \tilde{\Theta}_{\boldsymbol{\delta}_{\ell'}}(0)\right] + \dots \right) \right]$$
$$\simeq \int_0^T dt_1 \left(t_1 + i\left[\Theta_{\boldsymbol{\delta}_{\ell'}}(t_1) - \Theta_{\boldsymbol{\delta}_{\ell'}}(0)\right] - \frac{1}{2}\left[\tilde{\Theta}_{\boldsymbol{\delta}_{\ell'}}(t_1) - \tilde{\Theta}_{\boldsymbol{\delta}_{\ell'}}(0)\right] + it_1\vartheta_{\boldsymbol{\delta}_\ell}(t_1) - \vartheta_{\boldsymbol{\delta}_\ell}(t_1)\left[\Theta_{\boldsymbol{\delta}_{\ell'}}(t_1) - \Theta_{\boldsymbol{\delta}_{\ell'}}(0)\right] \right.$$
$$\left. - i\frac{1}{2}\vartheta_{\boldsymbol{\delta}_{\boldsymbol{\ell}}}(t_1)\left[\tilde{\Theta}_{\boldsymbol{\delta}_{\ell'}}(t_1) - \tilde{\Theta}_{\boldsymbol{\delta}_{\ell'}}(0)\right] - \frac{1}{2}t_1\vartheta^2_{\boldsymbol{\delta}_\ell}(t_1) - \frac{i}{2}\vartheta^2_{\boldsymbol{\delta}_\ell}(t_1)\left[\Theta_{\boldsymbol{\delta}_{\ell'}}(t_1) - \Theta_{\boldsymbol{\delta}_{\ell'}}(0)\right] + \frac{1}{4}\vartheta^2_{\boldsymbol{\delta}_\ell}(t_1)\left[\tilde{\Theta}_{\boldsymbol{\delta}_{\ell'}}(t_1) - \tilde{\Theta}_{\boldsymbol{\delta}_{\ell'}}(0)\right] \right).$$

We now solve the integral above term by term.

$$
\begin{aligned}
1^{\text{st}}: \quad & \int_0^T t_1 \, dt_1 = \frac{T^2}{2} \\
2^{\text{nd}}: \quad & \int_0^T i \left[\Theta_{\boldsymbol{\delta}_{\ell'}}(t_1) - \Theta_{\boldsymbol{\delta}_{\ell'}}(0)\right] \, dt_1 = 0 - i\Theta_{\boldsymbol{\delta}_{\ell'}}(0)T \\
3^{\text{rd}}: \quad & \int_0^T \frac{1}{2} - \left[\tilde{\Theta}_{\boldsymbol{\delta}_{\ell'}}(t_1) - \tilde{\Theta}_{\boldsymbol{\delta}_{\ell'}}(0)\right] \, dt_1 = 0 + \frac{1}{2}\tilde{\Theta}_{\boldsymbol{\delta}_{\ell'}}(0)T \\
4^{\text{th}}: \quad & \int_0^T i t_1 \vartheta_{\boldsymbol{\delta}_\ell}(t_1) \, dt_1 \overset{\text{PI}}{=} i \left(t_1 \Theta_{\boldsymbol{\delta}_\ell}(t_1)\Big|_0^T - \underbrace{\int_0^T dt_1 \Theta_{\boldsymbol{\delta}_\ell}(t_1)}_{=0} \right) \\
& \qquad = i\Theta_{\boldsymbol{\delta}_\ell}(T)T \\
5^{\text{th}}: \quad & \int_0^T -\vartheta_{\boldsymbol{\delta}_\ell}(t_1) \left[\Theta_{\boldsymbol{\delta}_{\ell'}}(t_1) - \Theta_{\boldsymbol{\delta}_{\ell'}}(0)\right] \, dt_1 = 0 \text{ (all primitives will be periodic in T)} \\
6^{\text{th}}: \quad & \int_0^T -i\frac{1}{2}\vartheta_{\boldsymbol{\delta}_\ell}(t_1) \left[\tilde{\Theta}_{\boldsymbol{\delta}_{\ell'}}(t_1) - \tilde{\Theta}_{\boldsymbol{\delta}_{\ell'}}(0)\right] dt_1 = 0 \\
7^{\text{th}}: \quad & \int_0^T -\frac{1}{2} t_1 \vartheta^2_{\boldsymbol{\delta}_\ell}(t_1) dt_1 \overset{\text{PI}}{=} -\frac{1}{2} \left(t_1 \tilde{\Theta}_{\boldsymbol{\delta}_\ell}(t_1)\Big|_0^T - \underbrace{\int_0^T dt_1 \tilde{\Theta}_{\boldsymbol{\delta}_\ell}(t_1)}_{=0} \right) \\
& \qquad = -\frac{1}{2}\tilde{\Theta}_{\boldsymbol{\delta}_\ell}(T)T \\
8^{\text{th}}: \quad & \int_0^T -\frac{i}{2}\vartheta^2_{\boldsymbol{\delta}_\ell}(t_1) \left[\Theta_{\boldsymbol{\delta}_{\ell'}}(t_1) - \Theta_{\boldsymbol{\delta}_{e\ell\ell'}}(0)\right] dt_1 = 0 \\
9^{\text{th}}: \quad & \int_0^T \frac{1}{4}\vartheta^2_{\boldsymbol{\delta}_\ell}(t_1) \left[\tilde{\Theta}_{\boldsymbol{\delta}_{\ell'}}(t_1) - \tilde{\Theta}_{\boldsymbol{\delta}_{\ell'}}(0)\right] dt_1 = 0
\end{aligned}
$$

Collecting all terms we see that indeed

$$
H^{(2)}_{\text{eff}} \simeq \frac{i}{T^2} \sum_{\substack{\boldsymbol{x},\ell \\ \boldsymbol{x}',\ell'}} \left[\frac{T^2}{2} - \frac{T^2}{2} - i\left(\Theta_{\boldsymbol{\delta}_\ell}(T) - \Theta_{\boldsymbol{\delta}_\ell}(0)\right)T - \frac{1}{2}\left(\tilde{\Theta}_{\boldsymbol{\delta}_{\ell'}}(T) - \tilde{\Theta}_{\boldsymbol{\delta}_{\ell'}}(0)\right)T \right] \hat{h}_{\boldsymbol{x},\boldsymbol{\delta}_\ell} \hat{h}_{\boldsymbol{x}',\boldsymbol{\delta}_{\ell'}} = 0. \tag{149}
$$